TECHNICAL UNIVERSITY OF LIBEREC
Faculty of Mechatronics, Informatics and Interdisciplinary Studies

Laser-generated synthesis of Pd-Ni nanoalloys usable as catalysts

Master thesis

Study programme: N0719A270001 – Nanotechnology
Study branch: N0719A270001NA – Nanotechnology

Author: **Bc. Ondřej Havelka**
Supervisor: M.Sc. Rafael Omar Torres Mendieta, Ph.D.

Liberec 2021

TECHNICKÁ UNIVERZITA V LIBERCI
**Fakulta mechatroniky, informatiky
a mezioborových studií**

Laserem řízená syntéza nanoslitin paladium-nikl použitelných jako katalyzátory

Diplomová práce

Autor práce:	**Bc. Ondřej Havelka**
Vedoucí práce:	M.Sc. Rafael Omar Torres Mendieta, Ph.D.

Liberec 2021

TECHNICKÁ UNIVERZITA V LIBERCI
Fakulta mechatroniky, informatiky a mezioborových studií

Zadání diplomové práce

Laser-generated synthesis of Pd-Ni nanoalloys usable as catalysts

Jméno a příjmení: **Bc. Ondřej Havelka**
Osobní číslo: M19000143
Studijní program: N0719A270001 Nanotechnologie
Zadávající katedra: Ústav nových technologií a aplikované informatiky
Akademický rok: **2020/2021**

Zásady pro vypracování:

1. The general goal of the thesis is the synthesis of Ni-Pd nanoalloys for its possible exploitation in the catalysis field. The combination of laser ablation in liquids (LAL) and laser photoreduction/oxidation in liquids (LPL) will be employed to reach this aim.
2. Determine the aspects that enable the control over the elemental composition in the nanoalloys. This will be done by testing different laser parameters and the material's precursor concentrations.
3. Analyze different physicochemical properties in the recently created nanoalloys looking for outstanding characteristics derived from the combination of both materials.
4. Finally, the nanoalloys' catalytic behavior will be tested to degrade the organic pollutant 4-nitrophenol (4-NP), which transformation in 4- aminophenol (4-AP) is considered a model reaction for evaluating the catalytic activity of the newly developed catalyst. After evaluating the nanoalloys' catalytic capacities in the model reaction, we will test their utility in the fabrication of one of the most promising catalysts towards the reduction of organic pollutants; graphene oxide-based composites decorated with nanoparticles.

Rozsah grafických prací: dle potřeby dokumentace
Rozsah pracovní zprávy: 40 – 50 stran
Forma zpracování práce: tištěná/elektronická
Jazyk práce: Angličtina

Seznam odborné literatury:

[1] FERRANDO, Riccardo; JELLINEK, Julius; JOHNSTON, Roy L. Nanoalloys: from theory to applications of alloy clusters and nanoparticles. *Chemical reviews*, 2008, 108.3: 845-910.

[2] AGUILERA-GRANJA, F., et al. Structural and magnetic properties of X 12 Y (X, Y= Fe, Co, Ni, Ru, Rh, Pd, and Pt) nanoalloys. *The Journal of Chemical Physics*, 2010, 132.18: 184507.

[3] GAWANDE, Manoj B.; FORNASIERO, Paolo; ZBOR̆IL, Radek. Carbon-Based Single-Atom Catalysts for Advanced Applications. *ACS Catalysis*, 2020, 10.3: 2231-2259.

[4] GUISBIERS, G., et al. Size and shape effects on the phase diagrams of nickel-based bimetallic nanoalloys. *The Journal of Physical Chemistry C*, 2017, 121.12: 6930-6939.

[5] ABDELSAYED, Victor, et al. Laser synthesis of bimetallic nanoalloys in the vapor and liquid phases and the magnetic properties of PdM and PtM nanoparticles (M= Fe, Co and Ni). *Faraday Discussions*, 2008, 138: 163-180.

[6] ZHANG, Dongshi; GÖKCE, Bilal; BARCIKOWSKI, Stephan. Laser synthesis and processing of colloids: fundamentals and applications. *Chemical reviews*, 2017, 117.5: 3990-4103.

[7] SAKAMOTO, Masanori; FUJISTUKA, Mamoru; MAJIMA, Tetsuro. Light as a construction tool of metal nanoparticles: Synthesis and mechanism. *Journal of Photochemistry and Photobiology C: Photochemistry Reviews*, 2009, 10.1: 33-56.

[8] MATSUMOTO, Ayumu, et al. Transfer of the species dissolved in a liquid into laser ablation plasma: an approach using emission spectroscopy. *The Journal of Physical Chemistry C*, 2015, 119.47: 26506-26511.

[9] TORRES-MENDIETA, Rafael, et al. Laser-assisted synthesis of Fe-Cu oxide nanocrystals. *Applied Surface Science*, 2019, 469: 1007-1015.

[10] SARAEVA, Irina Nikolaevna, et al. Laser synthesis of colloidal Si@ Au and Si@ Ag nanoparticles in water via plasma-assisted reduction. *Journal of Photochemistry and Photobiology A: Chemistry*, 2018, 360: 125-131.

[11] REVATHY, T. A., et al. Highly active graphene-supported palladium-nickel alloy nanoparticles for catalytic reduction of 4-nitrophenol. *Applied Surface Science*, 2018, 449: 764-771.

[12] GAO, Xiang, et al. Facile synthesis of PdNiP/Reduced graphene oxide nanocomposites for catalytic reduction of 4-nitrophenol. *Materials Chemistry and Physics*, 2019, 222: 391-397.

[13] LEPPERT, Linn; KEMPE, Rhett; KÜMMEL, Stephan. Hydrogen binding energies and electronic structure of Ni–Pd particles: a clue to their special catalytic properties. *Physical Chemistry Chemical Physics*, 2015, 17.39: 26140-26148.

Vedoucí práce:	Dr. Rafael Torres
	Ústav nových technologií a aplikované informatiky

Datum zadání práce:	19. října 2020
Předpokládaný termín odevzdání:	17. května 2021

L.S.

prof. Ing. Zdeněk Plíva, Ph.D. Ing. Josef Novák, Ph.D.
děkan vedoucí ústavu

V Liberci dne 19. října 2020

Declaration

I hereby certify that I have been informed that Act 121/2000, the Copyright Act of the Czech Republic, namely Section 60, Schoolwork, applies to my bachelor thesis in full scope. I acknowledge that the Technical University of Liberec (TUL) does not infringe my copyrights by using my bachelor thesis for TUL's internal purposes.

I am aware of my obligation to inform TUL on having used or licensed to use my bachelor thesis in which event TUL may require compensation of costs incurred in creating the work at up to their actual amount.

I have written my bachelor thesis myself using literature listed therein and consulting it with my supervisor and my tutor.

I hereby also declare that the hard copy of my bachelor thesis is identical with its electronic form as saved at the IS STAG portal.

Date:

Signature:

Abstract

The central theme of the thesis is the eco-friendly laser-assisted synthesis of Pd-NiO$_z$ nanoparticles (NPs) decorating partly reduced graphene oxide (prGO) support for their use as catalysts. The NPs obtained in a colloidal form were produced from a low energy plasma reaction and consist of 30-40 nm size NiO$_z$ NPs surrounded by 7 nm Pd NPs. The chemical nature of these NPs mixture was controlled by the amount of Pd salt included in the laser-mediated synthesis process. Such control resulted in the design of nanomaterials combining high magnetic responsiveness and robust catalytic behavior. As experimentally identified through the model reduction of 4-NP, one of the worst world pollutants, the increasing amount of Pd leads to increased catalytic performance. At the same time, the turnover frequency for the highest Pd concentration overcomes 3181 h^{-1}, which is competitive with the highest values of Pd NPs/support catalysts found in the literature. In addition, the sample composed of 8.35 wt% Pd and 91.65 wt% Ni exhibits an excellent decoration of prGO, which can bring many benefits for future applications in the catalysis field due to the expected catalytic enhancement prompted by the synergies between the nanoalloy and prGO. Overall, the current thesis represents a step forward in the fine control over the nanomaterials physicochemical features, which ultimately has a beneficial impact on a technological field as critical as catalysis.

Keywords: reactive laser ablation, control of chemical composition, palladium nanoparticle, nickel nanoparticle, metal-support interaction, nanocatalyst, graphene-based nanosupport

Graphical abstract

Pd-NiO$_z$ /graphene-based nanocatalyst
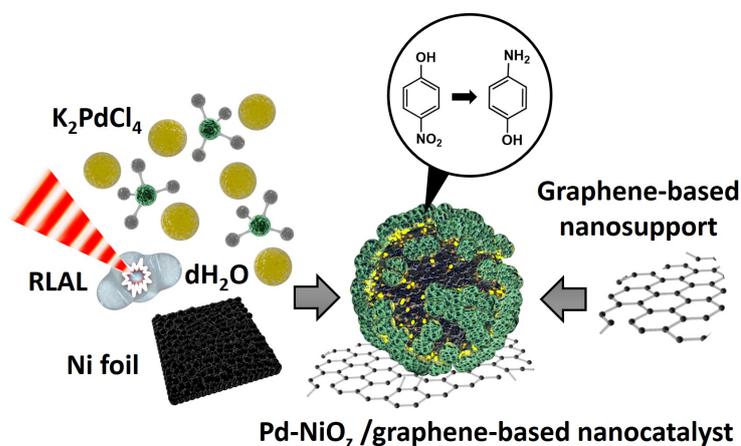
Abstrakt

Hlavním tématem práce je udržitelná laserem asistovaná syntéza Pd-NiO$_z$ nanočástic, které jsou použity k modifikaci částečně redukovaného grafen oxidu, přičemž částice i dekorované nanostruktury představují potenciální katalyzátory. Generované palladium-niklové koloidy byly vyrobeny reakcí v plazmatu s nízkou energií a skládají se z nanočástic NiO$_z$ o velikosti 30-40 nm obklopených 7 nm Pd nanočásticemi. Chemická povaha směsi těchto nanočástic byla řízena množstvím Pd soli obsažené v procesu laserové syntézy. Toto řízení vedlo k tvorbě nanomateriálů kombinujících vysokou magnetickou citlivost a silné katalytické účinky. Na základě modelové redukce 4-NP, jednoho z nejhorších světových polutantů, bylo možné zjistit, že zvyšující se množství Pd vede ke zvýšení katalytického účinku, přičemž frekvence reakčního obratu pro nejvyšší koncentraci Pd překračuje 3181 h^{-1}, což dle literatury konkuruje nejúčinnějším katalyzátorům na bázi paladia a nosiče. Kromě toho vzorek složený z 8,35 % Pd a 91,65 % Ni vykazuje vynikající úroveň nanesených nanočástic na grafenový materiál, což může přinést mnoho výhod v možných aplikacích v katalýze díky očekávanému navýšení katalytického účinku vyvolaného synergií mezi nanoslitinou a částečně redukovaným grafenem oxidu. Celkově tato práce představuje krok vpřed v jemné kontrole fyzikálně-chemických vlastností nanomateriálů, což má v konečném důsledku příznivý dopad na tak zásadní technologickou oblast, jakou je katalýza.

Klíčová slova: reaktivní laserová ablace, řízení chemického složení, nanočástice paladia, nanočástice niklu, interakce kov-nosič, nanokatalyzátor, grafenový nosič

Grafický abstrakt

Acknowledgements

Citation

HAVELKA, Ondřej. Laser-generated synthesis of Pd-Ni nanoalloys usable as catalysts. Liberec: Technical University of Liberec, The Institute for Nanomaterials, Advanced Technologies and Innovation, 2021. Supervisor: Rafael Omar Torres-Mendieta

Contents

List of abbreviations

ANGEL	**A**dvanced **N**anoparticles **G**eneration and **E**xcitation in **L**iquids
AP	**A**minophenol
CCD	**C**harge-**C**oupled **D**evice
CW laser	**C**ontinuum **W**ave laser
demiH$_2$O	**demi**neralized water
DLS	**D**ynamic **L**ight **S**cattering
EDX	**E**nergy-**D**ispersive **X**-ray spectroscopy
FET	**F**ield **E**ffect **T**ransistor
FTIR	**F**ourier-**T**ransform **I**nfrared spectroscopy
FWHM	**F**ull **W**idth at **H**alf **M**aximum
GO	**G**raphene **O**xide
HAADF	**H**igh-**A**ngle **A**nnular **D**ark-**F**ield
HPLC	**H**igh **P**erformance **L**iquid **C**hromatography
HR-TEM	**H**igh-**R**esolution **T**ransmission **E**lectron **M**icroscope
ICDD	**I**nternational **C**entre for **D**iffraction **D**ata
LAL	**L**aser **A**blation in **L**iquids
LASER	**L**ight **A**mplification by **S**timulated **E**mission of **R**adiation
LDE	**L**aser **D**oppler **E**lectrophoresis
LDL	**L**aser **D**efect engineering in **L**iquids
LFL	**L**aser **F**ragmentation in **L**iquids
LIPSS	**L**aser-**I**nduced **P**eriodic **S**urface **S**tructures
LML	**L**aser **M**elting in **L**iquids
LOM	**L**ight **O**ptical **M**icroscopy
LPL	**L**aser **P**hoto-reaction in **L**iquids
LSPC	**L**aser **S**ynthesis and **P**rocessing of **C**olloids
MeCN	**A**cetonitrile
MSI	**M**etal **S**upport **I**nteraction
NP	**N**itrophenol
NPs	**N**anoparticles
rGO	**r**educed **G**raphene **O**xide
RLAL	**R**eactive **L**aser **A**blation in **L**iquids
SA:V	**S**urface-to-**V**olume ratio
SADP	**S**elected **A**rea **D**iffraction **P**attern
SAED	**S**elected **A**rea **E**lectron **D**iffraction
SDD	**S**ilicon **D**rift **D**etector
SEM	**S**canning **E**lectron **M**icroscope
spICP-MS	**s**ingle **p**article **I**nductively **C**oupled **P**lasma **M**ass **S**pectroscopy
PLAL	**P**ulsed **L**aser **A**blation in **L**iquids
prGO	**p**artly-**r**educed **G**raphene **O**xide
PTFE	**P**olytetrafluorethylen
TEM	**T**ransmission **E**lectron **M**icroscope
TOF	**T**urn**o**ver **F**requency
UV-Vis	**U**ltraviolet-**V**isible
VSM	**V**ibrating-**S**ample **M**agnetometry
WDX	**W**avelength-**D**ispersive **X**-ray spectroscopy
XRD	**X** - **R**ay **D**iffraction

List of Figures

List of Tables

1 Introduction

As a 21st-century rising representative of worldwide innovation and development, nanotechnology brings answers to the current and future human society issues [1, 2]. Currently, there is a significant increase in the importance of nanomaterials, which are extremely useful products of the nanotechnology industry. Various nanomaterials have been developed over the last few decades for the benefit of humankind [3]; nevertheless, many toxic and hazardous stabilization agents and precursors have been used during their fabrication [4]. For this reason, the find of green alternatives for the preparation of nanomaterials has attracted enormous attention [5, 6].

The nanoparticles (NPs) that are conceived as nanomaterials with all dimensions in a nanometer-level exhibit unique and interesting features compared to the bulk material. Although, the chemical composition of bulk and nano-sized material does not have to be different. The uniqueness directly comes from their nano-dimensions, i.e., size, shape, and enormous surface to volume ratio [7, 8, 9]. As the best benefit coming from it, the NPs have been already tested for many possible applications, e.g. sensing [10, 11, 12], magnetorheology [13, 14, 15], biomedicine [16, 17, 18], targeted drug delivery [19, 20, 21], and catalysis [22, 23, 24].

In particular, the catalysis field highly profits from the large surface of NPs. In general, there are a lot of metallic NPs known for their excellent catalytic behavior. One of the best materials is palladium (Pd), which has been used many times for different catalytic reactions [25, 26, 27]. Nevertheless, as it happens for other metallic NPs, the Pd catalysts face issues with the aggregation of NPs and their loosing during the recycling of catalytic material, among others. Both problems can be solved by using a nanosupport, which serves as a prevention for both thanks to its bonding with individual particles [28]. Moreover, the nanosupport can increase the catalytic activity itself thanks to the higher free-surface of non-agglomerated particles.

The employment of the nanosupport is not the only way to improve the metallic catalyst performance. Interestingly, the great features of monometallic NPs, as palladium ones, can be modified by incorporating another metal element in the nanoparticle's lattice. The interaction between two different metals leads to the gain of the properties, whose combination is highly attractive for science. Moreover, the bimetallic NPs can play a crucial role in the most spread catalytic field - heterogeneous catalysis [29]. Especially, Pd-based NPs find a niche of application in the reduction and hydrogenation reaction [30, 31, 32, 33]. The chemical industry know hydrogenation processes as the most significant transformation reaction. The specific applications include the synthesis of active materials for pharmacy, the

preparation of biologically active moieties and dyes, or rubber chemistry. Besides, one of the most interesting reductive reactions needing a catalyst is the reduction of CO_2 to chemicals or fuels [34]. The product of this reaction could be a fuel for the future conquest of the planet Mars [35].

The current scientific progress in heterogeneous catalysis includes the synthesis of bimetallic and multimetallic alloyed NPs. Such an ambition can be really demanding for many synthesis perspectives but can be done in a relatively easy way in the field of laser-mediated synthesis. This procedure of NPs synthesis became a part of the modern industry at the end of 2020 [36]. Moreover, as discussed by the scientific community, the pulsed laser-assisted synthesis of nanoalloys with a specific composition represents the next most significant challenge of the field [37, 38]. The idea was presented at the last scientific field conference - Advanced Nanoparticles Generation and Excitation in Liquids (ANGEL) [37]:

"An important challenge for ANGEL could be the synthesis of nanoalloys with a specific composition. The generation of bimetallic nanoparticles (NPs) by laser ablation in liquid (LAL) is well established and is an important strength of LAL. Despite this, to date is impossible to control or drive the synthesis toward a specific NPs composition. This would make the technique even more promising and interesting."

The most common option for getting bimetallic NPs is based on employing bimetallic foils, which are ablated by pulsed lasers [39, 40, 41]. Aside from that, the reactive laser ablation in liquids (RLAL) representing the combination of laser ablation and laser photo-reaction methodologies brings the field a new option to manage the nanoalloys composition for fabricating the nanocatalysts. Compared with the traditional laser ablation, the RLAL mechanism includes reactive reactions between species from the laser ablation of a monometallic foil and the dissociation of metal salt species immersed in a solvent.

This nanoparticle-producing technique that agrees with the twelve principles of green chemistry [42] brings an ideal way for fabricating highly active bimetallic catalysts. The most powerful technique's advantages are the preparation of ligand-free NPs and their sustainability. For this reason, the fundamental goal of the this thesis is to synthesize palladium-nickel nanoalloys, a material well-known for palladium-mediated catalytic and nickel-mediated magnetic properties, by a laser-promoted plasma reaction. The added function of magnetism response induced by the nickel enables the easy manipulation of nanocatalyst [43, 44]. Besides, the anchoring of nanoalloys over the two-dimensional material as graphene, one of the most used nanosupports, opens a promising way to increase the excellent catalytic activity coming from the free surface of particles and graphene's conductivity. In addition, the thesis methodology represents a test of *ad hoc* design for the nanoalloys preparation by RLAL, where the precise control of nanoalloys composition that RLAL permits is expected to bring a scientific breakthrough-representing in this way, a perfect challenge to face in the thesis.

2 Catalysts

Catalytic field as a significant part of science includes many possible application areas, e.g., human health care, environment treatment, pharmacy, material science, chemical industry, nutrition, and energy conversion [45, 46, 47, 48, 49]. Briefly, catalysis represents fast, high-yielding conversions of precursors into the required products of chemical reactions without undesired side-products ideally [50]. The significance of catalysis can be proved by the fact that beyond 85% of all chemical productions of the modern industry comes from catalyzed reactions. Thus, the progress in catalysis has a crucial role in contemporary society's life [51, 52].

The entities responsible for catalysis are known as catalysts, which can be divided into homogeneous and heterogeneous ones [53]. The homogeneous catalysts consist of materials with a phase that differs from that of the reactants or products, which leads to their difficult separation from the reaction and the impossibility to re-use it. Nevertheless, the reaction between the catalyst and reactants is better thanks to their easy solubility and extreme selectivity [51, 54]. The opposite situations occur in the heterogeneous catalysts, which are made of a solid material (especially metals) [51]. Like other types of catalysts, the heterogeneous catalysts are not consumed, and thus their amount during the reaction does not change. The catalysts serve to decrease the required energy needed to achieve the transition state of the corresponding chemical reaction, while the reactants more probably reach their energy barrier and get converted into the desired product of the chemical reaction. Nevertheless, the active sites of catalysts that are responsible for changing the kinetics of the reaction can be deactivated by reactants, and consequently, the cleaning of the catalysts is necessary before their reuse [55].

The modern heterogeneous catalysts can be composed of many constituents [56, 57]. One of them is represented by an active catalytic component responsible for lowering the transition energy in a chemical reaction and is usually considered a catalyst when standing alone. Its surface area, morphology, chemical, electrical properties, preparation method, and many other parameters influence the catalyst's activity, selectivity of the reaction, stability, and final applicability [58, 59, 60, 61]. These parameters can be affected by other components - promoters and supports.

The promoters are not responsible for the catalytic activity in the reaction themselves, but they can purposefully improve the catalyst activity and consequently also the final application [62, 63]. Since there are many features that promoters can ameliorate, they are divided into structural, electronic, and textural ones, etc. The structural promoters enable the modification of the surface properties of a catalyst and increase its number of active sites [64]. Besides, the electronic promoters change the

electronic catalyst features. The connection between the catalysts' active part with the electronic promoter leads to different strengths of catalyst-reactant bonds [65]. Finally, the textural promoter protects the catalyst from sintering, which mainly occurs at high temperatures [66].

As well as promoters, the supporters have no point of interest in doing the catalytic activity themselves. However, the supporters decorated by active components make the catalyst more accessible to the reactants, and thus the catalysts could be more efficient [67]. This is done by a good dispersion of active components throughout the support's surface, enabling to decrease the amount of material employed [68]. Besides, the supports may influence the properties of the active components as the promoters do and even can act as the promoters. Moreover, the supporting of the catalyst leads to its stabilization, which is highly desired [69].

The applications of catalysts are vast, as was summarized. In our study, the created catalysts are examined on the efficiency to transform 4-nitrophenol (4-NP) to 4-aminophenol (4-AP), which represents a model testing reaction for new catalysts [70].

2.1   Nitrophenol

The nitrophenols constitute some of the most common pollutants coming from various industry fields, e.g., pharmacy or pesticides, herbicides, plasticides, and explosives production [71, 72]. These pollutants are nitroaromatic compounds known for their high toxicity to animals, plants, and the environment. However, they can be degraded in the environment by usual biological processes [72].

The health danger coming from the pollutant is exceptionally high. The undesirable impact of nitrophenols was noticed on the skin, eyes, kidneys, liver, muscles, nervous, or blood system. Besides, exposure to nitrophenol leads to the creation of carcinoma [73, 74]. Moreover, the negative influence of pollutants can lead to death. This is largely exemplified in the case of rats, where deadly dose for a large population of adult rats can be only 1 g/kg [75].

Since nitrophenols and especially 4-NP represent a serious danger to the environment, it is necessary to use technological advances for its degradation or removal. The methodologies, which have been already used, include adsorption, electrochemical treatment, and microbial degradation, but all of them have limitations [73]. These limitations like low efficiency, slow degradation rate, and no cost-effectiveness, among others, disable their use for large-scale applications [76].

Contrary to these methodologies, the catalytic hydrogenation reaction successfully faces these issues and enables the transformation of 4-NP into the 4-AP, which is a precursor for antipyretic and analgesic drugs [77]. The change of this pollutant into a useful product makes this methodology a good way for degrading 4-NP. Therefore, since the catalytic hydrogenation of 4-NP to 4-AP is highly desired, the demand to use catalysts in this reaction is natural. Some of the most common catalysts for this purpose are the metal-based NPs [74, 78], which are also used in this study.

3   Nanoalloys

The NPs represent a material entity including several or even millions of merged atoms. Such an entity can be composed of a single type of atom, molecule, or different elements, which create a crystal or an amorphous particle. When the NPs include at least two different metal atoms, they are known as nanoalloys. Bimetallic and even trimetallic nanoalloys have already been subjected to the research [79]. Nevertheless, four and more different types of atoms represent a troublesome challenge, which is not on the top of modern science society goals. In the following text, bimetallic nanoalloys will be discussed unless otherwise stated.

The change of nanoalloy's size, morphology, and mainly elemental composition enables the control of their optical, catalytic, or electronic properties [80, 81, 82]. Moreover, adding a different element in original NPs or changing their size brings many new nanoalloys variants and their characteristics. Therefore, a lot of experimental and theoretical research work is necessary and crucial. In any case, the performances of single element NPs can be very easily boosted, which represents one of the main nanoalloys' benefits for applications. In particular, the synergistic effect of properties belonging to separate single elemental NPs can occur [79]. The combination of different characteristics, such as catalytic activity and magnetic behavior together [83], or the overlapping of their different characteristics, as in the case of Surface Plasmon Resonance [84], opens new opportunities for nanotechnology and nanoscience. Besides, new features appear in comparison with a bulk alloyed material, e.g., full miscibility [85, 86].

Another opportunity for nanoalloys conversion is hidden in the manipulation of the atoms' positions in the structure (Fig. 3.1). One of the most common architectures of alloyed NPs is core-shell, where one element is isolated on the outer part of the structure, and the other one is in the center of the nanoalloy [79]. The inner part and outer part of NPs are titled as the core and shell, respectively. This type of structure is required especially when the shell is composed of a material with surface-activity, e.g., Pt, Pd, Rh, which are suitable for catalysis, and the core exhibits some modifying feature like ferromagnetism, which is usually connected with Fe, Co, Ni [10, 87]. The formation of core-shell structures can occur when one of the elements has lower surface energy. This rule comes from general theoretical and experimentally verified findings [88, 89]. Especially for immiscible elements or elements with a miscible gap, surface energy plays the main role in the atoms segregation in the particle. Nevertheless, if the elements are well miscible, the formation of segregated atoms on the surface belongs to the element exhibiting a significantly higher melting temperature [80].
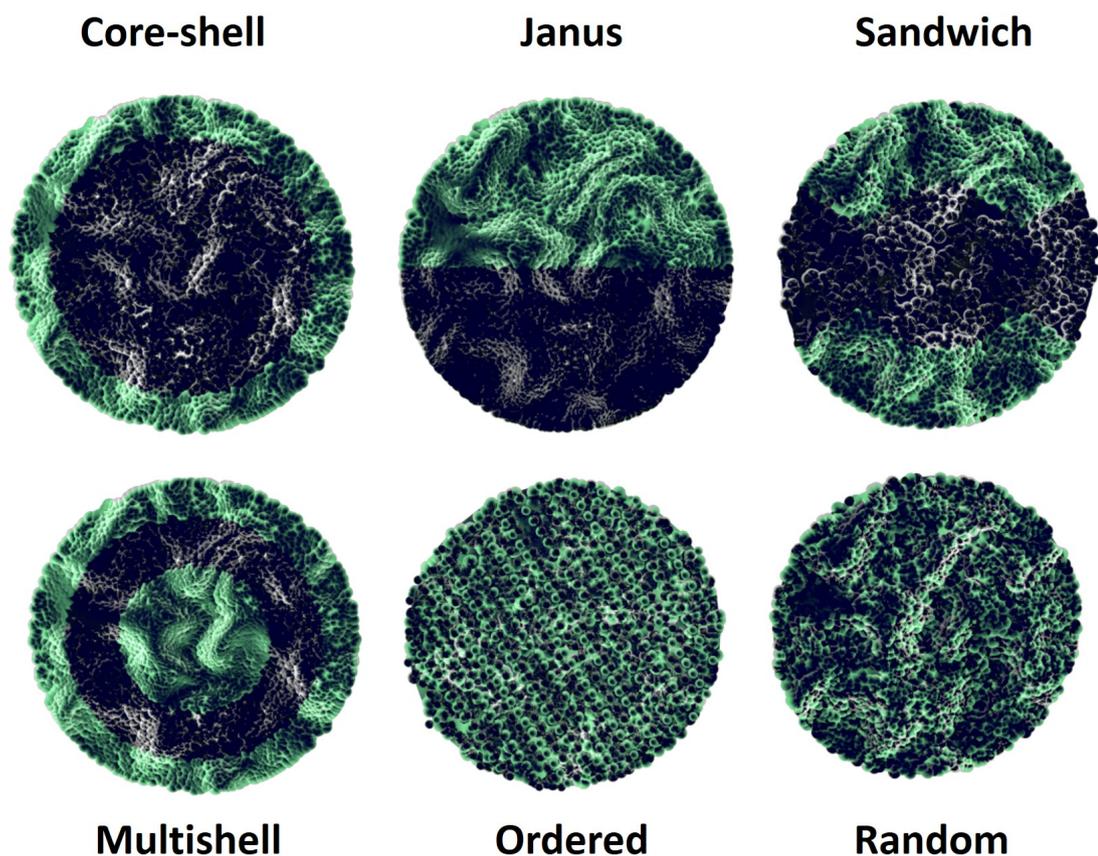
Figure 3.1: Nanoalloys categories according to their way of alloying

The core-shell nanoalloys represent one of many possible structures of nanoalloy. When a new layer of atoms is added to the core-shell structure, it is considered a multishell structure observable in, e.g., Cu-Ag, Ni-Ag, Pd-Ag, Pd-Au nanoalloys [79]. Besides, the nanoalloys without central symmetry can be divided into Janus and sandwich particles. The Janus nanoalloys are usually composed of two different atom sides, which enable nanoalloys to behave dependently on the facing side of the particle. The nanoalloy with one type of atom on its top and bottom is known as a sandwich. Finally, we can assort the nanoalloys between the ordered mixed and randomly mixed nanoalloys. The ordered mix is formed with an inner pattern as alternating lines of different atoms. Thus, it is probable to expect their anisotropic behavior. Nevertheless, their behavior should be the most similar to the randomly mixed nanoalloys. When the nanoalloy does not exhibit any order, they can be classified as randomly mixed, whereas the most representative members of this nanoalloy family are solid solutions [79, 90].

The presented configurations constitute the chemical type of nanoalloys ordering, which significantly depends on the used synthesis methodology. Moreover, new types of nanoalloys composition can be discovered in the future [90]. Recently, the scientific group of Prof. Barcikowski [91] was able to synthesize a new type of nest

nanoalloys, which look like small NPs incorporated in the structure of a bigger one.

As previously discussed, the nanoalloys can serve as suitable mediators of catalytic reactions, especially in heterogeneous catalysis. The choice of metals, which should be incorporated in their structure, is essential for the final performance of the nanoalloy catalyst. First, the structure must include the catalytically active material, which can be represented by the palladium, one of the best elements in the field. Moreover, when the requirement on the heterogeneous catalyst is the re-use of the material, the easy separation of catalysts from reaction followed by cleaning of catalyst is desirable. Thus, the great catalysts may include the nickel as a magnetically active motor of the nanoalloy. Moreover, the low cost of the nickel in comparison with the palladium makes from the Pd-Ni nanoalloy an (Fig. 3.2) affordable catalyst with an excellent performance [79, 80, 83, 89], which can be even higher than the one of pure particles [92].
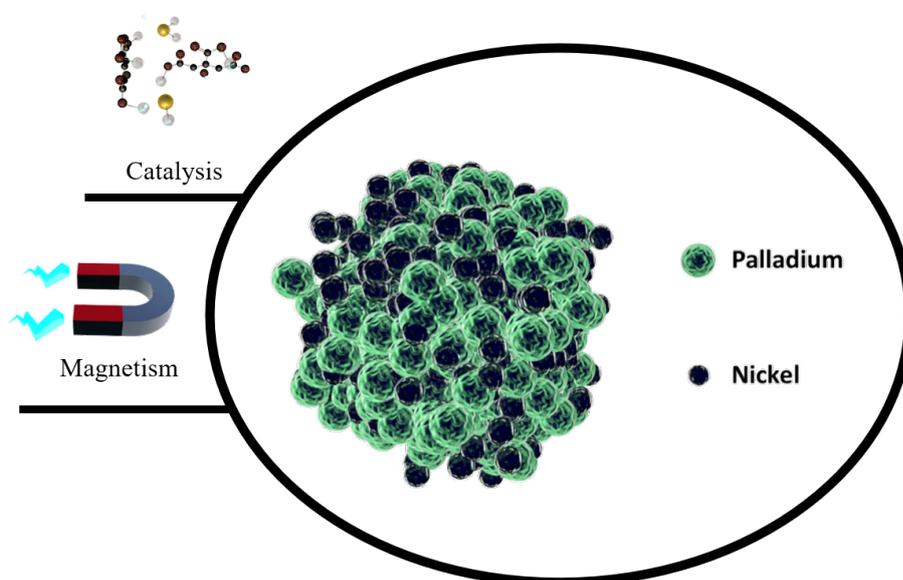
Figure 3.2: Randomly ordered Pd-Ni nanoalloy and its most significant features - extreme catalytic activity and ferromagnetic behavior

4 Graphene

In recent years, graphene has been considered one of the materials predestined to the future world and a pioneering material, which discovery brought interest in the so-called 2D materials. The history of graphene dates back to the year 1947 when the Canadian physicist P. Wallace wrote a theoretical study about the 2D carbon nanostructures' existence, including the graphene [93]. Later, in 1986, the graphene term was first mentioned in connection with a specific carbon modification [94]. Graphene itself is composed of carbon atoms that form a mono-atomic layer. The carbon atoms are arranged in regular hexagons in this layer, resembling the shape of a honeycomb, connected by sp^2 bonds. This type of structure is the main reason why graphene has many exceptional properties and provides a fruitful ground for applications [95].

If we could connect several layers of graphene together, these planes would form the human world's abundant graphite material that an ordinary person can find in any pencil. In fact, the pencil was the precursor for the first successful preparation of graphene. Although the 2D materials such as graphene were originally assumed to be stable only at temperatures around absolute zero due to the Mermin-Wagner theorem [96], this theoretical assumption was refuted at the beginning of the 21st century. The reason why the 2D structure does not collapse into itself, as the theorem predicts, is the wavy shape of the graphene structure, which prevents the collapse of the plane due to thermal fluctuations [97].

As graphene is only one of many carbon structures, we must ask ourselves what makes it so special that it is now referred to as 21st-century material. Why did the graphene become interesting to countless scientific groups around the world? The answer lies in its outstanding properties, which were already described by the discoverers - Prof. Geim and Prof. Novoselov. The list includes high charge mobility 2000–5000 $cm^2/V \cdot s$ [98], high optical transparency reaching 97.7% [99], high thermal conductivity 5000 $W \cdot m^{-1} \cdot K^{-1}$ [100], high Young's modulus of elasticity 1 TPa [101] and a large specific area of 2630 $m^2 \cdot g^{-1}$ [102], among others. In summary, the long listing of properties gives a satisfying answer to the uniqueness of graphene.

In 2004, Prof. Geim and his former doctoral student Prof. Novoselov managed to prepare one atomic layer of graphite, which is, in fact, the graphene, by tearing off the layers of the graphite using an adhesive tape (the principle of mechanical exfoliation) [103]. This method was ineffective and would be pretty impractical to prepare a sufficient amount of graphene for commercial applications. Therefore, many articles were published on alternative methods for the fabrication of graphene [104,

105] and its potential applications [99, 105] with a huge number of citations (e.g., in the catalytic field - Fig. 4.1).
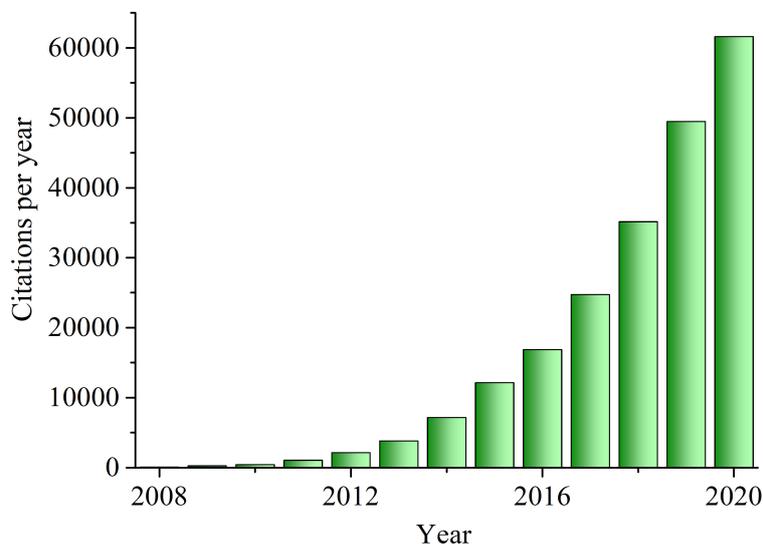
Figure 4.1: Number of citations per year determined by the ISI Web of Science search engine, while using the keywords "graphene" and "catalyst".

The use of graphene for catalysis has two points of view. As it was mentioned, the modern catalysts include 1-3 parts - active catalyst, promoter, and support. Specifically, the graphene can be used as the active catalyst or supporter [106]. Electrochemical catalysis is one field where graphene can find applications as an active supporter. Graphene has been used countless times since its discovery to catalyze chemical reactions [107, 108]. The graphene itself exhibits a very low electron density, which is commonly associated with poor electrocatalytic properties. Even if the graphene plane is oriented directly to the analyte, no electrocatalysis occurs at all. The electrocatalytic performance is improved when we increase the number of graphene layers to 8 or more [109], but such a structure is something between graphene and graphite. However, the electrochemical performance of graphene itself can also be enhanced by inducing defects (e.g., alkoxy, -CO groups) [110].

Although the catalytic activity of graphene is out of researchers' study, the use of graphene as support is tremendous [44, 111]. The unique properties, together with its abundance in scientific labs, make graphene a basic model for the testing of two-dimensional catalytic supports [44].

Among other characteristics, the adsorption constitutes the main parameter for the decoration of the support by catalysts like NPs. The adsorption mechanism of the metal NPs and graphene-based material is based on the charge transfer between them. The binding of the atoms over the graphene material can be made into three positions (Fig. 4.2) - at the center of a hexagon (H position), at the midpoint of a carbon-carbon bond (B position), and above a carbon atom (T position). Based

on the previous studies, the Ni atoms adsorb on H position, while the Pd atoms adsorb on B and T positions due to the nearly filled d-shell. The type of atom also plays a significant role in the quality of adsorption [44]. In the case of Pd and Ni, chemisorption between the atoms and graphene occurs, which makes these atoms higher adsorbed on the graphene surface than other ones, e.g., Au, Ag, or Cu, absorbed by physisorption [112].
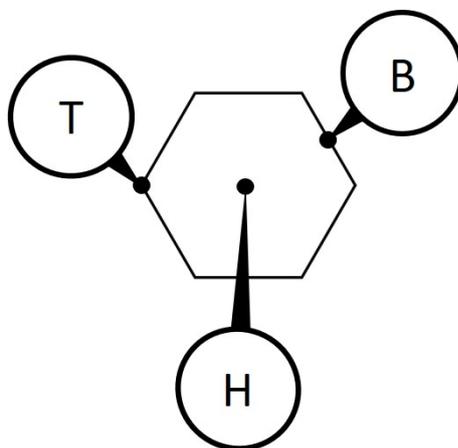
Figure 4.2: Scheme of adsorption positions over graphene structure: hollow (H), bridge (B), and top (T)

The alternative graphene-based material for catalysis is represented by graphene oxide. Since graphene is usually prepared with intermediate in the form of graphene oxide, the difference between graphene and graphene oxide is only a reduction process. From the point of properties view, the successful reduction increases the material's conductivity enormously, which is beneficial for catalysis. However, the methodology of reduction leads to the increase of defects, which negatively influence the conductivity and quality of material itself [44]. In summary, the ideal methodology for the fabrication of graphene from graphene oxide would reduce oxygen-based groups from graphene oxide structures without damage to the graphene plane.

4.1   Graphene preparation

Like many other materials, graphene applications require a method of preparation that meets in particular three parameters - high production speed, simplicity of the method, and low cost. The first technique used by the professors of the University of Manchester meets a single parameter, namely the simplicity of the method, although not completely. For this reason, right since the birth of graphene research, it has become crucial to find a more suitable method. Most methods have been based from the beginning on the so-called Hummer methods [113], which allow the synthesis of graphene oxide. As the name suggests, it is a layer of graphene that has oxygen attached to its surface. With the help of potent oxidizing agents and strong acids, the individual graphene layers are separated from graphite.

The subsequent process for the preparation of graphene from graphene oxide occurs through reduction; the graphene thus prepared is called reduced graphene oxide. Reduction techniques are extensive and can be divided into thermal [114] and chemical types of reduction [115]. A very successful chemical reduction can be performed, for example, with hydrazine [116]. However, this method is not very safe, and its alternative using DMSO (dimethyl sulfoxide) [116] does not represent an improvement from the point of view of sustainable (green) chemistry. Nevertheless, the alternative methods for green reduction of graphene oxide exist [70, 117, 118].

Other methods of graphene preparation include liquid phase exfoliation [119], ion implantation [120], epitaxial growth on a silicon carbide substrate [121], and chemical layer deposition (CVD) [122]. These preparation techniques are characterized by the ability to produce significant amounts of graphene [122]. Among the mentioned methods, the chemical deposition of layers has proved to be the most promising over the years. Moreover, the ability of CVD to prepare pure graphene with 90% of the theoretical strength also helped [123]. In addition, when copper is used as a substrate, it is possible to form single-layer graphene on 95% of the substrate's surface [124], which is another significant advantage of the method.

The produced graphene can also be divided into two basic categories - graphene flakes up to 100 μm in size and continuous graphene [125]. Graphene flakes can be well prepared by the previously mentioned liquid-phase exfoliation, even by preparing graphene directly from graphite without an intermediate phase with graphene oxide. This fact brings certain advantages, such as a substantially lower number of graphene defects caused by the synthesis [126, 127]. The mentioned CVD method is suitable for the preparation of continuous graphene, the production rate of which can be around 5 cm/min [122, 128].

The preparation of graphene-based material forms only one step in the creation of a new catalyst. Since the Pd-Ni NPs are prepared to decorate the graphene-based nanosupport, the unique laser technology, which is used for the preparation of active catalyst part, should be discussed.

5 Laser synthesis

Modern nanotechnology includes many nanofabrication techniques bringing to the world amazing nanomaterials, which can be classified as materials with one or more of their size dimensions under 100 nm [129]. Thanks to this specification, the scientists divide the nanomaterials into 0D, 1D, 2D, 3D according to the number of dimensions overcoming this condition. A typical representative of 0D nanomaterials is NPs with all dimensions in the nanometer scale [130].

The fabrication techniques allowing the preparation of NPs can be divided into different categories, e.g., chemical vs. physical [131] or green vs. hazardous techniques [131, 132]. Another relevant category is based on a change of the nanoparticle precursors size (Fig. 5.1). The top-down techniques prepare NPs by reducing precursor size till the moment of nanoparticle formation. Besides, the bottom-up consist of the matter self-organization phenomenon, while the NPs must grow from atomic precursors. The bottom-up procedure is typical for wet chemical methods [133, 134].
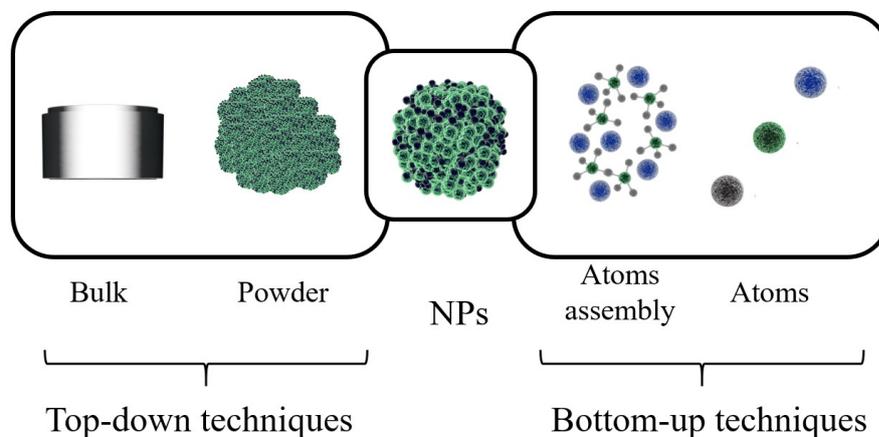
Figure 5.1: Scheme of two basic strategies for NPs synthesis differing in the NPs' precursor size

One of the most promising techniques for the preparation of nanomaterials, especially NPs, is the laser synthesis and processing of colloids (LSPC). In general, the LSPC technique represents a green synthesis approach enabling the production of NPs by physicochemical phenomena. The NPs preparation is mediated by a high-power laser irradiating a material usually immersed in a liquid, while the interaction between the laser's light and the matter leads to the formation of new nano-sized

species in the liquid environment [4]. The nascent colloid is composed of the liquid and the NPs with micrometer size to even under 3 nm in diameter [135].

The LSPC methodology has been discovered by the first research studies in the late 80's [136], and early 90's [137]. Since the seminal studies, the LSPC, also known as laser synthesis, has been developed to the maturity [138]. The methodology has a great potential to overcome the options and performances of other techniques by its versatility, simplicity, and effectiveness. [4] The laser synthesis benefits (Fig. 5.2) include the formation of ligand-free NPs (stabilized in special cases by macromolecules or monovalent salts [139]), low costs [140], safeness during preparation, a wide spectrum of preparable materials, the mentioned chemical sustainability, automation [36, 141], and room pressure and temperature conditions during the fabrication process. In addition, the sustainability of the technique consists of non-use of hazardous agents and no production of chemical waste [4], which enables us to avoid the environmentally detrimental effects representing one of the biggest challenges in the modern science [142]. Nowadays, due to all these benefits, the technique is gathering a great deal of attention, which can be proven by the increasing number of citations (Fig. 5.3).
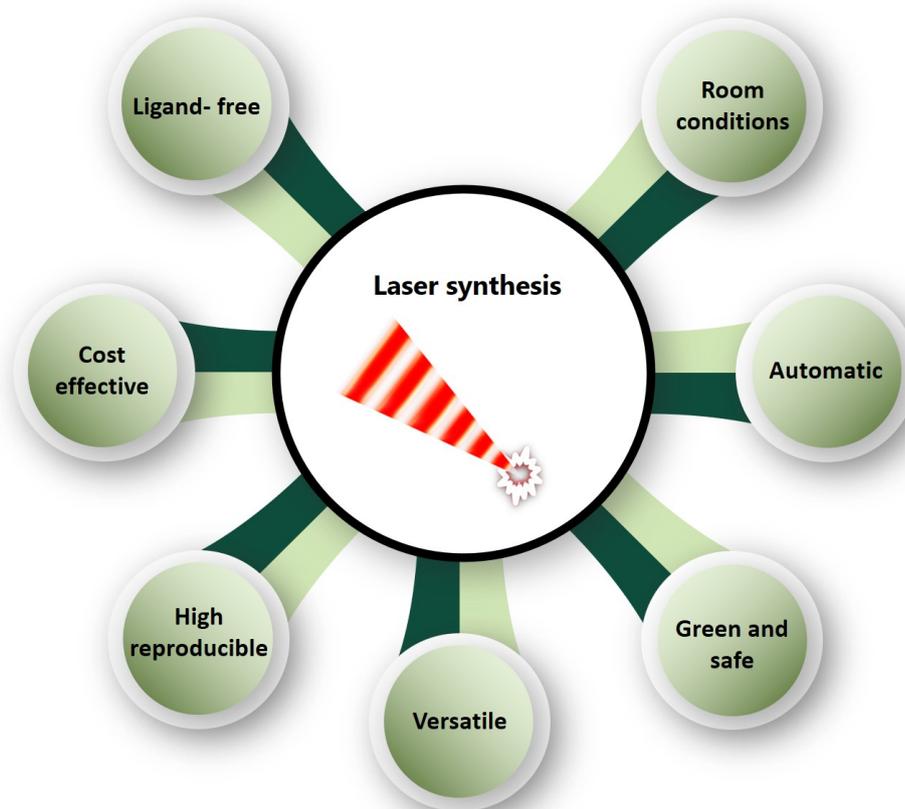
Figure 5.2: Main advantages of the laser synthesis and processing of colloids technology

As it is usual for technological advances, the LSPC brings some drawbacks.

For instance, the impossibility to directly synthesize organic NPs due to the high temperature inside of the process, which leads to the possible organic matter's incineration [4]. However, the main drawback is the low productivity of the methodology, which is currently being addressed by various perspectives. Specifically, the mass productivity has been positively influenced by the use of a laser with high pulse repetition [143, 144], the circular polarization, laser-induced periodic surface structures (LIPSS) formation [145], and the choice of optimal liquid [146]. In a long-term view, the methodology will become cheaper and cheaper thanks to the advances in the laser technologies, mainly due to the higher power and lower investment to the most expensive part of NPs production - an investment in the laser device [4].
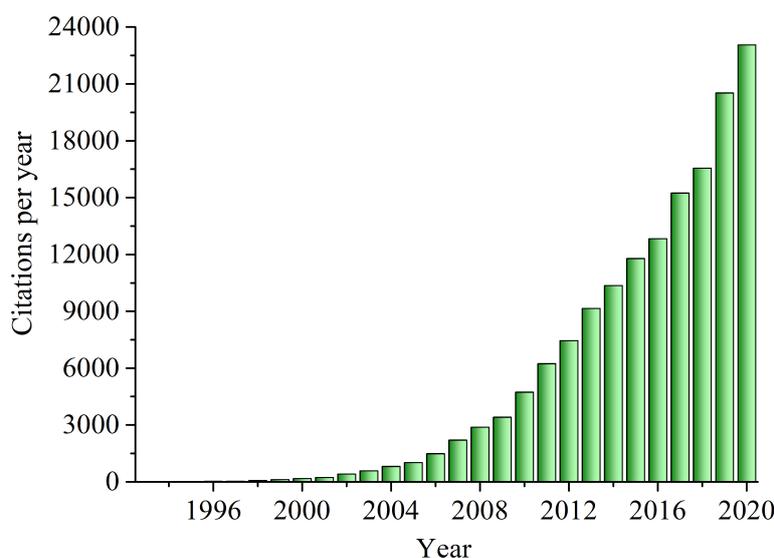
Figure 5.3: Number of citations per year determined by the ISI Web of Science search engine, while using the keywords "laser synthesis" and "nanoparticles".

Regarding the laser source, the LSPC can be promoted by two different types of instruments: continuum wave lasers (CW-lasers) and pulsed lasers. The principle of CW-laser-mediated LSPC consists exclusively of thermal effects. Briefly, the relatively low power laser beam continuously irradiates the sample by the photons coming from the instrument. The absorbed photons are transformed into energy in the form of thermal vibrations, which move through the material. The accumulated energy enables the material's melting, evaporation, or explosion. Then, the continuous irradiation of the sample leads to many undesired effects - a relaxation of thermal energy into the surrounding medium and cavitation bubble shielding, among others [4, 147]. All phenomena decrease the production yield, cost-effectiveness, controllability, and creation of cross-effects [146, 147, 148]. In summary, the CW-laser does not represent a good promoter of the LSPC.

On the contrary, the use of a pulsed laser enables us to avoid the mentioned drawbacks. During a pulsed laser-mediated LSPC, high energy of pulses, including

a high density of photons, is transmitted to the sample in an ultra-short time, making the pulsed laser an ideal source for promoting LSPC [147]. In the first place, the extreme peak power reaches the NPs formation threshold effortlessly. Secondly, the ultra-short duration on the fractions of a second does not give enough time to the material to significantly transform the energy into vibrations, suppressing the undesired effects.

Specific LSPC effects are different in the case of pulsed laser synthesis, where the pulse duration has the principal role in the effects [147]. In this context, the most employed pulsed laser are the nanoseconds, picoseconds, and femtoseconds (ns or 10^{-9} s, ps or 10^{-12} s, and fs or 10^{-15} s). The attosecond lasers with pulse duration on the level of 10^{-18} s have not been used for this methodology yet.

The suggestion that higher peak power and shorter time must lead to the best LSPC results is valid in the case of μs and ns lasers. The lasers promote thermal effects, as it is in the case of the continuous laser. Although, the undesired effects disappear, which is more significant in the ns laser pulse duration that is short enough to allow only a negligible release of energy to the surrounding liquid before the NPs creation.

The behavior of NPs creation becomes more complicated for shorter pulse durations, specifically, on the level of 100 ps and less [147, 149]. The extremely high power associated with these pulse durations could result in non-linear optical phenomena as the optical breakdown, self-focusing, filamentation effects, and cascade ionization, among others [4, 150]. One of the most important effects is the electron-phonon relaxation time, which appears in the region of ps [151] permitting the ps and fs lasers to completely avoid the release of energy in the form of heat. Here, the phenomena (Fig. 5.4) responsible for the nanoparticle's creation is a multiphoton ionization phenomenon. Besides, the non-linear optical phenomena happening in the liquid can lead to the movement of the laser's focal point, which causes an energy loss before the beam gets in contact with the sample [147].

Finally, the LSPC includes five basic methods, which are known as the laser ablation in liquids (LAL), laser melting in liquids (LML), laser fragmentation in liquids (LFL) [4], laser defects engineering in liquids (LDL) [150], and laser photo-reaction in liquids (LPL) [85, 138, 152]. The desired phenomena for each of them are different, and thus also different lasers are required.

5.1 LAL

The laser ablation in liquids (LAL) or, more specifically, pulsed laser ablation in liquids (PLAL) represents the leading technique in the LSPC field. The laser ablation setup configuration is based on the irradiation of a bulk material, which is usually an ultra-pure thin metal foil, immersed in a surrounding liquid environment by a high-power laser. The surrounding liquid ideally must be transparent or low-absorbing for the used laser wavelength. This condition guarantees effective laser ablation [150].

Since the LAL is generated in a transparent liquid, the laser-matter interaction on bulk target leads to plasma formation in a few hundreds of picoseconds. In case
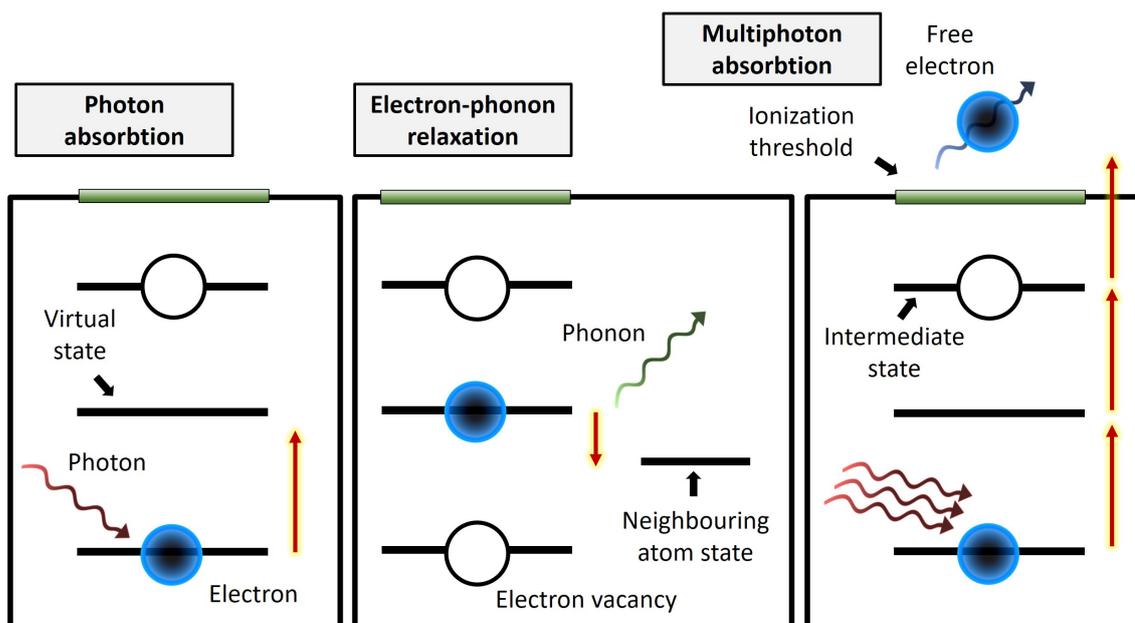
Figure 5.4: The scheme of light-absorbing electron phenomena promoted by ultrafast lasers

of fs laser, the mechanism responsible for a plasma creation is the multiphoton-ionization, which is described in the previous chapter. Together with the formation of plasma, the little pieces of material are released from the bulk. After a cooling of plasma, the removed matter is enclosed in a cavitation bubble coming from a fast volume expansion around the area of the laser-matter interaction. The expansion occurs together with a phase transition of the surrounding liquid due to locally destabilized conditions. The pressure can be enhanced to gigapascals at the laser focal point. At the moment of cavitation bubble creation, the bubble around the irradiated area mediates the transfer of energy from the irradiation point to the liquid. The cavitation bubbles have a characteristic time of existence depending on the laser pulse duration and its energy. After the bubble collapses, the particles are released into the surrounding liquid environment, resulting in the final colloid. As it was confirmed by the small-angle X-ray scattering (SAXS) technique, the area where the bubble collapse includes a lot of energy, which can lead to the creation of a second cavitation bubble followed by another one. The creation of new bubbles depends on the laser, environment, and primary cavitation bubble features. In addition, the dynamics of cavitation bubbles play an essential role in the final production of LAL and the phenomena that occur inside the ablation reaction, e.g., the creation of nonlinear optical effects or a decrease of an ablation yield. Although, not only the cavitation bubbles influence the LAL fate significantly [4, 150].

The laser parameters, especially its fluence, wavelength (Fig. 5.5), and pulse duration, bring a lot of advantages, disadvantages, opportunities, and challenges in the field. Firstly, an increase in the laser fluence leads to the higher productivities of the NPs. Nevertheless, a threshold limit must be considered due to the appearance
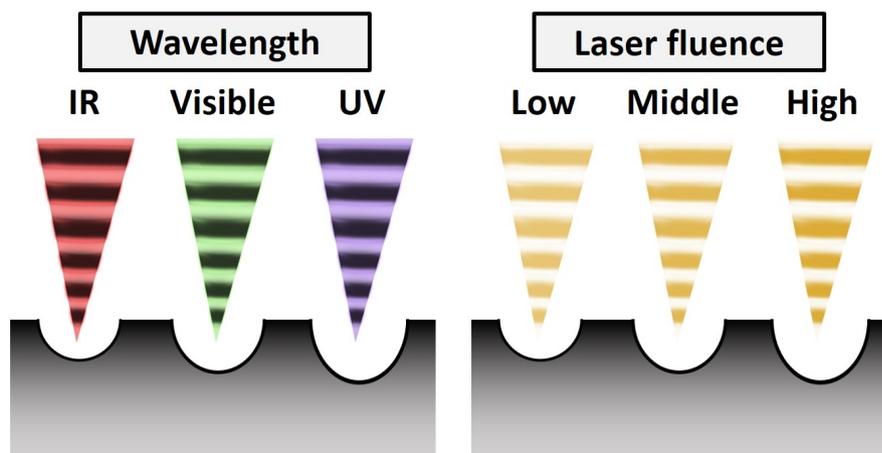
Figure 5.5: Influence of different laser wavelengths and fluences on the material detachment out of a solid target

of nonlinear optical effects. For instance, the self-focusing and the filamentation effect in the liquid environment have been observed for high laser intensities ($>10^{17}$ W·m^{-2}). However, these effects enormously decrease the productivity of the NPs. Secondly, the lasers with a shorter wavelength like ultraviolet (UV) lasers enable higher production per pulse compared to the visible or infrared (IR) ones. Nevertheless, the LAL in the case of UV lasers can be affected by the self-absorption of laser light by already produced NPs. The localized phenomenon leads to the production decrease and the secondary undesired LML and LFL effects in the colloid. This connection makes the ablation reaction more complex, and the combination of another uncontrolled effect with LAL can lead to wide size distributions and phase heterogeneity of NPs, among others. Last but not least, the pulse duration, which has been already discussed, dominates the effects of LAL. Especially for LAL, two processes are mostly discussed - thermal loss and plasma shielding. The negative effect known as a thermal loss decreases the effectivity of ablation most dramatically in the case of longer pulse duration. Oppositely, the pulses shorter than 10 ps avoid losing energy due to the negligible electron-phonon coupling effect, which has been mentioned before. For ns or sub-nanosecond lasers, the thermal loss of energy is supplemented by another negative effect - plasma shielding. The laser-mediated plasma formed due to the LAL, which in the case of ps and fs lasers disappears, changes the material's conditions and protects it from effective ablation.

In summary, the most effective lasers for LAL are those with high laser fluence, low pulse duration, and high repetition rate, e.g., from kHz to several MHz. Nevertheless, a moving scanning laser beam must be used to avoid the cavitation bubble shielding (Fig. 5.6). This kind of lasers enables the highest production rate, while the low yield is one of the biggest drawbacks of the methodology [4, 147, 150].

The laser ablation became, through time, a competitive technique for the preparation of NPs, which can be comparable with the most used wet chemical techniques [138]. Since the LSPC represents a methodology with an advantage in the high controllability of the final NPs composition and almost unlimited versatility,
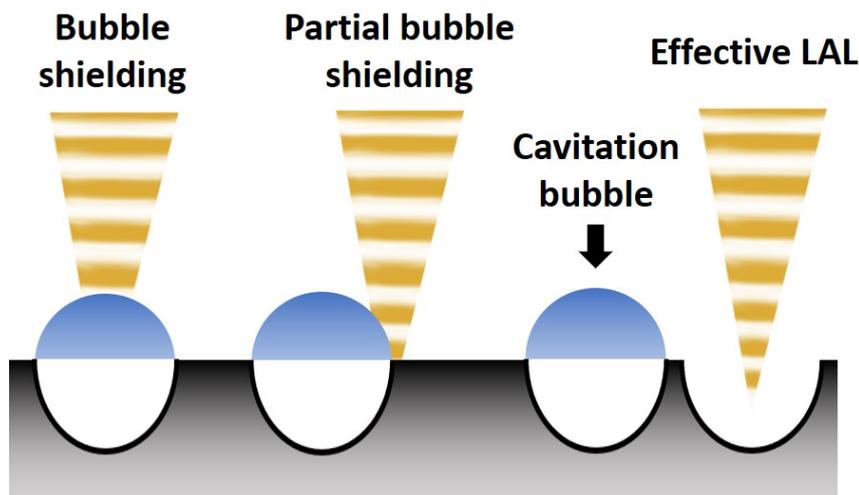
Figure 5.6: Scheme of beams position influence on effectiveness of LAL from the perspective of the cavitation bubble creation

the scientific progress push the LAL to the production of precisely defined nanoalloys as bimetallic nanostructures [37, 38] with outstanding features, e.g., 4D behavior [153], higher biocompability [154], etc. The irradiation of bimetallic foil mainly ensures the synthesis of bimetallic nanoalloys in a liquid environment [39, 40, 41, 154, 155, 156]. Nevertheless, LAL is not the only methodology enabling nanoalloys synthesis; the alternative can be found in reactive laser ablation in liquids (RLAL).

5.1.1 RLAL

In recent history, LAL has been connected with laser photo-reaction in liquids (LPL), which resulted in creating a new laser technique for the generation of NPs - RLAL. The methodology is similar to LAL (Fig. 5.7) [157]. In general, the experiment consists of irradiating a metal target immersed in a liquid environment, which contains another metal NPs-precursors (e.g., metal salts or powder material) [158].

From the perspective of timescale, the creation of NPs by RLAL is not direct. During RLAL, the irradiated material is immersed in the water with a NPs-precursor. First, the laser forms a plasma in the water by reaching its optical breakdown and generates free electrons in the liquid. Moreover, the intensive beam also ejects electrons from the material surface by multiphoton ionization. All electrons are formed in a few tens of fs and become hydrated until several hundred fs. The hydrated electrons interact with the NPs-precursors immersed in the water and start to reduce them in hundreds of fs to tens of ns. The reduced species form atom clusters and start to coalesce. The plasma created in the liquid contains hydroxyl radicals, which are transformed continuously to hydrogen peroxides immersed in the solvent in the range of ns and μs. The reaction between hydrogen peroxide and reduced NPs precursors leads to the autocatalytically-mediated growth and subsequently to the large NPs formation [157].
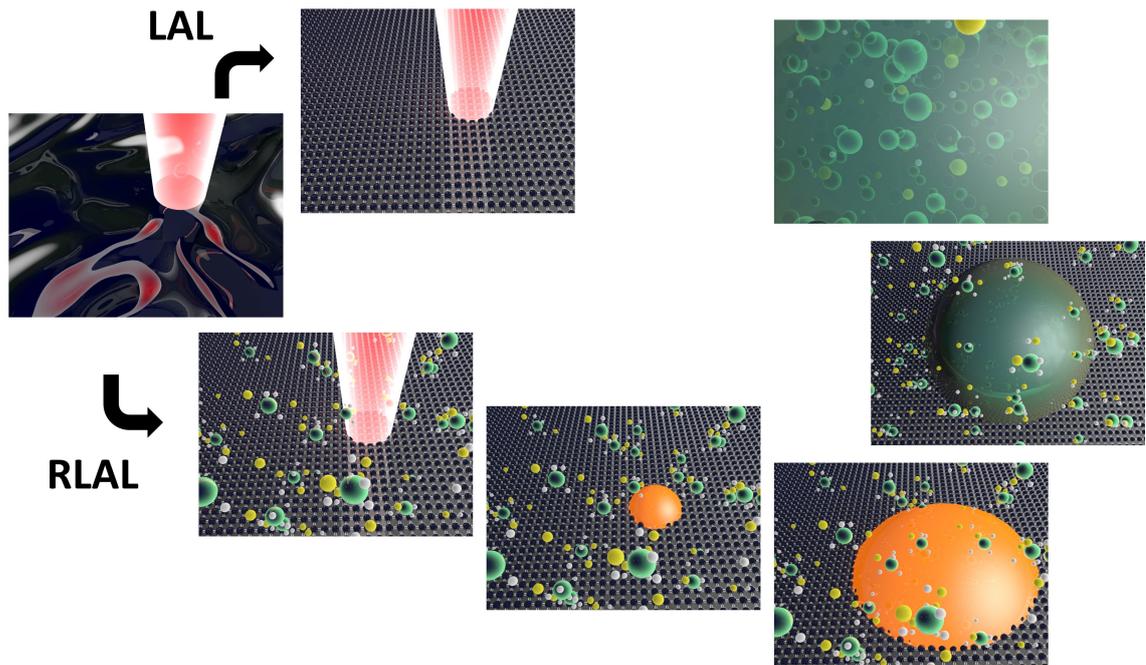
Figure 5.7: Scheme of RLAL mechanisms and initial difference with LAL

During this process, a second line of the NPs formation starts. The irradiated material is deprived of electrons on its surface, leading to electrostatic repulsion and release of target atoms after tens or hundreds of ps since the experiment started dependently on the used material. Later, there is a release of bigger droplets of material from the target in a range of several ns. The material coming from the target on the sub-ns timescale serves as a stabilization agent for the new type of NPs formed from the NPs-precursors or their atom clusters [157].

The two mechanisms of NPs formation in two different timescales can also result in two different size distributions [157]. The following mixture process can result in the formation of tight junctions between the created species. Subsequently, the junctions mature into NPs in the cavitation bubble serving as a nano-reactor. After the bubble collapse, the final NPs get a structure of nanoalloys with elements mixed in a single particle [158] or eventually the colloid includes NPs surrounded by a nanostructured matrix [157].

In summary, the RLAL has already been shown to be an alternative technique for the preparation of new nanomaterials [159, 160, 161, 162, 163]. Nevertheless, not many scientific studies have been done, and shadows still hide all the aspects of this promising technique.

6 Characterization techniques

As a part of the thesis, the fabricated nanomaterials were characterized by many electron- and photon-based analytical techniques, among others. The chosen analysis with state-of-art devices includes ultraviolet-visible spectroscopy (UV-Vis spectroscopy), high-resolution transmission electron microscopy (HR-TEM), energy-dispersive X-ray spectroscopy (EDX), selected area electron diffraction (SAED), inductively coupled plasma mass spectrometry in single-particle mode (spICP-MS), Fourier-transform infrared spectroscopy (FTIR), Raman spectroscopy, high-performance liquid chromatography (HPLC), and vibrating sample magnetometry (VSM). The complete analysis of samples or their parts gives complex information about the chemical and physical structure of the nanocatalyst and its performance.

6.1 UV-Vis spectroscopy

In general, spectroscopes are devices that use light or, more precisely, electromagnetic radiation to study the matter. Since the variety of wavelength regions have a different impact on the studied material, the instruments are divided based on the region of used light.

UV-Vis spectroscopy uses light from the ultraviolet region to the near-infrared region. A halogen lamp can produce the whole spectra with a tungsten wire. The individual wavelengths from the halogen lamp spectra are separated in the instrument (Fig. 6.1) by a diffraction grill and interact wavelength by wavelength with the colloidal sample placed in a cuvette. The transmitted light reaches the detector and the instrument compares the amount of light going through the sample and the theoretical amount, which should come from the halogen lamp.

The gained value represents the transmittance of the light (eq. 6.1), which is finally recalculated to the absorbance of the light (eq. 6.2)

$$T_\lambda = \frac{I}{I_0} \tag{6.1}$$

$$A = -log_{10}(T_\lambda) = -log_{10}(\frac{I}{I_0}) = \frac{ln(e^{\alpha(\lambda)d})}{ln(10)} \cong \frac{\alpha(\lambda)d}{2.3} \tag{6.2}$$

where I_0 is the incoming light beam intensity, I is the outgoing light beam intensity measured by a detector, λ is the light wavelength, α is the absorption coefficient of the sample, and d is the beam path in which the light interacts with the sample in the cuvette.
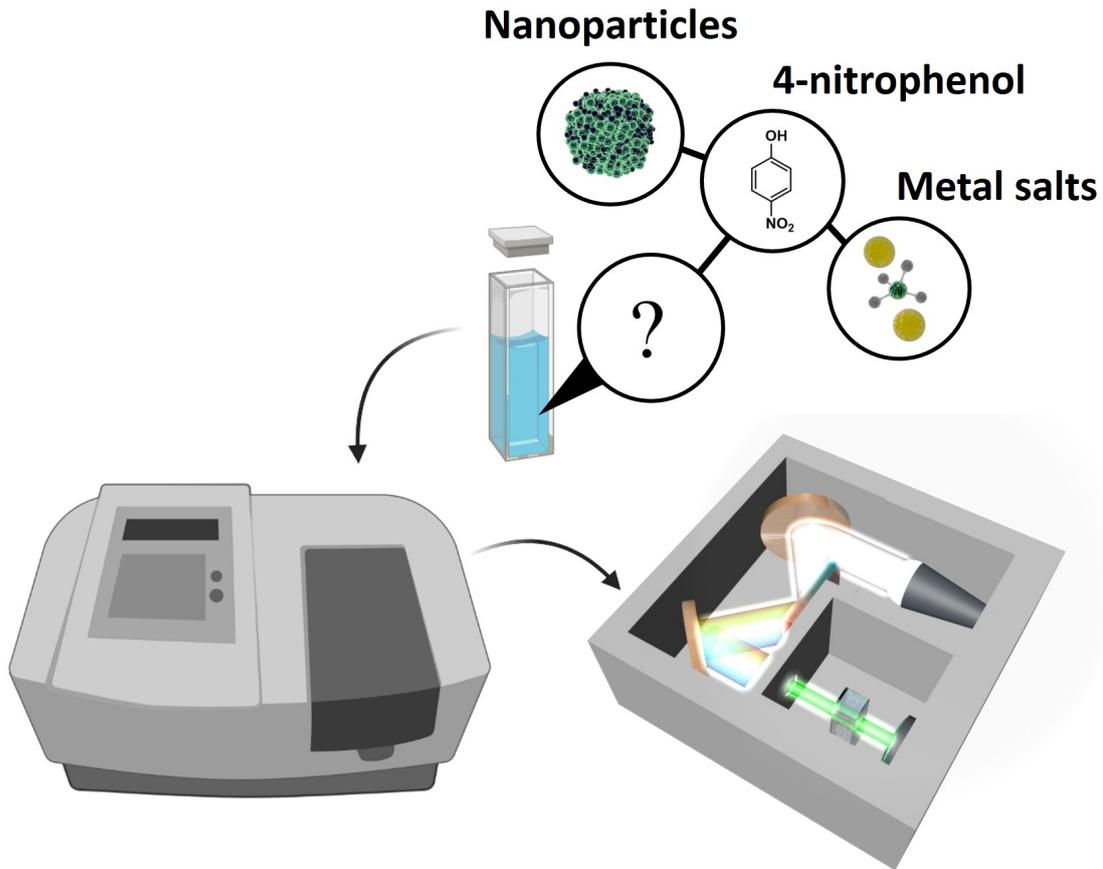
Figure 6.1: Principle of a spectrophotometer enabling the analysis of various samples. Image created with the help of BioRender.com

The UV-Vis technique enables us to test the optical properties of nanomaterials by determining the absorption spectra of the samples, e.g., nanoalloys. Besides the spectra of absorbed light, the technique allows us, e.g., to compare the concentrations in different colloidal samples (eq. 6.3), to observe Ni-based and Pd-based NPs creation, and to follow reaction dynamics of 4-nitrophenol reduction.

$$A = \epsilon_\alpha c d \tag{6.3}$$

In combination with the Mie-theory calculator, the UV-Vis graph can give a reasonable estimate on the particle size and nanoalloy structure. The basic assumptions of particles' sphericity, homogeneity, and planarity of light waves must be fulfilled. In that case, the NPs interaction with light can be described by the following formulas [164]:

$$C_{ext} = \frac{24\pi^2 R^3 \epsilon_d^{3/2}}{\lambda} \frac{\epsilon_m''}{(\epsilon_m' + 2\epsilon_d)^2 + (\epsilon_m'')^2} \tag{6.4}$$

$$\epsilon'_m = \epsilon^\infty - \frac{w_p^2}{w^2 + \gamma^2} \tag{6.5}$$

$$\epsilon''_m = \frac{w_p^2 \gamma}{w(w^2 + \gamma^2)} \tag{6.6}$$

$$\gamma = \frac{v_F}{L_{bulk}}, \tag{6.7}$$

where C_{ext} is the extinction coefficient of the spherical particle, R its radius, ϵ_d the material's dielectric function, ϵ_m the dielectric function of the environment where the particles are located, ϵ^∞ the dielectric function at high frequencies, w the frequency of the incoming light beam, w_p the resonance frequency of the electron-light interaction in the particle, v_F the Fermi velocity coming from the Fermi energy, and L_{bulk} the electrons' pathway in the 3D material.

The assumption of homogeneity is much more difficult to meet for multi-metallic NPs such as nanoalloys. Nevertheless, the mentioned formula could be modified for some particular types of multi-metallic NPs, e.g., core-shell structure [165]. Therefore, the final spectrum hides information not only about the particle size and composition, but also about the element distribution in the particles together with the shell and core diameters.

In summary, the UV-Vis analysis gives us basic information about the bulk behavior of the created NPs. Nevertheless, the individual parameters of the particles must be later analyzed by HR-TEM, EDX, and SAED techniques.

6.2 TEM

Today, we meet many different devices and techniques in science and industry, allowing us to observe materials and their morphological structure. One of the primary classifications distinguishes methods based on the signal provider. As the most common example, photons are used in the light optical microscope (LOM) or electrons in electron microscopes. As this thesis includes research of nanomaterials, the electron microscopes represent the best option for the observation. The usual LOM does not enable nanometer-size object observation due to the low resolution resulting from the long wavelengths of the visible light. According to the design of the microscope and the type of electrons that are detected, we distinguish between transmission electron microscopy (TEM) and scanning electron microscopy. The higher resolution and opportunity to determine crystallographic families and defects make the HR-TEM the top choice to analyze individual crystal-forming nano-sized specimens.

The analysis process starts with an electron gun - mostly a bright LaB_6 hot cathode, which serves as an alternative to a hot cathode source formed by a tungsten wire or to an auto-emission source. By using a LaB_6 cathode in the shape of a tip, the electrons dissipate towards the sample due to the voltage induced at the positively charged anode, which is placed near the cathode. High voltages between tens of kV and 300 kV are commonly used. Thanks to this voltage, the electrons are highly

accelerated, overcoming the energy needed to transmit through the sample. The successful transmission of electrons requires a tiny sample around 100 nm thick in the holder composed of a copper grid and a carbon film serving as a support of the specimen and a background in the pictures (Fig. 6.2). The low and precise height of the sample enables an accurate analysis with a relatively high signal of outgoing electrons.
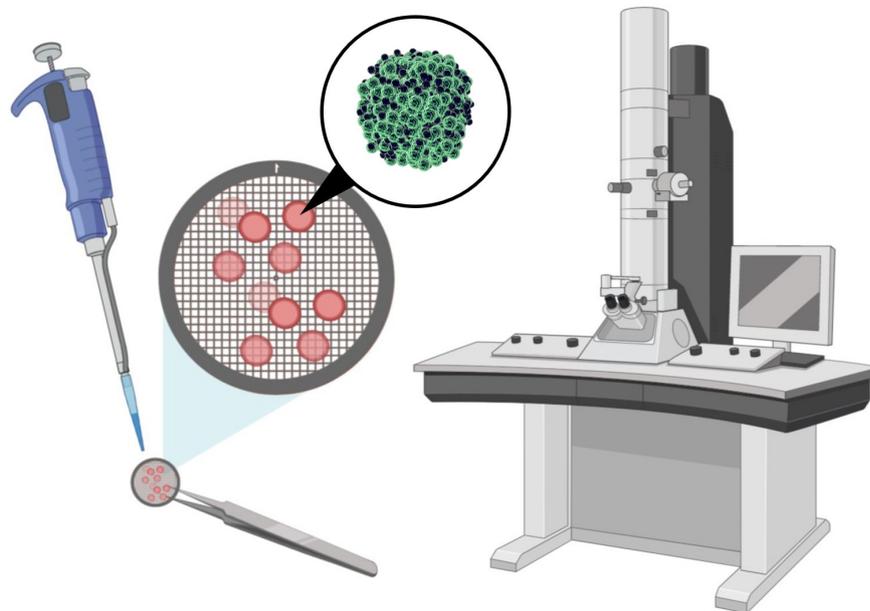
Figure 6.2: Scheme of a TEM instrument and the preparation of a thin sample on the grid. Image created with help of BioRender.com

The electrons themselves are directed in the tube by a condenser electromagnetic lens before interaction with the sample. Subsequently, the objective lens gathers light from the sample. In comparison with photons, the electrons also react with atoms and molecules ordinarily present in the air. Thus, the whole apparatus needs to be enclosed in a vacuum tube to prevent adverse effects on the electron beam caused by the environment commonly found in laboratories.

The mechanism inside of the instrument is based on electron collisions on the sample. The interaction between the accelerated electrons and the sample leads to electron scattering and transmission. The successfully transmitted electrons, which are under the interest in TEM, are collected by a charge-coupled-device (CCD) camera at the bottom of the instrument. The signal on the camera is extremely precise, with a resolution under 0.1 nm. However, the correct preparation of the sample plays a vital role in the final images. Firstly, the particles are on the holder, usually in the form of a droplet, which is subsequently dried, and the sample can be introduced in the TEM instrument.

After the TEM analysis, the size and morphology of the material placed on the grid are known, but there is a lack of information about its chemical composition.

This can be managed by energy-dispersive X-ray spectroscopy (EDX), of which detector is usually placed in electron microscopes.

6.3 EDX

The electron probe microanalysis (EPMA) is one of the methods of structural analysis based on the measurement of the characteristic X-ray radiation emitted from the material. The radiation process begins when focused electrons pass through the sample in the instrument. Among other phenomena induced by the electron-matter interaction, the X-ray Bremsstrahlung occurs and manifests itself in the form of X-ray radiation with characteristic energy. This specific X-ray signal is supplemented by an X-ray background and is detected by the X-ray spectroscope. Since the electrons are used as a promoter of radiation, the EPMA is usually attached to an electron microscope. It can be a transmission electron microscope (TEM) or a scanning electron microscope (SEM).

An essential condition must be fulfilled to get X-ray radiation effectively in the electron microscope. The primary electron must overcome the energy necessary to eject some sub-valence electron from the sample's atoms. Subsequently, the energy state of the ejected electron is replaced by another atom's electron from a higher state, and the electron transition to a lower energy state (electron vacancy) leads to the release of characteristic radiation. The impending alternative phenomenon is based on the transfer of the electron's energy to another electron from a higher level, and the radiation in the form of a photon does not occur. This third mentioned electron is ultimately released from the atom and is known as the Auger electron.

Each mentioned phenomenon (Fig. 6.3) gives different information about the sample. The characteristic X-ray photons are specific for each element, and therefore EPMA allows us to determine the type and relative amount of elements in the sample. Moreover, the EPMA analysis can be performed in a point (small area), in a line, or an extended area. The EPMA spectrum can be measured as dependent on the X-ray radiation intensities on their energy or their wavelength in all the mentioned techniques. When measuring energy dependence, the methodology is known as energy-dispersive X-ray spectroscopy (EDX).

In EDX, a Si(Li) detector or a silicon drift detector (SDD) is used. The Si(Li) detectors have two essential parts - a collimator and a cryostat used for cooling. The collimator has a window, e.g., from Be glass, which transmits X-rays. However, at the same time, there are electron traps in the collimator, which prevent the detection of unwanted electrons emitted from the sample, an X-ray detecting crystal, and a field-effect transistor (FET). As soon as an X-ray photon is captured in the crystal, an electron-hole pair is formed; subsequently, a charge is separated from it by an overvoltage. In the FET transistor, the separated charges are converted to voltage, which is amplified to be easily detected. The detection is provided simultaneously for all energies thanks to the multiple channels included in the instrument. Finally, the resulting spectrum is created in the software. In the case of SSD detectors, the structure and principle are similar. However, these detectors are much faster, and

it is easier to cool them, and thus they represent the best choice in modern devices.
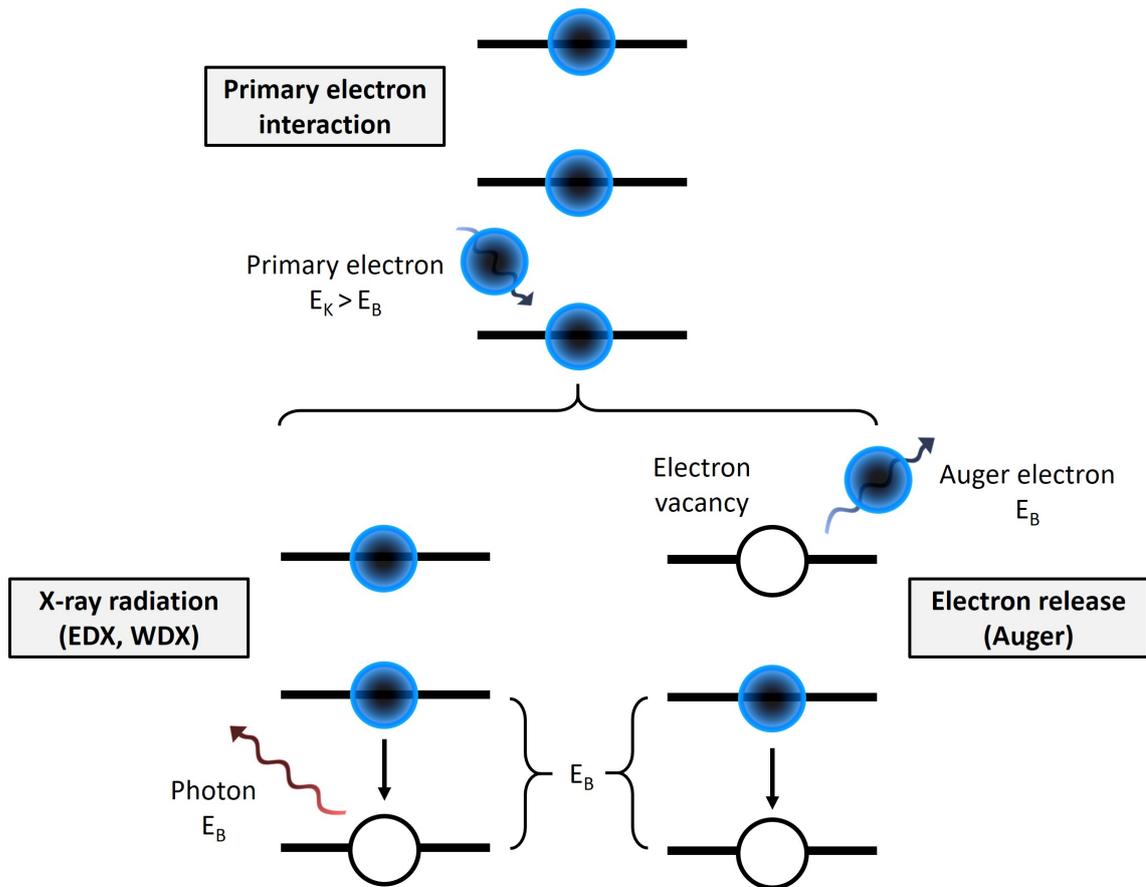
Figure 6.3: Interaction of primary electron with atom's electron and phenomena analysed by EPMA or Auger spectroscopies, where E_b is the kinetic energy of released species

An alternative method to EDX encompasses the determination of X-ray intensity depending on its wavelength. This method that uses X-ray diffraction on a crystal to separate individual wavelengths is known as the wavelength-dispersive X-ray spectroscopy (WDX). The detected angles, which provide information about the sample, are given by Bragg's law and meet the diffraction condition. A proportional counter provides radiation detection. The pulses are converted to voltage, and a spectrum is subsequently loaded, as in EDX. However, unlike EDX, the measurement is single-channel; thus, the reading of the spectrum is gradual.

Comparing EDX and WDX, it is clear that the EDX's instantaneous spectrum reading enables the method to be faster, while WDX is a more accurate technique with less noise and more detailed peaks. Furthermore, the EDX analysis has a much higher detection limit for elements than the WDX method. In summary, both techniques enable an excellent analysis of the elements with the proton number belonging to the boron and higher ($Z \geq 5$). In the case of lighter elements, electrons' fall process from a higher level to an empty state is improbable or impossible from a theoretical point of view.

Although EDX analysis affords information about the chemical composition of samples, a prediction about the patterns (crystals) formed by the atoms in the particles is not given. Therefore, to look more deeply into NPs' crystals, a diffraction method is required.

6.4   SAED

Although various diffraction techniques have already been presented, the selected area electron diffraction (SAED) represents an ideal methodology to analyze our samples. Unlike X-ray diffraction (XRD), which examination area encompasses several centimeters, in SAED, the possibility to measure crystallographic data on selected areas, e.g., several hundred nanometers in size, including only a few particles. Thus, the selection of area makes SAED an accurate method enabling the study of particles with lower concentration. Moreover, the electron diffraction (Fig. 6.4) can be taken in the same TEM instrument as the previous characterization techniques. The requirements on the sample are the same as for the transmission microscopy.
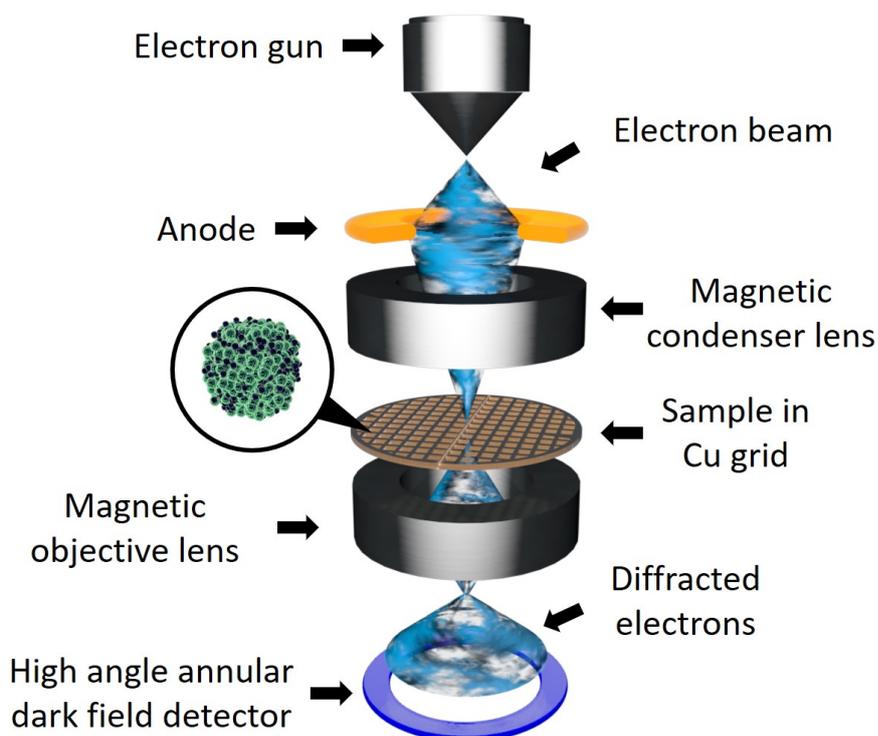
Figure 6.4: Scheme of a TEM instrument during the SAED analysis of a sample

During the measurements in the electron microscope, a crystalline sample placed in a Cu grid is irradiated by a perpendicular electron beam coming from the electron gun. The highly accelerated electrons have an energy of hundreds of keV, and

a significant number of them passes through the thin sample ($\sim$100 nm). During the passing, the electrons interact with atoms present in the material. The mentioned electron-matter interaction can be interpreted as an interaction between the electromagnetic waves and the fixed material points. This statement comes from the short wavelength of the accelerated electrons (level of picometers - 10^{-3} nm) and the average distance between the atoms, which is usually on the level of angstroms (10^{-1} nm). The material acts as a grid, and the behavior of electrons can be described by Bragg's law (eq. 6.8).

$$n \cdot \lambda = 2 \cdot d \cdot sin(\theta), \tag{6.8}$$

where n represents the refractive index of the material, λ the wavelength of electrons, d the space between atoms, and θ the angle between the incoming beam in a perpendicular direction to the plane of the atoms. Consequently, the specific periodic composition of atoms in crystals causes scattering of electrons to the specific group of angles.

The created diffraction image consists of bright spots. These selected area diffraction pattern (SADP) enables the determination of the crystal. The spots in the SADP meet the diffraction condition of Bragg's law, and the distances in them constitute a reciprocal lattice of the origin crystals. The level of material crystallinity significantly influences the final SADP not only in specific diffraction angles but also in the shapes of patterns. Since the diffraction is made on a single crystal, the individual spots stand out in diffractograms. For vast amounts of material (polycrystalline materials), many crystals are presented in the sample, and their various orientations are also detected. Thus, polycrystallinity leads to the creation of ring patterns and the amorphous materials do not show any kind of SADP.

6.5 spICP-MS

Besides the details about the size, morphology, seminal information about the chemical composition, and types of crystals, the finding of samples' elemental compositions is desirable. The extremely precise technique with an ultra-low detection limit of material like optical emission spectroscopy or mass spectroscopy serves as the ideal technique for the characterization. In our case, the inductively coupled plasma mass spectroscopy was used to get the precise analysis and get information from its single-particle mode.

Briefly, the inductively coupled plasma mass spectroscopy (ICP-MS - Fig. 6.5) technique is based on atomization and ionization of samples' elements by an argon plasma in an instrument. Before the analysis, the samples must be transformed into a homogeneous solution to ensure the easy and complete ionization of atoms in the whole sample by collisions with accelerated argon ions forming the plasma and protecting the instrument from contamination. The whole process starts with the connection of the instrument with the sample container, which is responsible for continuous injection of the sample in a nebulizer. Here, the sample forms an aerosol, which is then transformed into sample ions by collisions in argon plasma, as it

was mentioned. Electromagnetic coils maintain the plasma with a high-frequency magnetic field at the level of MHz. The ions of individual nuclides are formed and enter into a mass spectrometer. Here, the ions are separated based on the m/z (ion mass per charge) by a mass analyzer (e.g., quadrupole one) and subsequently go towards the detector.
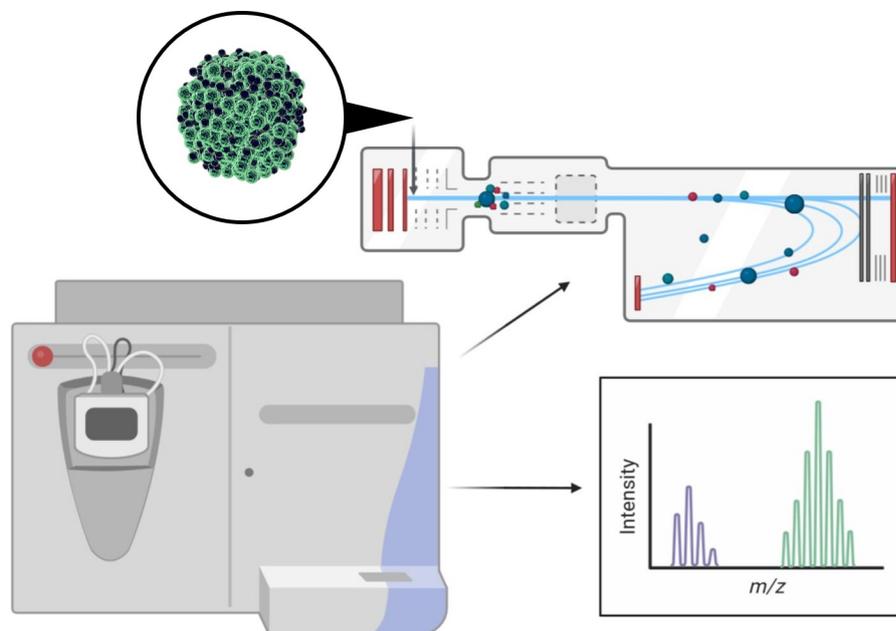
Figure 6.5: Scheme of an ICP-MS instrument with its basic principle and usual data report. Image created with the help of BioRender.com

The observed intensity signal of each nuclide ion is directly proportional to the concentration of the respective element. This fact makes the instrument ideal for quantitative analysis. Conventionally, the instruments make many measurements and the results are expressed as the average for each presented nuclide. The total measuring time for one nuclide is from several seconds to a few minutes. The final results constitute mass concentrations calculated from intensities and calibration. The low measuring time and statistically-based results can be included in the benefits of the methodology. Nevertheless, the options can even be enhanced by the single-particle mode of the instrument, so-called spICP-MS.

The origin of spICP-MS dates back to the beginning of the 21st century [166]. The technique provides information about individual NPs in the sample, which can be mono-metallic or multi-metallic, and the technique is used to determine the distribution of NPs' sizes calculated from the mass of particles. The injecting samples are in the form of a highly diluted dispersion (even tens of ng/L) and the duration (dwell time) of individual analysis is set to a range of milliseconds or even hundreds of microseconds, which enables the detection of individual particles embodying signal peaks (Fig. 6.6).

The number of detected peaks corresponds to the number of NPs in the diluted sample P (eq. 6.9).
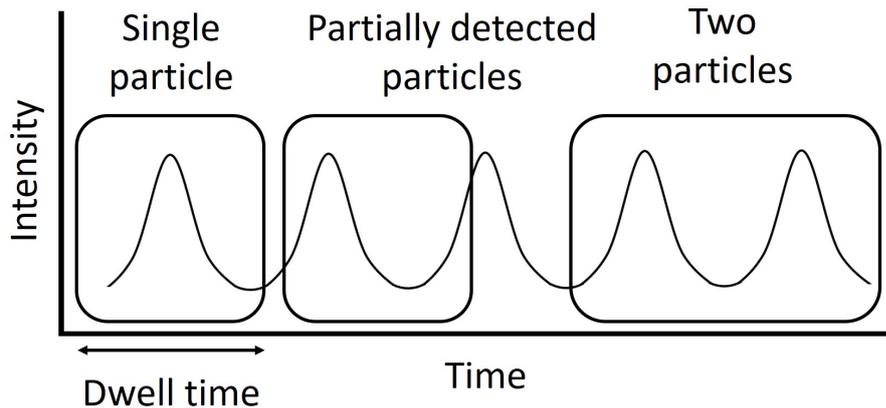
Figure 6.6: Scheme of particle signals detected during spICP-MS and the configuration of dwell time

$$P = \frac{f}{K \cdot T},$$ (6.9)

where f is the average number of peaks per time, K is the sampling flow rate, and T is the transport efficiency of nebulization. The information can be extended by considering the peak area, which enables determining the size of particles. Thus, the instrument software can create a size histogram of particles, including from a fraction of millions to hundreds of atoms. For this, it is necessary to prepare the corresponding calibration and assume a spherical shape of particles. For spherical particles, the diameter of NPs d_p can be calculated by the equation 6.10.

$$d_p = \frac{S}{w \cdot \psi} = \left(\frac{6 \cdot m}{\pi \cdot \rho_p} \right)^{1/3},$$ (6.10)

where S is the peak area of the nanoparticle signal expressed in count units, w is the weight fraction of the detected element in the sample, ψ is the tangent line of the calibration curve of S versus the mass of the detected element, m is the mass of the nanoparticle, and ρ_p is the density of the nanoparticle element. In summary, these simple calculations and technique features enable us to connect results from bulk and single-particle analysis.

6.6   HPLC

Chromatography constitutes a methodology used for the separation of individual components from a mixture. In general, the technique enables high-quality component differentiation and precise quantitative detection. The qualities result from a mechanism based on the different affinity of components to the so-called mobile and stationary phases. The analysis starts with the injection of a mixture with components in the mobile phase. Subsequently, the mixture in the mobile phase

continues to the separator column with the stationary phase. The flowing mobile phase carries the components through the stationary phase, and the different affinity of components causes their spatial separation. Finally, the components are step by step exposed to the UV-Vis spectroscopy and the intensity of the specific component content is determined.

Since the mobile phase plays a key role in the process, the chromatographs can be divided based on the different mobile phases - gas (gas state), plasma (ion current), fluid (supercritical fluid state), and liquid (liquid state) chromatography. A modern type of liquid chromatography is high-performance liquid chromatography (HPLC - Fig. 6.7), also known as high-pressure one, which serves as an excellent technique to separate the organic pollutants as 4-nitrophenol (4-NP) or its reduced form 4-aminophenol (4-AP). These compounds were under study in this work.
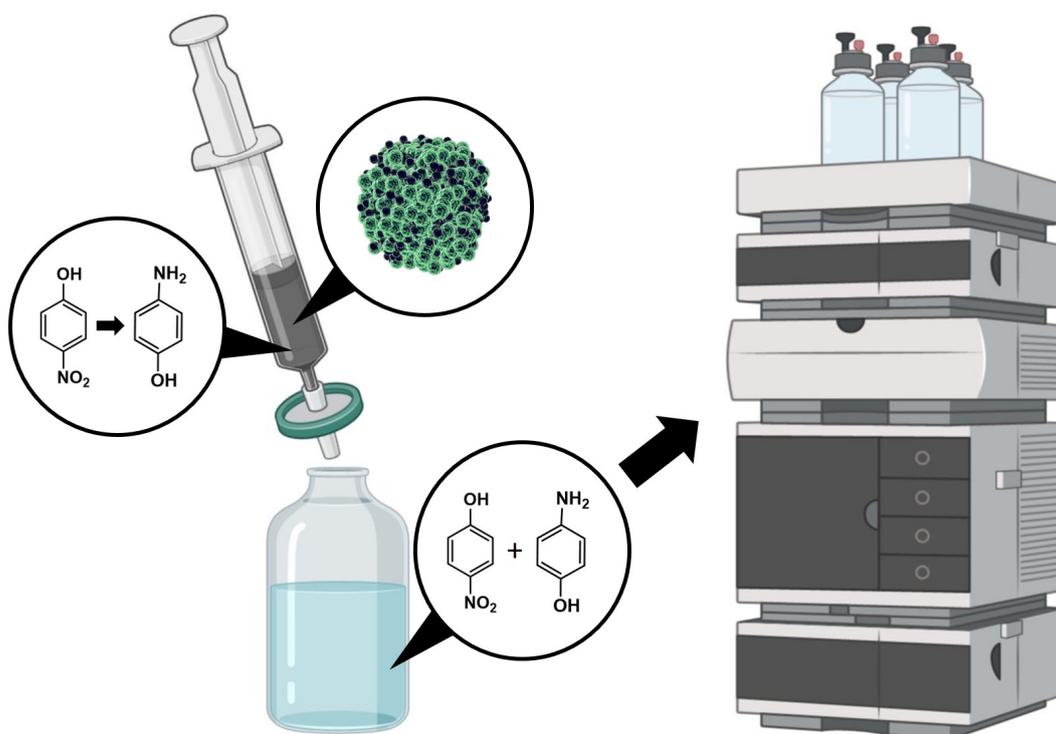
Figure 6.7: HPLC instrument and sample prepared for HPLC performance. The injection taken from chemical reactor includes the degrading 4-NP with NPs. The NPs are filtrated from liquid to stop catalytic reaction. Image was created with the help of BioRender.com

6.7 Vibrating-sample magnetometry

Vibrating-sample magnetometry (VSM) is a widely used and sensitive technique used to measure the magnetization of a sample. The specimen which is mounted in the vibrating holder oscillates in a system of coils, and it leads to the induction of a voltage on the coils due to the magnetization of the analyzed specimen.

The measured voltage can be transformed in the hysteresis loop, permeability, or magnetic moment of the sample. Especially, the hysteresis loop (Fig. 6.8) includes a lot of new details about the samples, e.g., saturation (M_s), remanence (M_r), and coercivity (H_C) values. Besides, the magnetometers enable the measurements at different temperatures, which bring new information about the material behavior and can serve to find the critical temperature of the material. In our case, the NPs were tested at the most used condition - room temperature. In addition, the anisotropy constants were calculated from H_C values based on theory of Stoner and Wohlfarth [167], using the formula:

$$K = 1.02 \cdot H_c \cdot M_s \qquad (6.11)$$
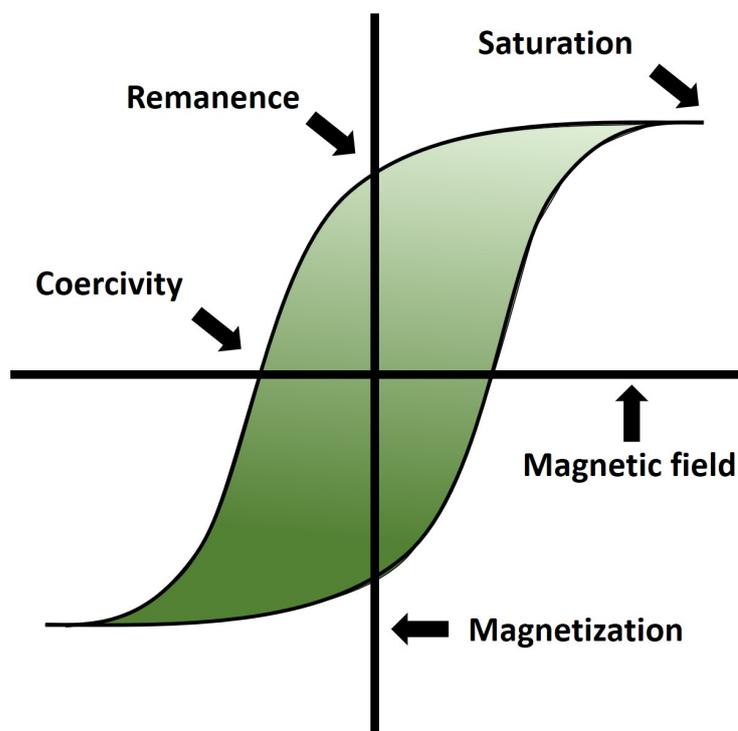
Figure 6.8: Typical hysteresis loop of a ferroelectric material

6.8   LDE

Laser Doppler electrophoresis (LDE) as a part of the dynamic light scattering (DLS) instrument (Fig. 6.9) is used to measure Zeta potential. At the same time, its value determines the electrical double layer barrier, which protects a material against agglomeration. Thus, a high Zeta potential represents a large stabilizing layer of the ions between the material and the liquid environment surrounding the material.

In detail, the used DLS device includes two electrodes that transmit an electrical current between each other, while the material in a cuvette with a liquid
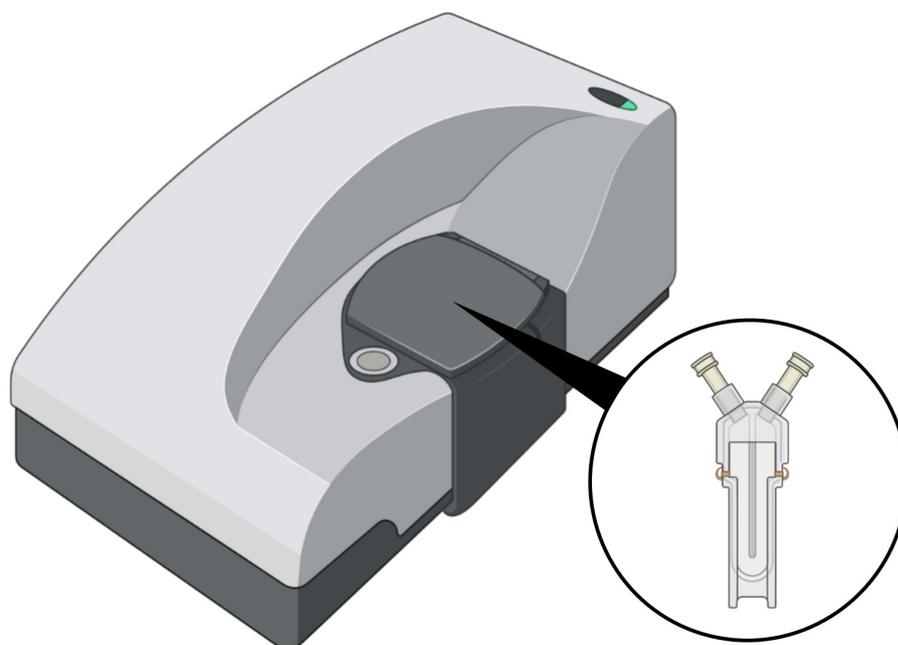
Figure 6.9: Scheme of a DLS instrument with a cell for LDE measurements. Image created with the help of BioRender.com

moves. Specifically, the material in the liquid exhibits charged surface, which is surrounded by the liquid ions. The application of voltage causes the movement of the charged species towards the instrument's electrodes. Subsequently, the device measures the velocity of the material, which is known as the electrophoretic mobility of the material. This velocity relates to the Zeta potential by using Henry's equation (eq. 6.12) [168].

$$z = \frac{\eta \cdot E}{\epsilon} \tag{6.12}$$

where, z is the Zeta potential, η the medium environment viscosity, E the electrophoretic mobility, ϵ the dielectric constant of analyzed material.

6.9   FTIR

The Fourier-transform infrared spectroscopy (FTIR) represents an analytic spectroscopic method that identifies and characterizes vast amounts of inorganic and organic compounds. The technique is non-destructive for analyzing the material and is based on the interaction of infrared laser light with the studied sample. The commonly used is middle infrared light lying between 4000-200 cm^{-1}. The energy of infrared photons, which is lower than the one of visible light, does not allow the excitation of the sample's electrons, which makes the most significant difference compared with the mentioned UV-Vis spectroscopy. Since the energy is too low to promote the change of electrons' electronic states, the laser-matter interaction

of infrared light promotes only the change of molecules' vibrational (or rotational) states. The successful change of vibration state (Fig. 6.10) is possible only for the studied molecules with chemical groups with light-changeable dipolar momentum. Therefore, only asymmetric chemical groups can start to vibrate during the measurements. Besides, the Raman spectroscopy enables the observation of not FTIR active groups. The spectra from both techniques give information about all possible functional groups. The whole set of groups in a molecule can be determined by comparing the measured sample with spectra included in databases.
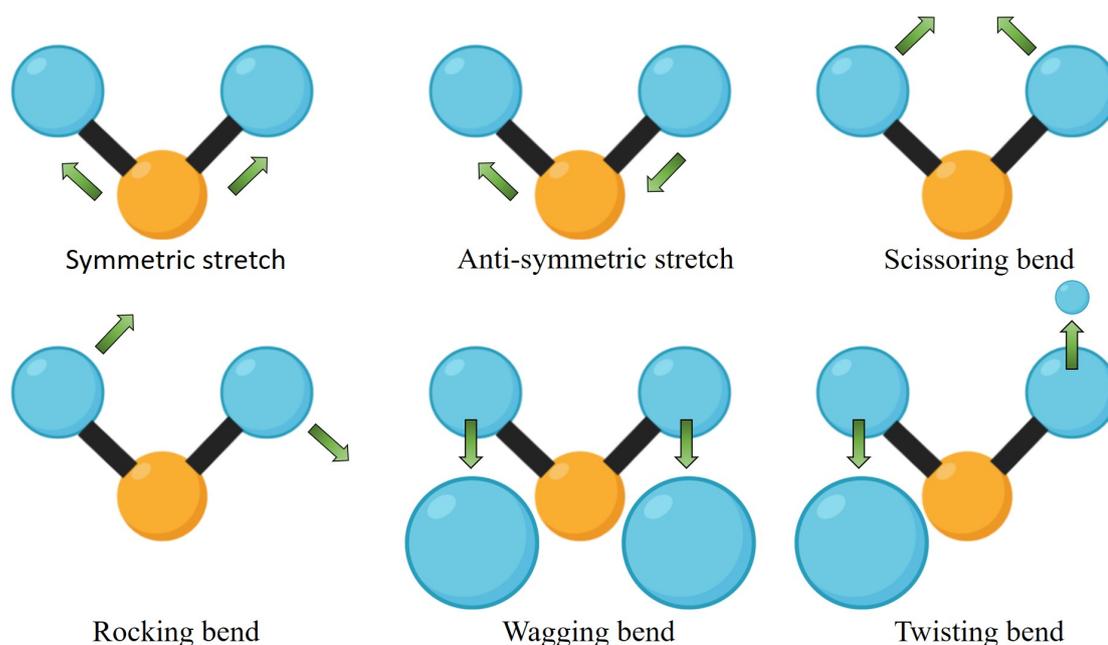
Figure 6.10: Selected kinds of molecule's vibrations excitable in FTIR

The infrared spectroscopy faced the problem with a low intensity of transmitted light in the past [169]. This problem was coming from the low energy of infrared photons. Since the 80's, a new principle using interfering infrared light transformed by the Fourier algorithm enabled to overcome the low-intensity issue. The commonly used fast Fourier transformation methodology changes an interferogram to a spectrum. This spectrum is composed of the transmitted light going through the studied sample or the calculated absorbed light. The advantages of FTIR include the fast simultaneous measurement of the whole spectrum, high signal-to-noise ratio, stable and accurate measurement, and analysis of gas, liquid, or solid samples. Nevertheless, FTIR data interpretation is not straightforward, and some detected wavelength could be typical for more chemical bonds moving; thus, a detailed discussion must be made.

6.10 Raman spectroscopy

As it was mentioned, Raman spectroscopy is a technique complementing with its results FTIR. It is a non-destructive technique that serves for the identification and characterization of inorganic and organic compounds. Its spectrum is composed of light signals showing the vibrational modes of molecules, just like in FTIR. Nevertheless, the mechanism responsible for the observation of the sample's chemical groups is different.

The lasers in spectroscopy are usually the ones with wavelength 785 nm (near-infrared), 532 (green), or 405 nm (UV), which get the sample's molecules in virtual energy states. The UV lasers represent the light source with the highest intensity of inelastic scattering, but the high fluorescence drowns the signal. The opposite situation occurs in the case of near-infrared lasers.

The analysis starts with the absorption of the laser light going through a molecule. Subsequently, the sample emits the light with the same or different energy by scattering. When the wavelength of the original laser light and the scattered one are the same, the scattered spectrum does not give any information about the inner structure of the sample. This phenomenon is known as elastic scattering or Rayleigh scattering. Nevertheless, it is also possible to observe light with higher energy (anti-Stokes scattering) or lower energy (Stokes scattering) (Fig. 6.11).
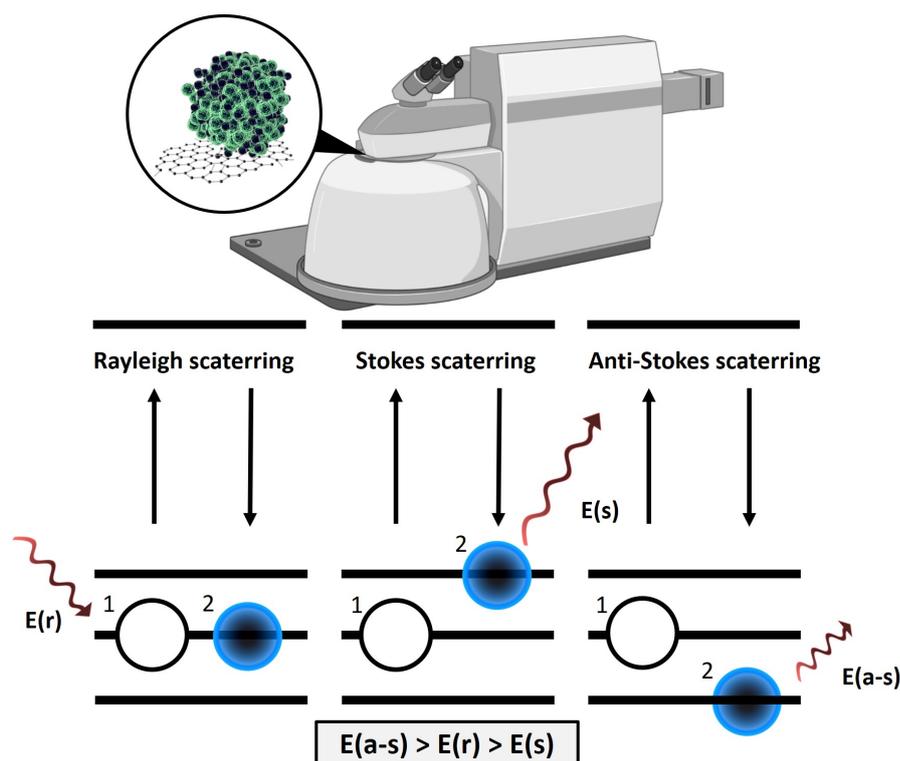
Figure 6.11: Raman spectroscopy of graphene-based sample and type of scattering phenomena promoted in the instrument. Image created with the help of BioRender.com

The mentioned scattering types are known as an inelastic scattering, which has an extremely low probability of happening; 1 out of a thousand laser photons are the Rayleigh scattered, and 1 out of 10 million photons are inelastically scattered. The mentioned rare effects occur due to the change of the molecule's vibrational energy levels. The energy of the absorbed photon can be decreased by transferring part of its energy to a molecule (Stokes scattering) or by receiving energy from the molecule, which decreases its vibrational or rotational state (anti-Stokes scattering). The Raman activity of chemical groups depends on the changeability of the electric polarizability, which results in high visibility of centrosymmetric molecules oppositely to FTIR. Whereas Raman spectroscopy is not so similar to FTIR, the primary advantages and disadvantages are similar for both techniques.

7 Methodology

7.1 Setup details

The generation of the Pd-Ni nanostructures was carried out by the high-repetition industrial femtosecond pulsed laser Onefive Origami XP-S (maximum average output power 5.1 W, pulse duration < 400 fs, central wavelength of 1030 nm, maximum repetition rate of 1 MHz, spectral bandwidth < 5 nm, and output beam of 5 mm at the width of $1/e^2$). The photon beam going out of the laser served to irradiate a nickel foil ($> 99.98\%$ Ni, thickness 0.5 mm, Sigma-Aldrich, USA) with palladium salts immersed in demineralized water (demiH$_2$O, 18.2 M$\Omega\cdot$ cm). The created laser ablation plasma on the nickel foil interacted with palladium salt and promoted a reaction, leading to Pd-Ni nanoalloys formation.
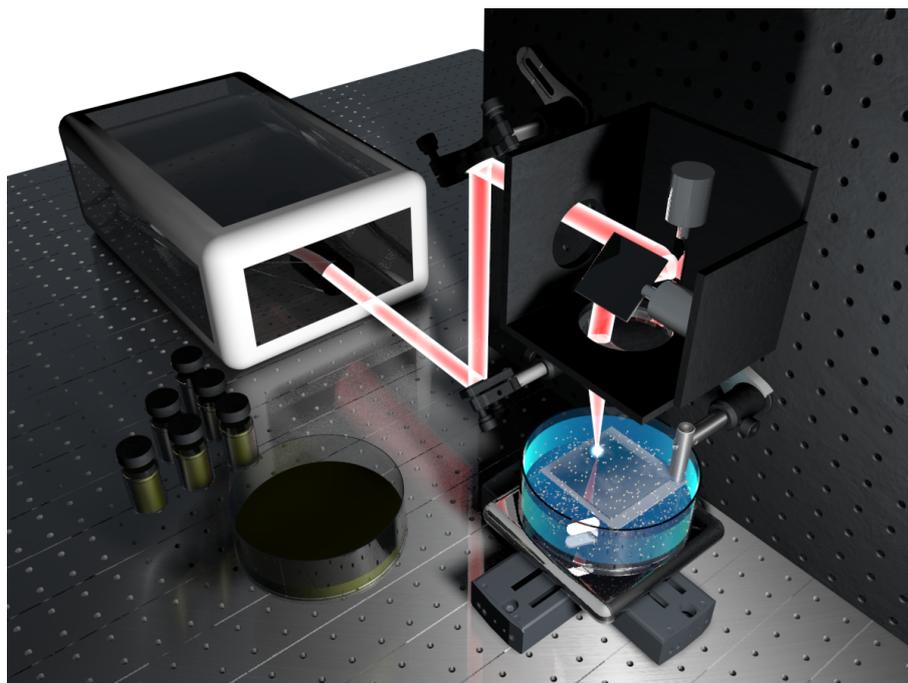
Figure 7.1: Scheme of the experimental setup used for the fabrication of Pd-Ni nanoalloys

The general experimental concept is displayed in Fig. 7.1. Firstly, the laser beam was directed by reflecting mirrors to a scanning head. This stage was followed by the

pass of the beam through the scanning head (intelliSCAN 14, SCANLAB), where the beam direction was quickly changed with the help of 2 galvanometric mirrors, which lead to the positioning of the beam above the foil. Subsequently, the laser beam was focused on the nickel foil by an F-theta lens (f = 160 mm) into a glass vessel, which contained 40 mL of an aqueous solution of potassium tetrachloropalladate(II) (>98% K_2PdCl_4, Sigma-Aldrich, USA). The vessel contained two magnetic stirrers, which served to the colloid mixing and thus to the moving of the created particles from the position above the nickel foil. The water level above the nickel foil was set to 3 mm. This low height was chosen to prevent the high absorption of the infrared laser light by the water. To avoid the cavitation bubble's shielding, the velocity of the laser scanning onto the foil secured by the galvanometric mirrors was set to the maximum possible speed level of 2 m/s. Finally, to avoid the LFL phenomenon, the laser fluence was set lower than 10 J/m^2, which is too small to promote the particles' fragmentation [170]. A precise average power and laser repetition rate were chosen based on a seminal study with the nickel foil. More details are given in the chapter "Results and discussion".

Scanning head with galvanometric mirrors

Laser beam reflecting mirror

Holder of nickel foil

High repetition laser

Surface laser pattern

Setup components

Palladium-nickel final coloid

Magnetic plate on position stage

Colloid before irradiation with magnetic stirror
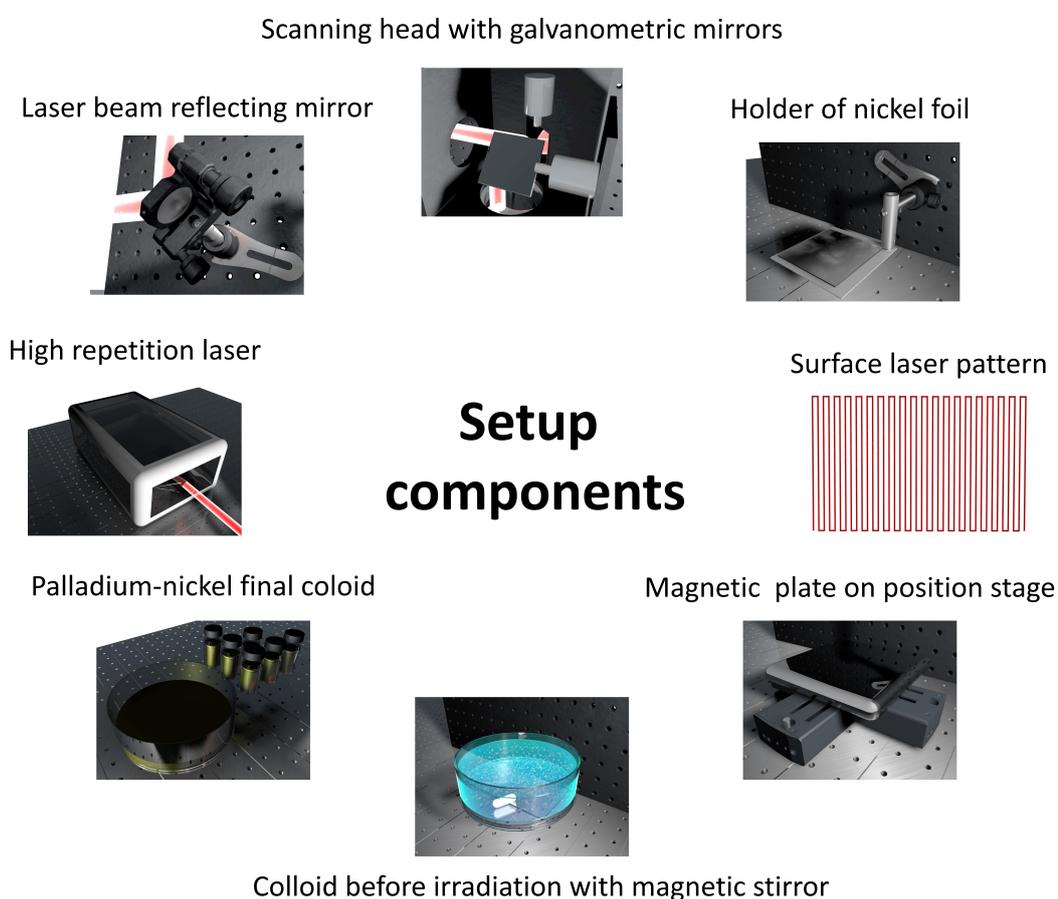
Figure 7.2: Description of the setup components used for laser synthesis

Looking into the setup details (Fig. 7.2), two parts are essential to be mentioned. First, how the shape and size of the irradiation pattern play a significant role. The

role of the scanning pattern created by the laser on the foil is hidden in avoiding any waste while maximizing the foil's material consumption and in bypassing the cavitation bubble. The second part is the polytetrafluorethylen (PTFE) coated magnetic stirrer system of two small magnets. The magnets are placed inside of the colloid and exhibit a continuous rotation (120 rpm) caused by the magnetic field of a stirrer plate placed under the sample. The flow of the colloid allows the incoming laser beam to irradiate the foil without a high particle concentration shielding effect. Two magnets are chosen due to their advantage to protect each other before attachment on the magnetic nickel foil.

After the irradiation process, the samples were centrifuged by different centrifuging protocols (Tab. 7.1) to find an optimal way for fast Pd-Ni NPs production. As it was found, only the first methodology, including 15 minutes centrifuging at 14500 rpm (Centrifuge MiniSpin plus, non-refrigerated, with Rotor F-45-12-11, 230 V/50 – 60 Hz) with 1.5 mL Eppendorf enabled the significant separation of material from the colloids. The other methodologies were able to separate none or only a negligible amount of NPs. Thus, the first methodology was chosen for the separation of NPs. After the centrifuging, the produced NPs were sedimented on the Eppendorf's bottom (Fig. 7.3), while the supernatant was mainly composed of the solvent, including the Pd salt. Hence, the supernatants were taken out from the Eppendorf and another colloid replaced a missing volume. The solutions in the Eppendorf were centrifuged until all NPs in the solvent were transformed into the sediment. Finally, the missing volume in the Eppendorf was replaced by demiH$_2$O, homogenized and once more centrifuged. The last step serves as a cleaning procedure from the residual Pd salt. Since only a small amount of water stayed in the Eppendorf, the colloid was dried by oven at 70 °C. Before each experiment or analysis of NPs, the dried sample was dissolved in the specific volume of demiH$_2$O and homogenized by an ultrasonic cleaner (SONOREX DIGITEC DT 510 H, 35 kHz, 9.7 L).

Method	Speed	Centrifuge time	Eppendorf's volume	Number of eppendorfs	Yield material
1	14500 rpm	0.25 hr	1.5 mL	12	significant
2	4500 rpm	2 hr	13 mL	33	negligible
3	4500 rpm	2 hr	40 mL	10	none

Table 7.1: List of used centrifuging methods to find the effective procedure to get Ni-based NPs

The design of the experiment with the laser was based on our previous study with Ti-Ag NPs [158] with some modifications. The RLAL parameters for the preparation of Pd-based NPs were given *ad hoc*. Thus, different concentrations of palladium salt solutions were chosen for the preparation of the nanoalloys. The concentrations of the K$_2$PdCl$_4$ were the following: 1 mM, 0.1 mM, 0.01 mM, and without salt. The large range of concentrations served to determine which salt concentration is the optimal one for the creation of the best nanocatalysts. In addition, a small range of concentrations, which would result in the control over the content of palladium in the single nanostructure, was searched.
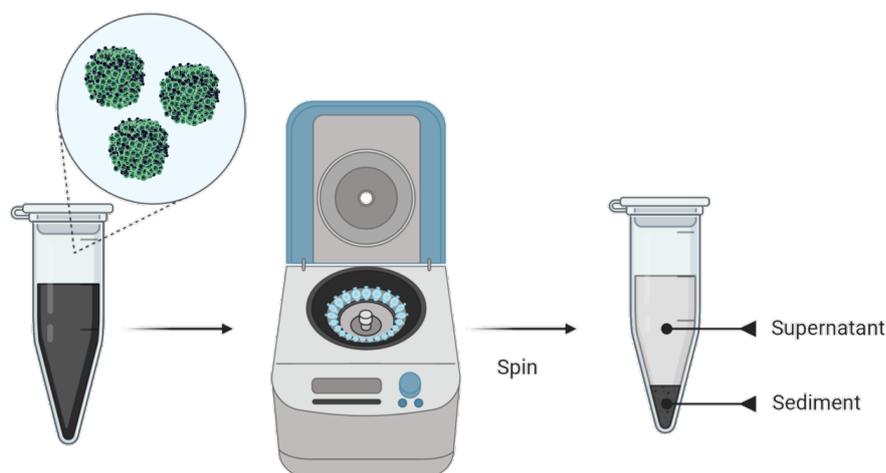
Figure 7.3: NPs separation by the centrifuging process, image created with help of BioRender.com

7.2 Catalytic activity procedure

The NPs' catalytic activity was evaluated by reducing 4-NP to 4-AP following the previous study [171]. For this, the optimal catalyst concentration was first assessed by a screening test (Fig. 7.4), where 24 μL of 5mM 4-NP (> 99% $C_6H_5NO_3$, crystals, Sigma-Aldrich), 120 μL of 0.1M sodium borohydride (> 96% $NaBH_4$, powder, Sigma-Aldrich), and various concentration of the NPs (100.0, 50.0, 25.0, 12.5, and 6.25 mg/L) were mixed in deionized water at a volume of 1 mL and transferred to quartz cuvettes, which served as the chemical reactor for the 4-NP reduction. The $NaBH_4$ was used in large amounts compared to 4-NP, and, thus, it can be considered constant during the reaction.

The decreasing concentration of 4-NP in the final liquid was step by step determined by the absorbance at 401 nm by a UV-Vis spectrometer (DR 3900, Hach Lange). The continuous absorption decrements at this wavelength denote the 4-NP reduction [172]. Note that 4-NP usually has the highest absorption peak at 317 nm, nevertheless by adding $NaBH_4$ (pH > 12) and thus by changing pH, the absorption peak shifts to 401 nm, due to its deprotonation and formation of 4-nitrophenolate [173].

Since the described reaction can be modeled as the pseudo-first-order reaction, the decreasing absorption values were transformed in $\ln(A/A_0)$ values, where A_0 is the starting absorption and A the absorption at a specific time. Further, the slope value in the graph of transformed absorption dependence on time represents the rate constant of reaction (k_{app}), which gives an idea of the material's catalytic power.

After the screening tests, the optimal concentration for all the samples was identified as 6.25 mg/L, which constitutes the minimally used concentration with a visible catalytic effect. In HPLC, the reactions using Pd-based samples followed the protocol with the same chemical ratios as those found for the screening tests.
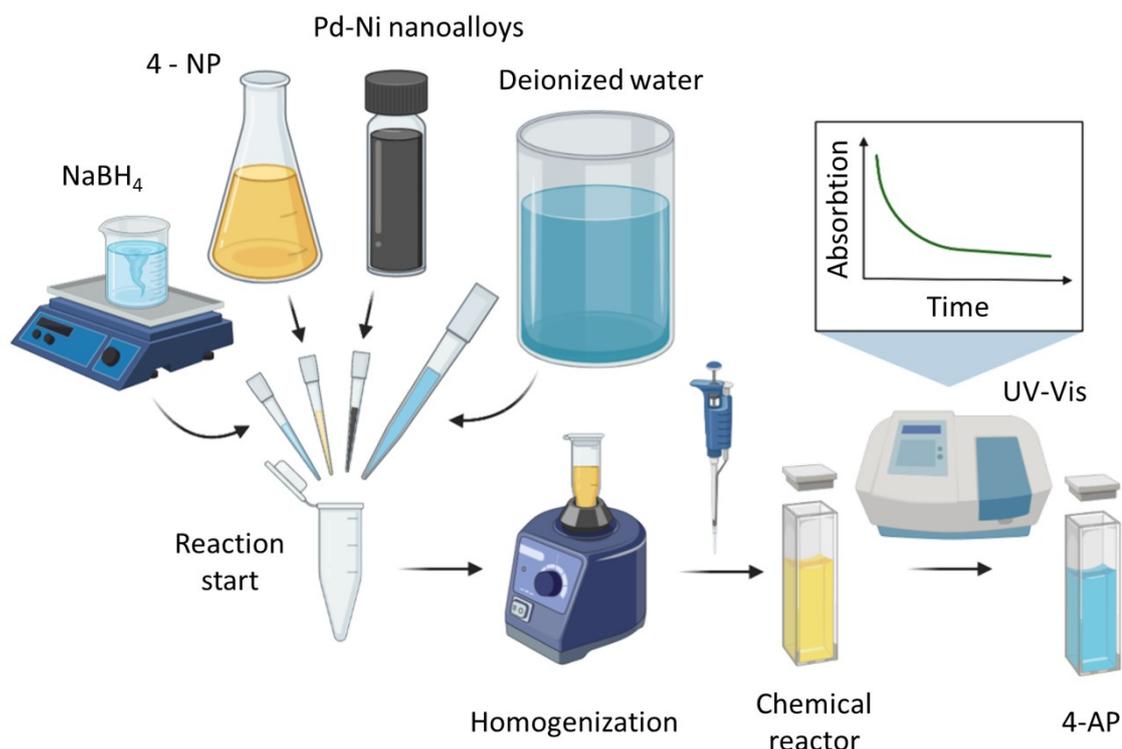
Figure 7.4: Screening routine for testing a catalyst on 4-NP degradation. Scheme was created with the help of BioRender.com

However, the reactions in bigger volumes and with magnetic stirring led to the complete degradation of 4-NP already in a minute. Thus, even a lower concentration was considered for Pd-based samples. Subsequently, the protocol was modified from the point of view of NPs concentration. The reaction mixtures were magnetically stirred in a volume of 20 mL at 150 rpm and ambient conditions (22 °C) for the entire experiment. The NPs were used with a lower concentration (3.125 mg/L) because the concentration represents half of the previous one and this concentration continues in the already tested continuous protocol (100, 50, 25, 12.5, 6.25, 3.125 mg/L, etc.).

Since the reaction started, aliquots (1.5 mL) were taken from the mixtures at different intervals and filtered using a magnet near the pipette tip and subsequently by syringe filters with a pore size of 220 nm (CHS Filterpure PTFE). The filtered samples were analyzed by HPLC using a chromatograph (UltiMate 3000, Thermo Fisher Scientific). The ultraviolet-visible (UV-Vis) detector (VWD-3100, Thermo Fisher Scientific) attached to the chromatograph was set to 230 nm and 323 nm to observe the simultaneous presence of 4-AP and 4-NP, respectively. Both compounds were separated in the instrument through a Kinetex EVO C18 column (Phenomenex, 150 mm length $\times$ 4.6 mm i.d., 2.7 μm particle size) at 40 °C. The mobile phase was composed of 20% acetonitrile ($>$ 98% MeCN, Penta) solution with a pH set to 3 by adding 0.5 mL H_3PO_4 ($>$ 85%, Penta) in a 1 L solution that consisted of

deionized water and MeCN. Before adding the acid, the solution was cleaned by filtration using a Lafil400 and NY (Nylon) membrane (pore size 220 nm, GVS Filter Technology UK Ltd.). After preparing the calibration samples for 4-NP in water and 4-AP in methanol, the instrument was prepared for the chromatography analysis, which started with the injection of the samples. The calibration curves enabled precise detection of 4-NP and 4-AP at the instrument's detection limit (6 μM). The injection volume in the instrument was 20 μl, and the flow rate 1.2 mL/min. According to pre-tests, the retention time of 4-AP was expected to be around 1.3 minutes and for 4-NP around 6.4 minutes.

Since the results about both organic compounds were determined, the 4-NP degradation efficiency (eq. 7.1), conversion (eq. 7.2), selectivity (eq. 7.3), turnover frequency (TOF)(eq. 7.4), and activity parameter (k_c) were calculated to check the performance of three employed Pd-based catalysts through the following set of formulas:

$$Degradation\ efficiency\,(\%) = \left(1 - \frac{final\ 4-NP\ concentration}{origin\ 4-NP\ concentration}\right) \cdot 100\,[\%]$$

(7.1)

$$Conversion\,(\%) = \left(\frac{final\ amount\ of\ 4-AP}{origin\ amount\ of\ 4-NP}\right) \cdot 100\,[\%] \qquad (7.2)$$

$$Selectivity\,(\%) = \left(\frac{conversion\ in\ specific\ time}{degradation\ efficiency\ in\ specific\ time}\right) \cdot 100\,[\%] \qquad (7.3)$$

$$TOF\,(h^{-1}) = \left(\frac{degraded\ moles\ of\ reactant\ 4-NP}{moles\ of\ catalyst\ Pd\ material \times time\ in\ hours}\right) \cdot 100\,[\%] \quad (7.4)$$

The degradation efficiency gives information about the effectivity of NPs to degrade 4-NP. The conversion represents the percentage of the original 4-NP, which is transformed into the final product (4-AP). Since not all the material must be degraded during the reaction, the selectivity must also be defined. The value of selectivity describes how much percent of degraded 4-NP is transformed into 4-AP. In other words, the reaction can also have other products.

Further, the TOF represents the catalyst's performance in the context of its amount and time needed for the degradation. Finally, the activity parameter represented by the change of kinetic rate constant determines the total efficiency of the catalyst. Its value is represented by the slope of the linear regression line between k_{app} and the concentration of catalyst, as it is reported elsewhere [174, 175].

7.3 Preparation of partly-reduced graphene oxide nanosupport and Pd-Ni/graphene-based catalyst

The graphene-based material constituting a nanosupport for Pd-Ni NPs was synthesized from graphene oxide (GO) colloid (2 mg/mL, Sigma Aldrich) by a described method [176, 177]. Briefly, a colloidal GO suspension was exposed to sonication for 3 h using the ultrasonic cleaner (SONOREX DIGITEC DT 510 H, 35 kHz, 9.7 L). Subsequently, $0.33 \mu l$/GO mg hydrazine monohydrate (50-60%, Aldrich) as a reducing agent was added to the suspension. The reactants were added in an oil bath held at 80 °C for 12 h at constant stirring with a teflon coated magnet. Then, the final solution resulted in a black partly-reduced graphene oxide powder (prGO), which precipitated.

In the second step, the preparation of Pd-Ni/graphene-based catalyst partly followed the method used to prepare Pd/rGO. The method was previously used for the reduction of metal salt together with rGO [177]. Firstly, the prepared prGO was added in demiH$_2$O to form a sample with 0.6 mg/mL concentration. The ultrasonication followed for 90 minutes, which resulted in a properly dispersed solution. Secondly, each sample with NPs was dispersed in demiH$_2$O at a concentration of 0.06 mg/mL by mixing and ultrasonication for 1 h. The samples were mixed with the same graphene-based solution (0.6 mg/mL) in a vial with a 1:1 ratio (particles solution : graphene-based solution). Finally, the samples were agitated for 30 minutes by a magnetic stirrer and dried at 80 °C.

8 Results and discussion

In the current diploma thesis, the laser ablation and reactive laser ablation strategies were used to prepare Ni-based NPs with a manageable chemical composition in the context of palladium to nickel ratio. Various Pd salt concentrations achieved this aim during LAL and RLAL experiments (Tab. 8.1). Further, the samples were subjected to various characterization techniques and catalysis tests to find the features of the generated NPs, a deeper understanding of the process behind their formation, and find the ideal material for heterogeneous catalysis. Finally, the catalytic activity of nanocatalysts was enhanced by the decoration of graphene-based nanosupports with Pd-Ni NPs.

Sample	Foil	Salt	Liquid medium
S1	Ni foil	-	40 mL dH_2O
S2	Ni foil	0.01 mM K_2PdCl_4	40 mL dH_2O
S3	Ni foil	0.1 mM K_2PdCl_4	40 mL dH_2O
S4	Ni foil	1 mM K_2PdCl_4	40 mL dH_2O

Table 8.1: List of material parameters used for the laser-mediated generation of Ni-based samples

Before starting with the experiments, including the palladium salt, the laser ablation of the nickel foil was performed with various repetition rates of the femtosecond laser. The repetition rates have been set to 0.2 MHz, 0.4 MHz, 0.6 MHz, 0.8 MHz, and 1.0 MHz. To check the influence of rates, the UV-Vis spectrophotometer with a maximum wavelength range from 320 to 1100 nm and a minimum wavelength step of 1 nm measured the absorbance of the samples.

The UV-Vis (Fig. 8.1) graphs of the prepared colloids exhibit a proportion between the increasing repetition rate and the higher samples' absorbance. The observation can be connected with the relationship between the number of pulses and the amount of produced material, which is directly proportional to the samples' absorbance.

A significant decrease of absorption occurs in the sample, which was prepared by setting the laser to the repetition rate of 1 MHz. The decrease in absorption also means a decrease in the concentration of the sample and, thus, lower production of the NPs. As a consequence, another two repetition rates were used - 0.7 MHz and 0.9 MHz. All UV-Vis data led to the finding that the optimal repetition rate for the samples is 0.9 MHz. Since the increase of repetition rate is connected with a slight decrease of energy per pulse, the 1.0 MHz repetition rate led most probably
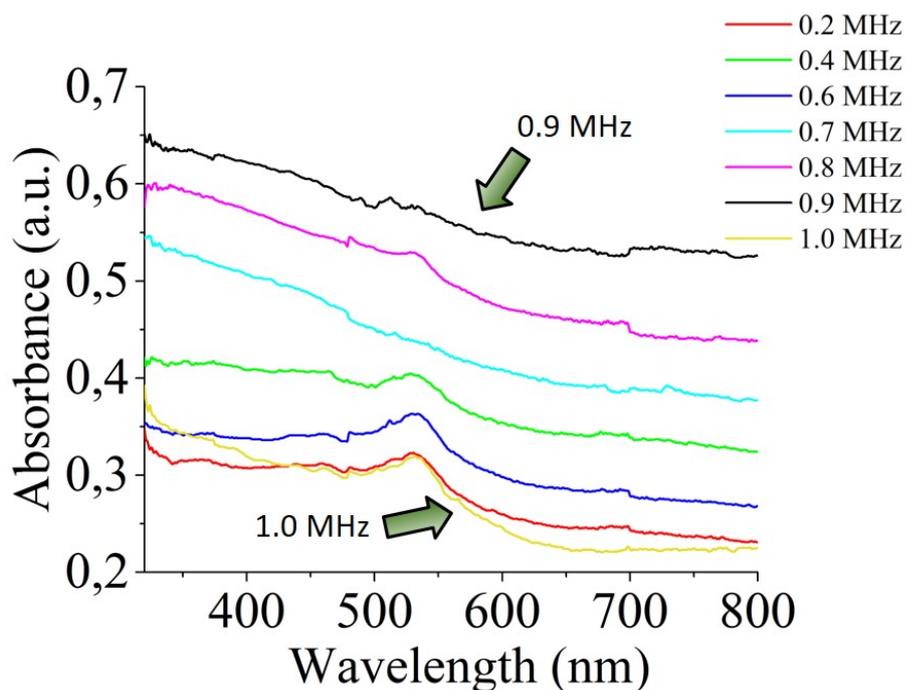
Figure 8.1: UV–Vis spectra in a wavelength range from 320 to 800 nm of Ni NPs prepared by LAL with different repetition rates of the pulsed fs laser. The arrows in the graph highlight the threshold repetition rate at 900 kHz.

to energies below the ablation threshold. Then, the production of particles was naturally suppressed. The alternative interpretation can be hidden in the cavitation bubble shielding as the problem of high repetition lasers. Since the velocity of the scanning head was 2m/s, the distance between two pulses during 1.0 MHz irradiation was 2 μm. In contrast, the diameter of cavitation bubbles near the irradiation point is on the millimeter scale for ns lasers and on the fractions of a millimeter for the ps lasers or fs lasers [4]. Moreover, the time delay between two pulses was around 1 μs, and the cavitation bubble lifetime is tens or even a few hundreds of microseconds [178]. However, the cavitation bubble lifetime and its size can be decreased by lower pulse energies [4]. Since the 1.0 MHz sample does not exhibit similar absorbance as the 0.9 MHz sample, the production decrease coming from the attenuation of the laser beam by a concentrated solution can be rejected.

8.1   Pd-Ni NPs

8.1.1   UV-Vis

As a first step, the optimal repetition rate for Ni foil irradiation had been found, and thus, the experiments with palladium salt followed. Before starting the experiments with the salt, the palladium salt in dH_2O was mixed properly before each experiment by a MIX ARGOlab Vortex Mixer. Firstly, the irradiation time (15

minutes) was given based on a previous study [158]. Nevertheless, the UV-Vis spectroscopy with the already used parameters was used to compare the sample with the ones prepared by 12 minutes and 18 minutes of irradiation. The sample with shorter irradiation time exhibited significantly lower absorption, and the one with longer irradiation time had visibly higher absorption, which led to the statement that a saturated colloid was not prepared after 15 minutes of irradiation. Thus, the irradiation protocol could be followed. The measured graphs are included in the summarizing graph (Fig. 8.2).

In the same graph, it is possible to see the difference between S1 (Ni), S2 (0.01 mM), S3 (0.1 mM), and S4 (1 mM) samples. The increasing concentration of salt resulted in a higher absorbance. In S1, S2, S3, the flat part of the curve matches Ni particles below 50 nm. The S2 and S3 samples exhibit a similar curve as the S1 sample, and unlike S4, the peak of unconverted Pd salt is not visible. Besides, a broad peak between 530 - 535 nm is visible for all samples and can mean an agglomeration of Ni NPs in S1 or Ni-based NPs in S2, S3, and S4 samples. Especially, the Pd-based samples exhibit this peak significantly, which can be connected with the possible lower stability of Pd-based NPs.

The S4 sample exhibits a valley and small peak at 359 nm and 417 nm, respectively. The same local extrema was found in the solution with Pd salt before irradiation. To be able to test the possible Pd salt contamination in the S4 sample, the UV-Vis spectra of 1mM Pd salt and 1mM Pd salt with Ni NPs were measured. The comparison of S4 with the colloid, including Ni NPs and 1mM of Pd salt, indicates a significant conversion of Pd salt. However, the residual salt in the S4 sample can still be expected because of the similar position of the extrema. Nevertheless, the research was not influenced by the possible salt contamination because it was removed together with the supernatant after the centrifugation. In summary, the predictions about NPs, which are described based on the UV-Vis spectra, correspond to the Mie-theory calculations [165].

In addition, the samples exhibit increasing productivity with an increasing amount of used Pd salt. The concentrations of samples were first determined based on the UV-Vis spectra. Nevertheless, the concentration of samples could be influenced not only by a higher amount of the produced material but also by the decrease of the colloid volume. This situation is extremely usual when the colloids are evaporated during the irradiation of a foil immersed in a solvent. Significantly, the used water can absorb much energy from the infra-red laser used for the irradiation. To follow this problem, the nickel foil was placed near the water surface (3 mm), and the liquid volume was checked in all samples after the irradiation many times. The final volume was on average 39.3, and the maximum deviation was $\pm$ 0.3 mL; thus, the concentrations of samples were only negligibly affected by the solvent evaporation.

8.1.2 TEM

In our study, the S/TEM TITAN 80–300, FEI instrument used for the analysis enabled us to focus electrons at an acceleration voltage of 100kV to display the sample. The emitted electrons were generated by a bright LaB_6 hot cathode. Then
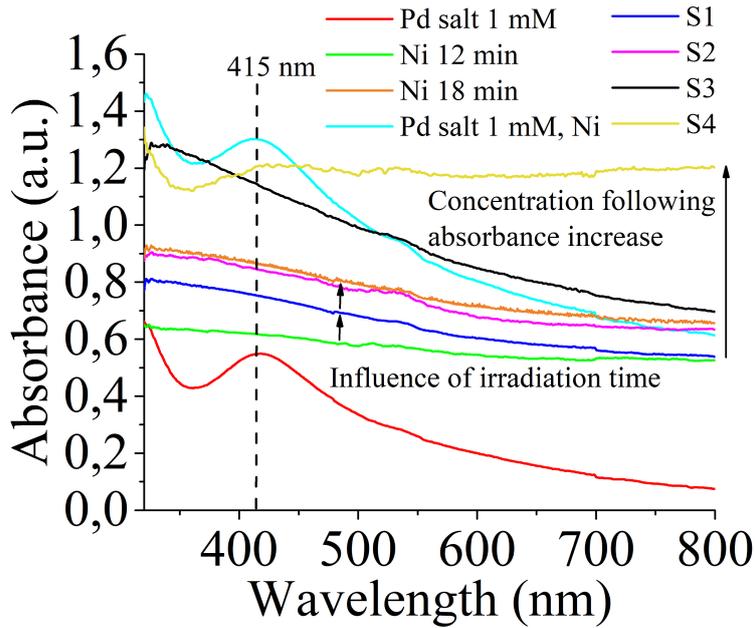
Figure 8.2: UV–Vis spectra in a wavelength range from 320 to 800 nm of different samples prepared by LAL or RLAL techniques. Moreover, the graph includes UV-Vis spectra of the samples including the Pd salt at 1mM concentration. The arrows highlight the influence of irradiation time and Pd salt concentration over the UV-Vis response. The lines between 413 and 423 nm highlight the peak for Pd salt.

the analyzed data from the instrument (Fig. 8.3) includes representative TEM pictures of all the samples with a scale bar of 100 nm. In the graphs, approximately spherical NPs are visible. To find the real size of NPs, 500 particles for each sample were measured by the software ImageJ and the corresponding size histograms were created. Long-normal functions fitted the distributions of particles with the general formula 8.1:

$$y(x) = \frac{1}{x\sigma\sqrt{2\pi}} e^{-\frac{(\ln x - \mu)^2}{2\sigma^2}} \qquad (8.1)$$

where μ is the mean value and σ is the standard deviation.

In the case of S1, it is possible to observe NPs with a mean size of 33.7 nm $\pm$ 1.8 nm, which is in agreement with the UV-Vis predictions. All NPs on carbon film should be the nickel ones because the colloid was prepared by the ablation of the nickel foil. For S2, the histogram of NPs is a little bit shifted to the bigger sizes of 38.8 ± 1.7 nm. The shift can be connected with the alloying with the palladium resulting in the NPs size expansion. Nevertheless, no significant difference in the mean size can also be caused by measurement deviation or deviation in settings of laser experiment. For instance, the position of focus influence significantly the synthesis.

Besides observations in the two mentioned samples, a new peak between 6.8 - 6.9 nm appears in the histograms of S3 and S4. More precisely, these small NPs

Sample	TEM	
	Images	Histograms
S1		
S2		
S3		
S4		
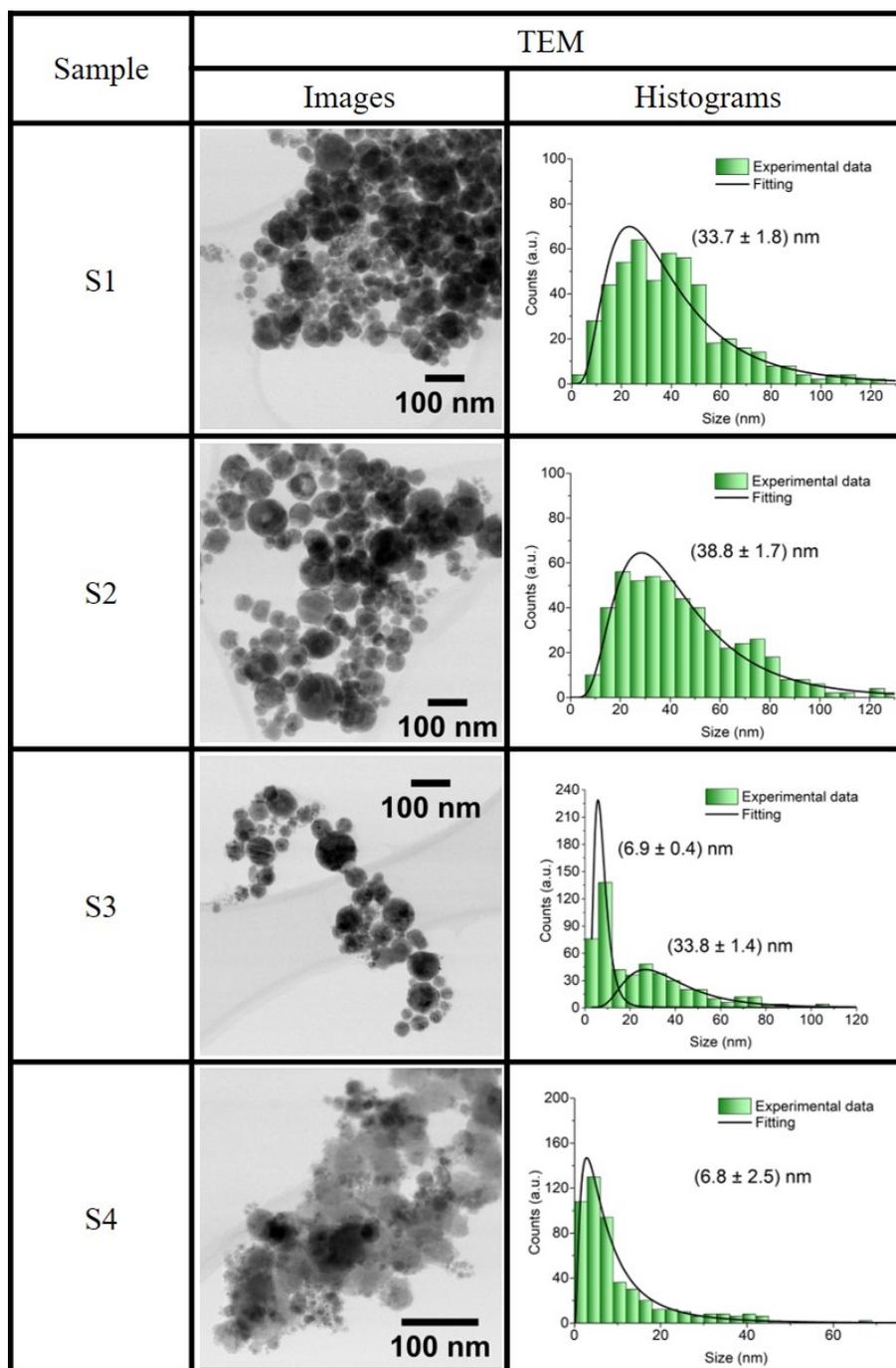
Figure 8.3: Representative TEM pictures and size histograms of all samples. Each histogram includes the counting of 500 particles. The size distributions are fitted by the log-normal functions. The means and standard deviations calculated from fitting are included inset the histograms.

were also visible in S2 sample. However, their amount is almost negligible. These NPs surround the surfaces of the big NPs, and thus, they look to be attached to the big ones. In the case of S3, the histogram displays two distributions, at 6.9 $\pm$

0.4 and at 33.8 $\pm$ 1.4 nm. Since the difference between S1 and S2 samples is the concentration of Pd salt used during RLAL, the creation of NPs can be connected with it, and their composition is probably Pd-based.

In the case of S4, the number of small NPs 6.8 $\pm$ 2.5 is predominant. The bigger particles inhabit the sample, but the large amount of small NPs suppresses their concentration. Since the small NPs are possibly composed of palladium and the amount of Pd-salt was the highest in S4 sample, the predominant presence of these particles corresponds well to the assumptions.

8.1.3 EDX

The TEM measurements confirm the creation of spherical NPs with two different distributions. Besides, the EDX figure (Fig. 8.4) helps to understand more the chemical composition of particles. In our study, the chemical analysis was made by scanning EDX selected area using a detector X-Max 80 (Oxford Instruments) incorporated into the TEM instrument.

In general, the EDX analysis was made in dark field mode, which permits to distinguish the NPs with a possible different composition hidden in the brightness of the NPs. In each sample, two types of NPs (areas) were chosen for analysis - the brighter ones and the darker ones. In S1, it is possible to observe a significant intensity of the Ni signal and smaller O and Cu signals. The appearance of the Cu signal comes in all the samples from the samples' holder, which is composed of a Cu grid. Besides, the oxygen comes directly from the NPs, and thus, it is probable that the NPs are composed of nickel oxide in both areas (NiO_x). Alternatively, the oxygen can come from adsorbed air oxygen while the sample was analyzed. The small oxygen peak more probably indicates the oxygen absorption. Moreover, a small amount of the NPs looks like core-shell structures, where the shell is brighter. The thickness of brighter shells is on average 2.22 $\pm$ 0.30 nm and can be composed of the NiO_y.

In S2, the peaks, which were not described before, belong to palladium and carbon. The intensity of palladium peaks is extremely low in both areas, and thus, a more precise technique is required for a better analysis of the samples. Nevertheless, the concentrations of palladium look similar in both areas. The particles exhibit a similar composition, which can be associated with the creation of Pd-Ni nanoalloys or another type of Pd-based NPs. In addition, the carbon peaks indicate the detection of the carbon film, which was located under the NPs on the Cu grid. The lack of carbon peak in the S1 sample can be caused by the overlapping of oxygen and carbon peaks.

In S3, the palladium peaks are located at the same positions with slightly higher intensities than those found in the S2 sample. Together with the previous sample, the O peak is suppressed in comparison with the nickel one. This can be caused by the presence of Pd-based NPs, which overlaps the oxygen peak. Alternatively, the presence of Pd can lead to the replacement of oxygen from Ni NPs by Pd and thus to the creation of mixed Pd-Ni nanoalloys.

The S4 is the first sample with a high signal from palladium, which is compa-
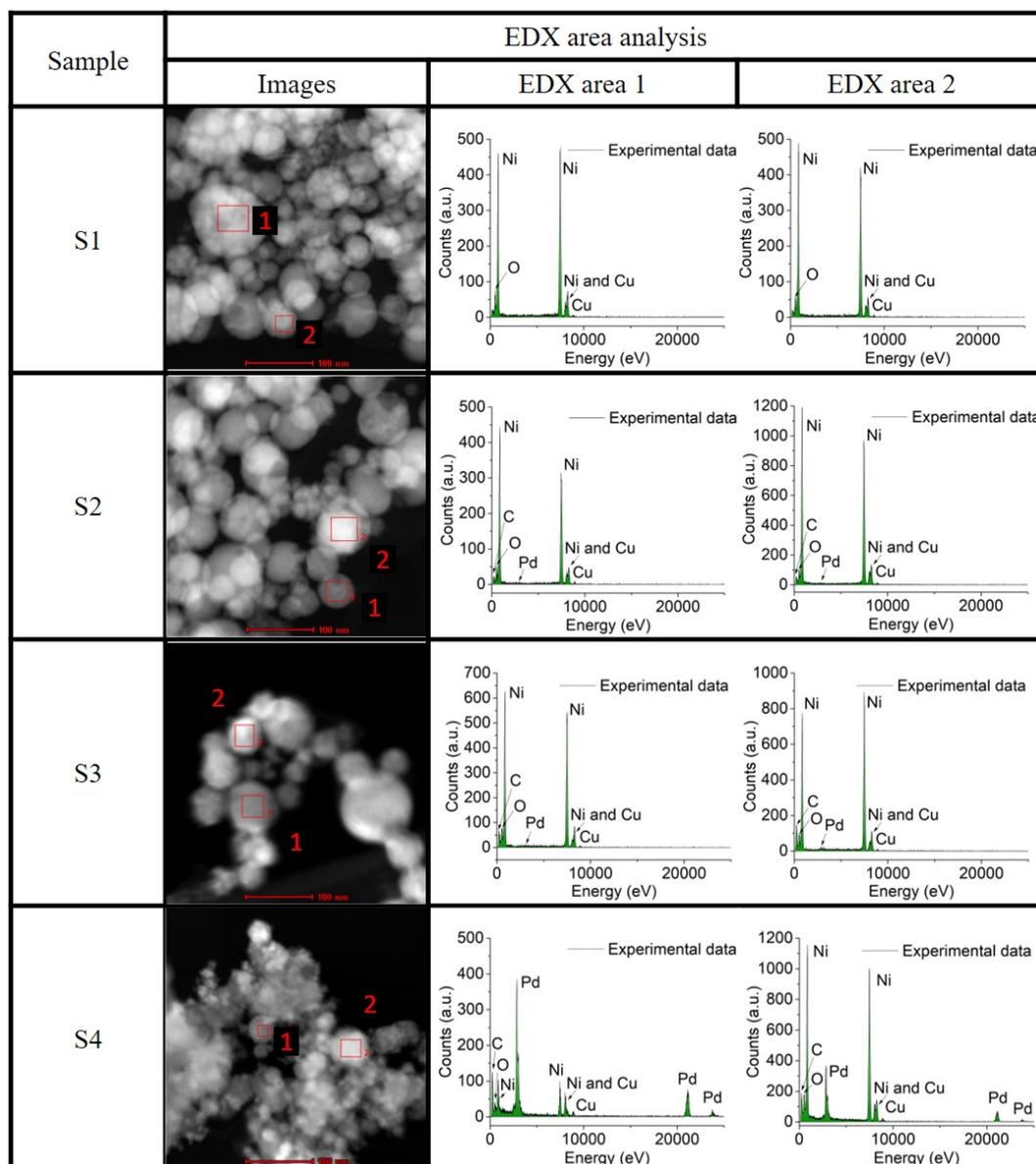
Figure 8.4: Representative figures of EDX area analysis of all samples. The right TEM pictures show where the analysis was taken. Each sample includes 2 selected areas with brighter and darker NPs. The middle and left pictures represent the corresponding EDX spectra

rable with the nickel one. In addition, the two chosen areas exhibit a significant difference in Pd:Ni signal ratio. The first area represented by darker and smaller NPs exhibits the predominant presence of palladium. Oppositely, the second area includes a brighter and bigger particle, which has a predominant amount of nickel. Consequently, both types of particles are composed of Pd-Ni nanoalloys with different Pd:Ni ratios, or the smaller NPs constitute the palladium NPs. In any case, the area with smaller NPs contains the particles with the highest relative content of palladium.

8.1.4 SAED

Although EDX analysis gives us more information about the chemical composition of the NPs, there is still a lack of information about the crystallographic structure of the NPs. A deeper understanding of NPs structures was given by SAED and TEM, which complements the crystallographic composition data from the electron diffraction.

In SAED, a high-angle annular dark-field detector (HAADF) was used for getting SADP. The patterns (Fig. 8.5) were measured by the software ImageJ to get the 1/2r values, which were recalculated from the distances between atoms. The distances were connected with the Miller index of Pd- or Ni-based crystals thanks to the International Centre for Diffraction Data (ICDD) files. All values are included in Tab. 8.2. In general, the diffractograms display the ring SADP, and thus polycrystals should be expected. The found crystal families match with ICDD file: 65-5788 for $Pd_{0.475}Ni_{0.525}$, ICDD file: 45-1027 or 65-380 for Ni, ICDD file: 65-5745 for NiO, ICDD file: 65-2867 or 72-710 for Pd, ICDD file: 65-5065 for Pd_2O.
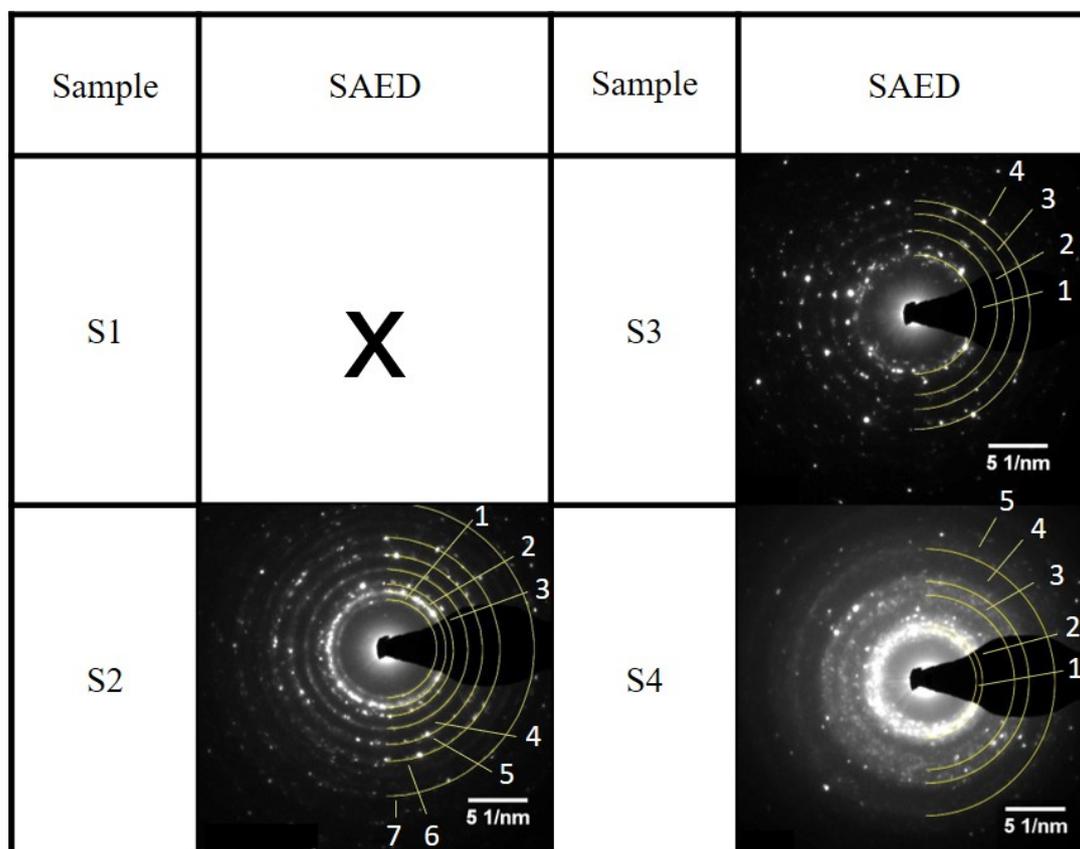
Figure 8.5: Representative SAED images of all the samples and semicircles marking the diffraction patterns. The measured d-spacings are assigned to the crystallographic families and Miller indices.

The SAED of S1 was not made because the sample can only display Ni-based crystals. In the case of the S2 sample, the d-spacings are mostly paired with Ni or

NiO. However, the 2.419 Å , 1.797 Å and 0.806 Å d-spacings belong only to Ni. Since the EDX analysis shows the presence of oxygen in S2, the sample consists of Ni and NiO NPs combination or Ni-core NPs with a NiO shell, which has also been found in other studies [179, 180]. The process of NPs oxidation is based on the interaction of the surrounding environment, for instance, demiH$_2$O, with the surface of the metal particle. Some of the d-spacings can belong to Pd-based NPs. Nevertheless, the low presence of Pd-based material, as was indicated by EDX, does not enable us to observe the d-spacings, which Pd-based crystals could pair.

In the S3 sample, it is possible to detect NiO crystals with hkl (220), while the other d-spacings can belong to Pd NPs. Besides, the sample S4 exhibits not only Ni/NiO NPs with possible Pd NPs, but also the Pd-Ni nanoalloys. The lack of d-spacings for Pd-Ni nanoalloys in the previous samples can be caused by comparing the results with datasheet of Pd-Ni NPs with the Pd:Ni ratio 1:1. However, the Pd:Ni ratio significantly influences the crystal dimensions. The Pd-Ni$_x$ structure usually exhibits the d-spacings between values, typical for one material (Ni) or another (Pd). Since the percentage of alloyed palladium in Ni particles can be too low, the d-spacings can be almost identical for Ni or Pd-Ni$_x$ crystals. The small Pd content in the Ni NPs or Ni in the Pd ones is not detectable by the method. Anyway, nickel or nickel oxide NPs are present in all samples.

The SAED analysis brings more information about the structure of NPs created by RLAL. Nevertheless, another diffraction investigation was made to support the SAED results.

8.1.5 TEM diffraction

Additional crystallographic details (Fig. 8.6) were obtained from the high-resolution TEM analysis of the NPs. The high resolution in the TEM instrument enabled the direct observation of crystallographic families in the particles. Since it was possible to precisely localize the d-spacings, the analysis of big NPs and small ones surrounding the big NPs was made. The distances were collected by the measurements of individual NPs in ImageJ.

As it can be predicted from the EDX and SAED, the S1 sample includes d-spacings of NiO or Ni. The presence of NiO crystal with (111) Miller index at the surface of Ni-based particles indicates the creation of NiO shells around the particles. Moreover, several particles in TEM pictures exhibit two types of contrast, darker core and brighter shell, which can be connected with creating an oxidized shell around some Ni NPs. The thickness of the brighter shells is, on average, 2.22 $\pm$ 0.30 nm.

The TEM analysis of sample S2 shows the small NPs in area 2, which are composed of Pd, while the big NPs are similar to the ones of sample S1. The NiO crystal in the particle's core in the second image can be connected with the attachment of another particle on the surface of the big one. Since the Pd$_2$O d-spacing could not be found in the S2 sample, the d-spacing at 1.492 Å from the SAED analysis can only be associate with NiO.

Aside from the sample S2, the S3 sample exhibits a possible presence of Pd-Ni

S2 (0.01 mM Pd salt)			
No	1/2r (nm^{-1})	d-spacing (A)	hkl
1	8.277	2.416	(111) NiO
2	9.742	2.053	(011) Ni / (200) NiO
3	11.132	1.797	(200) Ni
4	13.405	1.492	(220) NiO or Pd$_2$O
5	15.962	1.253	(220) Ni / (311) NiO
6	18.876	1.060	(311) Ni / (222) Pd-Ni
7	24.801	0.806	(331) Ni
S3 (0.1 mM Pd salt)			
No	1/2r (nm^{-1})	d-spacing (A)	hkl
1	10.093	1.982	(200) Pd / (011) Ni
2	13.872	1.442	(220) NiO
3	16.581	1.206	(311) Pd / (220) Ni / (222) NiO
4	19.380	1.032	(311) Ni / (400) NiO
S4 (1 mM Pd salt)			
No	1/2r (nm^{-1})	d-spacing (A)	hkl
1	8.651	2.312	(010) Ni
2	9.652	2.072	(011) Ni / (200) NiO
3	14.828	1.349	(220) Pd or Pd-Ni
4	17.306	1.156	(311) Pd / (400) Pd-Ni
5	22.738	0.880	(331) Pd or Pd-Ni / (420) Pd

Table 8.2: Collected SAED parameters of samples corresponding to the specific crystallographic families in Ni- or Pd-based NPs.

nanoalloys. The alloyed material can possibly be located in the core of the big particle in image 1. Moreover, the small NPs with crystallographic families are not visible in the pictures, while these NPs were previously associated with the Pd NPs. Nevertheless, the combination with SAED data for S3 leads to the theory that the small NPs are also in this sample composed of palladium.

Finally, the sample S4 includes a large amount of small palladium NPs, which are surrounding the big NPs that are probably made of NiO$_z$. The presence of Pd-Ni nanoalloys is also probable in this sample. Nevertheless, it is not possible to confirm the creation of randomly mixed Pd-Ni nanoalloys. The d-spacings below 2 Å were not observed, and thus the most of the d-spacings that belong to Pd-Ni, and Pd can be hidden.

In summary, the small NPs with a mean size around 7 nm are mainly composed of Pd, and the big NPs with a mean size of 33.8 or 38.8 nm are composed of Ni. The separation of the material can be connected with the creation Pd-NiO$_z$ NPs instead of Pd-Ni mixed nanoalloys. The samples can form NPs connected by metal-support

Sample	HRTEM crystallographic analysis	
	Images 1	Images 2
S1		X
S2		
S3		
S4		X

S1

No	d-spacing	hkl
1	2.399 ± 0.025	(111) NiO
2	2.064 ± 0.053	(011) Ni / (200) NiO
3	-	-
4	-	-

S2

No	d-spacing	hkl
1	2.395 ± 0.051	(010) NiO
2	2.244 ± 0.021	(111) Pd
3	2.108 ± 0.029	(200) NiO / (111) PdNi
4	2.056 ± 0.022	(011) Ni / (200) NiO

S3

No	d-spacing	hkl
1	2.410 ± 0.027	(010) NiO
2	2.129 ± 0.030	(200) NiO / (111) PdNi
3	2.068 ± 0.034	(011) Ni / (200) NiO
4	-	-

S4

No	d-spacing	hkl
1	$2,266 \pm 0.024$	(111) Pd
2	$2,125 \pm 0.034$	(200) NiO / (111) PdNi
3	2.093 ± 0.026	(200) NiO
4	-	-

Figure 8.6: Representative TEM figures highlighting the selected area used for the crystallographic analysis. The corresponding d-spacings of the marked areas are assigned to the crystallographic families and Miller indices.

interactions (MSI) as it was reported before for e.g. Pd/TiO NPs [181], Au/TiO$_2$, Au/ZrO$_2$, Au/ZnO, and Au/Al$_2$O$_3$ [182], and Cu$_x$Ni$_{1-x}$/CeO$_2$ [183]. In our case, the support can be represented by NiO$_z$ NPs, while the small Pd NPs act as the metal that surrounds the nanosupport (Fig. 8.7); thus, the charge transfer between them occurs. Moreover, the NPs are surrounded by some "gel-looking" structure, which has already been attributed to the support skin, which surrounds the smaller NPs [181].

The Pd-NiO$_z$ NPs with Pd at their surface represents a possible great nanocatalyst, and its potential theoretical features overcome the ones of Pd-Ni mixed nanoalloy. Specifically, the Pd NPs on the surface should be responsible for catalytic
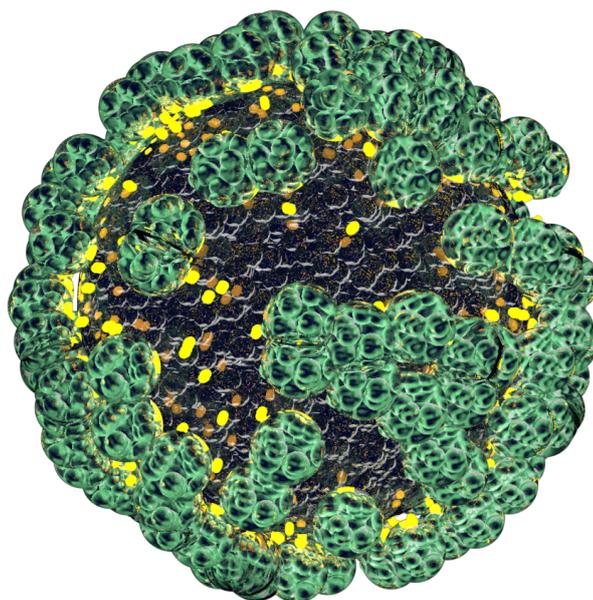
Figure 8.7: Scheme of Pd NPs surrounding nickel-based spherical nanosupport. The metal-support interactions between the NPs attributed to charge transfer between the elements

activity, and the NiO_z support should enable the magnetic movement of NPs. In general, the discussed MSI interaction, which represents a connection between the NPs based on the electron transfer between them, plays a crucial role in catalysis [183]. Specifically, the activity of transition-metal NPs can be enhanced by promoting the effectiveness of the metal oxide support, which comes just from the charge transfer between the catalyst and support. Moreover, the interaction between the metal and support can affect the selectivity of the catalytic reaction. In some cases, the reaction is accelerated by oxygen vacancies in the support structure [181]. Since our NiO_z exhibit a relatively low amount of oxygen, the possible vacancies can also be presented in the structure, especially when the NPs are coming from non-equilibrium reactions like the laser ablation is [184].

8.1.6 spICP-MS

The composition of big NPs and small NPs seems to be associated with the NiO_z NPs and Pd NPs, respectively. As the understanding of their ratio in the nanostructures is crucial for using the material in various applications, the spICP-MS was made. Only metals were monitored during the measurements since the oxygen can not be measured by mass or optical spectrometry. The analysis gives precise information about the ratio between Pd:Ni, among others. Moreover, the particles below 20 nm are not detectable in single-particle mode analysis, and therefore, only the big NPs

or big NPs with attached small NPs could be analyzed by the detector, which means that individual small Pd NPs should not be detected.

In our study, the mass spectrometer NexION 3000D (Perkin Elmer) with a detection limit of 0.5 ng/L, dwell time of 50 ms, and scanning time 50 s was used for the mentioned analysis of single particles. The calibration curves consisted of 4 samples for each metal element with concentrations from 12.5 μg/L to 100 μg/L. The data from the mass spectrometer are summarized in Tab. 8.3. To get the analysis from a single particle, the samples were diluted to the level below μg/L as reported elsewhere [185].

Sample S1 was used to check the method's effectiveness because the predictable 100% content of Ni in the sample was confirmed. On the other hand, the sample S2 includes 8.35 wt% of Pd and a predominant amount of nickel. In addition, the methodology was used to control the affiliation of NPs. The material detected as the Pd-based NPs exhibited a significantly smaller size distribution than the material connected with the Ni-based NPs, which is consistent with the TEM and EDX analyses.

The last two samples exhibit the highest Pd:Ni ratio, which is almost the same for both. As it is expected, the samples overcome the Pd content measured in the sample S2. However, the trend with an increasing amount of Pd is not confirmed in sample S4. The observation can be associated with the saturation of palladium NPs, which can surround the NiO_z support. A specific amount of Pd NPs can probably surround the surface of NiO_z NPs, and the remaining Pd NPs exist separately from the Pd-NiO_z NPs or without enough attachment to the possible catalyst. This assumption can be applied in the S4 sample and possibly with minor significance in the sample S3.

Alternatively, Pd-Ni mixed nanoalloys were formed in S3 and S4 samples with the same Pd:Ni ration. Nevertheless, the spICP-MS shows an almost 1:1 ratio of Pd and Ni atoms.

Sample	Ni amount (wt%)	Pd amount (wt%)
S1	100	0
S2	91.65	8.35
S3	47.22	52.78
S4	49.14	50.86

Table 8.3: Representative weight percentages of Ni and Pd determined in all samples by spICP-MS

8.1.7 Catalytic tests

The catalytic tests were performed by analyzing the samples' capability to degrade 4-NP using $NaBH_4$ and NPs. The already used UV-Vis spectrophotometer measured the 4-NP concentrations in the samples. The UV-Vis absorption value at 401 nm over time indicated the decrease of 4-NP in a chemical reactor. The monitoring

ended after 10 minutes of screening or after the reaction stopped due to the full transformation of 4-NP or the catalyst's deactivation.

The complete reaction scheme of 4-NP transformation to 4-AP is presented in Fig. 8.8. Here, the hydrogenation reaction mediated by the nanoparticle is presented. The $NaBH_4$ acts as the donor of hydrogen atoms to the NPs surface. The hydrogens are absorbed thanks to the physisorption between the charged particle surface and the dissolved atoms themselves. Since a 4-nitrophenolate is also adsorbed to the NPs surface, the catalytic degradation begins thanks to the transfer of electrons from $NaBH_4$ ions to 4-nitrophenolate ions. The used nanocatalyst enables a 6-electron powered reaction where the nitro group from 4-nitrophenolate is reduced to a nitroso group. The reaction continues by the reduction to a hydroxylamine group. Finally, the reactants are transformed to 4-AP, which represents the targeted product [73].
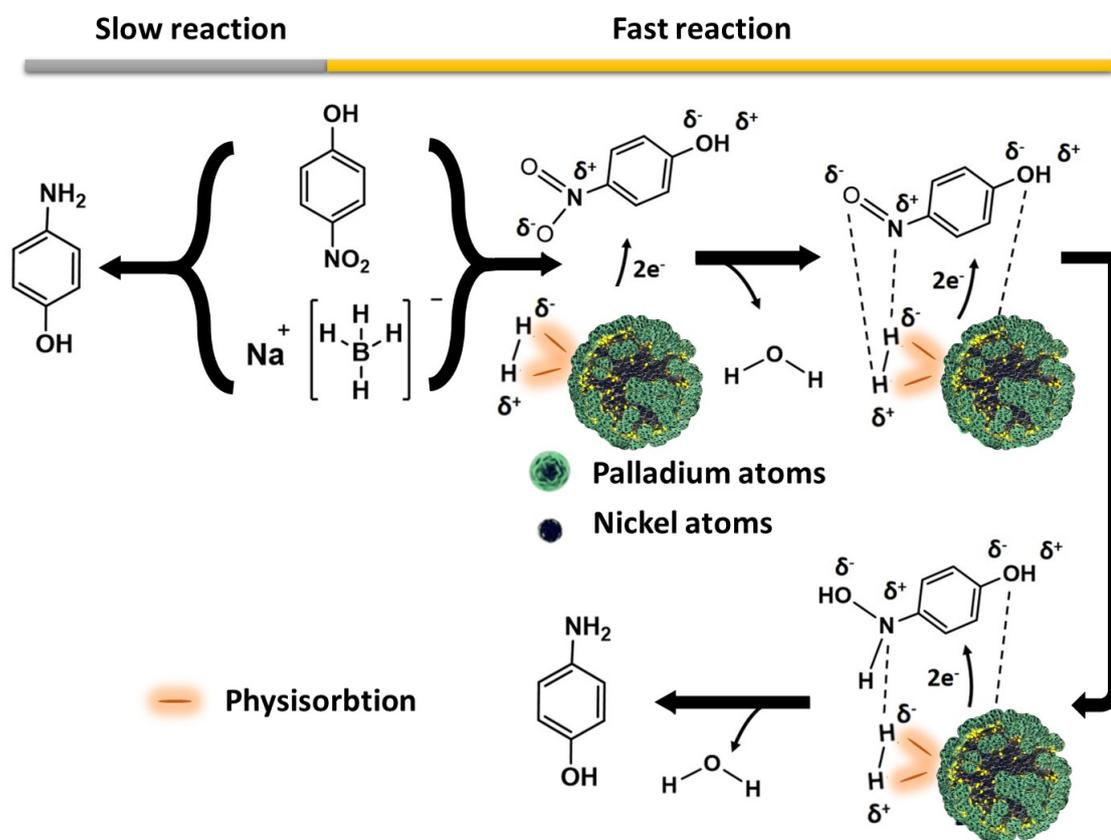
Figure 8.8: Reaction scheme of 4-NP transformation to 4-AP using metal-support NPs as the catalyst.

The described reaction can be modeled as a pseudo-first-order reaction. Following this prediction, the measured absorption values were fitted by the linear curves in the graphs with logarithmic scale $\ln(A/A_0)$, where A_0 is the starting absorption and A the absorption at a specific time. The calculated rate constants of the reactions are summarized in the (A) graph of Fig. 8.9.

In general, the reactions took place visibly in all samples instead of S1 samples.
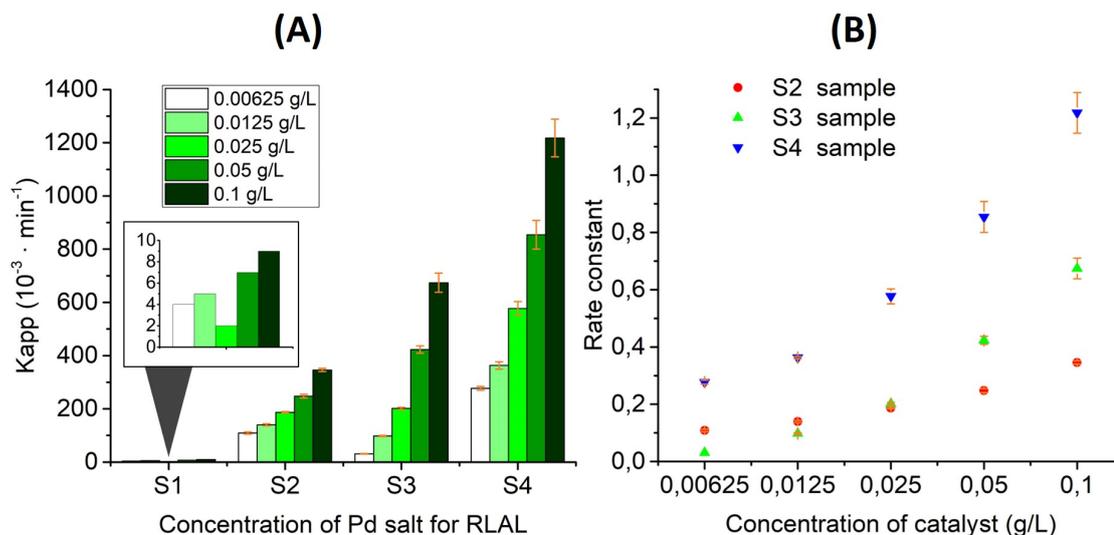
Figure 8.9: Representative rate constants (k_{app}) of 4-NP degradations catalyzed by NPs with different concentrations in the chemical reactors. The rate constants were calculated based on the assumption of the pseudo–first–order reaction.

The absorption in S1 samples was slowly decreasing or even equal during 10 minutes of the screening. The nickel particles caused the low degradation without palladium neighbors. The NiO$_z$ NPs have negligible catalytic activity in comparison with palladium NPs. Besides, the presence of Pd NPs leads in other samples to a significant increase in their catalytic activity.

The second batch of samples exhibits a high rate constant (0.109 min^{-1}) even for the low concentration of 6.25 mg/L. In addition, the rates are gradually increasing with the increasing amount of used NPs. It happens due to the increased total surface area of catalysts and thus the increased number of active sites available for catalytic hydrogenation. Nevertheless, the differences are lower than in S3 and S4 samples.

The S3 samples show a different rate constant dependence on the NPs concentration. The chemical reaction is lower (0.031 min^{-1}) in the case of 6.25 mg/L NPs. However, the constant grows to the value 0.674 min^{-1} in the chemical reactor with a 0.1 g/L. The dependence of rate constant on the NPs concentration can be easily checked in the (B) graph of Fig. 8.9. Here, the overlapping of rate constants for S2 and S3 samples can be observed at concentration 0.025 g/L. The higher concentrations lead to a more efficient reaction in the sample S3.

The performance of the last samples' batch was the best for all the concentrations. This observation makes sense because these samples include the highest amount of Pd. The comparison of calculated k_c leads to the same trend of results (2.49, 9.09, 11.86 L/g/min for S2, S3, and S4 sample, respectively). Moreover, the performances of catalysts were compared with the other catalysts in Tab. 8.4, which show important parameters for the catalysis. Note that the content of Pd NPs serves to compare the amount of catalyst, which is probably most responsible for

Sample	NPs (μg)	4-NP (μmol)	NPs/4-NP (μg/μmol)	NaBH$_4$ (μmol)	K (min^{-1})	Pd content (%)
This study	6.25	0.12	52.1	12	0.109	8.35
Pd-Ni [186]	200	14	14.3	12	0.054	46.94
Pd-Ni [187]	200	14	14.3	12	0.552	46.90
Pd-Ni [188]	10000	60	166.7	3000	0.272	4.85
Pd [189]	200	62.5	3.2	6250	0.035	100

Table 8.4: Comparison of catalytic properties of Pd-Ni NPs reported in the literature

the catalytic reaction. Since the S3 and S4 samples can contain individual Pd NPs, the S2 sample is included in the table as a representative of Pd-NiO$_z$ NPs.

In summary, all Pd-based samples exhibit degradation of absorbance at 401 nm, and consequently, the chosen optimal concentration for more precise tests in HPLC was the minimal one, i.e., 0.625 g/L. Nevertheless, as mentioned in the methodology chapter, the transformation of 4-NP in bigger mixed chemical reactors with 20 mL volumes was too fast to get any reliable data. The reaction slowdown was realized by decreasing the NPs concentration to half.

In the following catalytic experiments, the components produced in the chemical reactors were analyzed by high-performance liquid chromatography, while the detected peaks were integrated and transformed in concentration values of 4-NP and 4-AP. The concentration results are summarized in Fig. 8.10 together with the calculated degradation efficiency, conversion, selectivity, and TOF.

The samples S2 and S3 were not wholly degraded after 10 minutes. Although the final conversions of both samples were the same, the S2 sample had a faster reaction in the first minute. Thus, the TOF calculated after degradation of a significant part of 4-NP was higher for S2 than S3. The slow reaction of the S3 sample, which was also detected from the screening tests, can be caused by a low amount of free catalysts' active sites due to the attachment of Pd NPs on NiO$_z$. The large amount of Pd NPs near the NiO$_z$ particle can decrease a free space around particles, and then the attachment of 4-nitrophenolate becomes more difficult than in the sample S2, where the molecules interact with the NiO$_z$ with a significantly less surrounded surface by Pd NPs. Besides, in the S4 sample, the reaction was swift even for a concentration of 0.3125 g/L. The total degradation of 4-NP and conversion to 4-AP was completed in an aliquot after 1 minute of reaction. In addition, the reaction could be done in less than 60 seconds.

Consequently, the TOF value was higher than 3181 h^{-1}, which overcomes the TOF of Pd heterogeneous catalysts NPs [190], Pd/PNGO [191], and in other of magnitude compete with Pd/rGO [192], the highest value ever reported in the heterogeneous catalysis, which indicates a highly promising performance of our catalysts. Nevertheless, the reaction here is performed more probably on the higher number of the individual Pd NPs, which are not in contact with NiO$_z$. Thus, this mechanism can enable the S4 sample to perform all the samples' best catalytic activity and avoid sample S3 issues. Alternatively, the NPs in the sample S3 can also exhibit a longer retention time than the other samples. However, this is not probable since
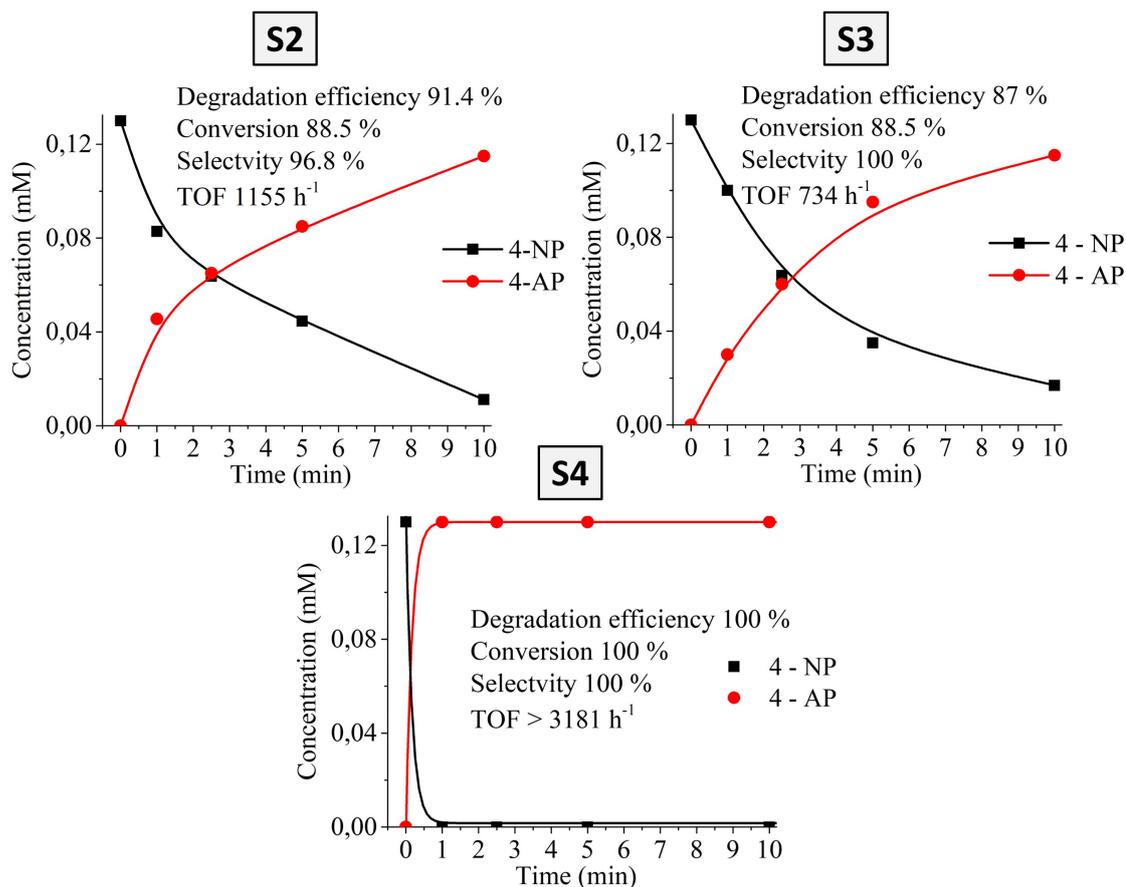
Figure 8.10: Evolution of the 4-NP reduction to 4-AP using 6.25 mg/L of Ni-based catalysts.

there is no reason for this effect, and the chemical reactors were correctly mixed with the same conditions.

8.1.8 VSM

The nickel foil was used for the production of Ni-based NPs, which should enable the final nanostructure to be manipulated by applying a magnetic field. In this thesis, the Ni-based NPs are tested by VSM (Model 7404, Lake Shore, USA) in a magnetic field of $\pm$ 15 kOe at ambient conditions. The samples are inserted into a VSM sample holder (730931 Kel-F, powder upper/bottom cup) mounted on a fiberglass tail with a vibration frequency of 82 Hz, employed vibration amplitude of 1.5 mm and time constant of 100 ms.

The VSM spectra are displayed in Fig. 8.11, which shows the hysteresis loops of the samples. Moreover, the magnetic saturation, coercivity, remanent magnetization, remanence ratio, and anisotropy constant were calculated based on them and summarized in Tab. 8.5. In general, all samples display a ferromagnetic behavior.

The highest performances in saturation and remanent magnetizations were ob-
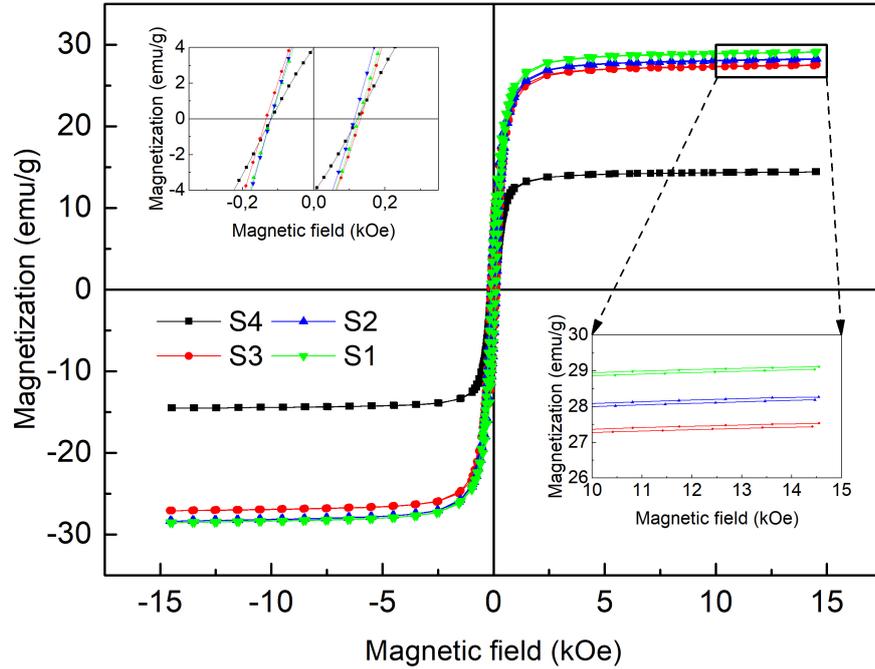
Figure 8.11: Representative VSM hysteresis loops of all samples. The upper-left inset displays the magnification of the zero-field region and the bottom-right one displays the magnification of the magnetic saturation region for the three samples with the highest magnetization.

tained for the S1 sample, including only NiO_z NPs. The magnetizations of S2 and S3 samples were almost the same, whereas a decrease can be observed in S4 sample almost to half of the others. Both values in all the samples are highly compatible (Tab. 8.6) with the ones reported for Pd-Ni nanoalloys [186], Pd-Ni with template and Pd-Ni bulk material [193] or Pd-Ni/NrGO nanodimers [194].

Sample	M_S (emu · g^{-1})	H_C (Oe)	M_R (emu · g^{-1})	M_R/M_S (a.u.)	K (emu · Oe · g^{-1})
S1	29.1	120	7.4	0.254	3563
S2	28.3	120	6.9	0.244	3465
S3	27.5	133	7.3	0.265	3732
S4	14.4	119	4.0	0.278	1749

Table 8.5: Magnetic parameters of the generated Ni-based nanoalloys

In general, the magnetization of the samples depends on the content of the Ni:Pd ratio showed by the EDX analysis, which is consistent with the theoretical predictions. As it was reported, the non-magnetic compounds like Pd NPs cause a continuous decrease in the magnetic performance [195]. In addition, the same trend

was observed for the anisotropy constants. The magneto-crystalline anisotropies, which relate to these values [196], are probably the same for all Ni-based NPs. Since the S4 sample contains more Pd NPs, the relative amount of NiO_z NPs is lower together with the anisotropy value. However, the magnetocrystalline anisotropy of NiO_z NPs itself is comparable with the other samples. The S3 sample exhibits high magnetic performance, but the threshold for the significant changes of magnetic properties should be between the concentration of S3 and S4 samples.

Sample	M_S (emu · g^{-1})	H_C (Oe)	M_R (emu · g^{-1})	Size (nm)	Ni content (%)
This study	27.5	133	7.3	33.8	≤ 47.2
Pd-Ni [83]	73.6	98	19.4	- (NPs)	66
Pd-Ni [186]	17.5	113	2.4	19	53.1
Pd-Ni [193]	26.6	-	-	bulk	40
Pd-Ni/CT [193]	2.76	32	-	5	4.9
Pd-Ni/NrGO [194]	8.11	77.1	1.02	5	19.8

Table 8.6: Comparison of magnetic properties of Pd-Ni NPs reported in the literature

In summary, the amount of Pd NPs does not strongly influence the magnetic properties until the concentration threshold is overcome, as in the S4 sample. The sample S3 used for comparison with the other studies represents the second-highest magnetic performance in the context of M_S/(Ni content) ratio and M_r/(Ni content) ratio. However, the difference between the samples can also be caused by the difference in the size of crystals.

8.2   Pd-NiO$_z$ NPs and graphene-based nanosupport

The decoration of graphene-based nanosupports with the prepared NPs was performed to get the catalyst-support nanocatalyst. The methodology for the preparation of these nanocatalysts is described in the methodology chapter. Since the phenomenon responsible for the graphene-based nanosupport decoration should be physisorption, the electrostatic attraction between NPs and the graphene material must be appreciable. The chosen supporting material is prGO, which should enable the decoration of its structure as a GO and at the same time should have beneficial properties of rGO coming from the structure defects [197] and higher conductivity [100]. The prGO also should have evident electrostatic stability, which makes the prGO ideal for our study. To get details about the surface charge of materials, the Laser Doppler Electrophoresis (LDE) was performed.

8.2.1   LDE

Firstly, the NPs were tested at the samples' native pH (7.35-7.36), determined by a pH meter. The samples' Zeta potentials and measured pH values are displayed

in the table 8.7, where the voltage values are related to the stability of the colloid. The used instrument was a Zetasizer Nano ZS90 (Malvern Instruments Ltd., laser wavelength centered at 632.8 nm). Since the values beyond $|30mV|$ indicate long-term stability [164], the samples can be considered long-term stable. The stability of the NPs is out of the study. However, such values indicate the necessity to ensure stability employing a capping agent. The studied part is the positivity or negativity of the potential. Since all the samples exhibit a positive Zeta potential value, the physisorption of the graphene-based material will be enabled only on a negatively charged surface. An issue comes from the opposite situation, when the NPs and graphene-based material repel, which can be solved by changing the medium's pH [198]. The native surface charging is then changed. The changes are continuous and finally leads to the Zeta potential equaled the zero. This point is known as an isoelectric point, which constitutes no free electric charge barrier around the material.

Sample	Zeta potential (mV)		pH
	Main peak	Side peak	
S1	13.2 ± 5.7	-	7.35 ± 0.05
S2	10.1 ± 4.6	25.0 ± 0.1	7.36 ± 0.07
S3	22.9 ± 3.7	-	7.36 ± 0.05
S4	18.2 ± 5.3	6.3 ± 5.1	7.35 ± 0.06

Table 8.7: Representative zeta potential values of all samples. The main peaks show the predominant zeta potential value, and the side peaks give information about the observed less intense peaks.

Precisely, the Zeta potential of the S1 sample corresponds solely to the nickel NPs. The value beyond 10 mV represents an incipient instability indicating that the NiO_z NPs can agglomerate. A similar central peak was also measured for the S2 sample at 10.1 mV, which probably again belongs to the NiO_z NPs. Besides, a side peak with lower intensity was also found at 25.0 mV. Since the S2 sample contains Pd NPs aside from the NiO_z NPs, the peak with a significantly higher value can be associated with the NiO_z NPs surrounded by the Pd ones.

The S3 sample exhibits only the central peak and no side peak. The peak around 10-13 mV previously assigned to the NiO_z NPs disappears. The explanation can be related to the creation of $Pd-NiO_z$ nanostructures, which can not be easily separated. The Pd NPs surround the NiO_z NPs and form their capping agent. Since Pd NPs can surround the majority of Ni NPs, only one central peak was detected.

A similar central peak to the one of the S3 sample was observed for the S4 sample. Here, the central peak can mean the creation of the same $Pd-NiO_z$ nanostructures. However, the amount of Pd NPs in the sample is significantly higher than in the previous ones. The excess of Pd NPs can lead to measuring separated Pd NPs, leading to the side peak. Compared to the other described side peaks, the one belonging to the S4 sample was much more significant, and its intensity was connected with 48.9% of the intensity area.

After measuring the Zeta potential of NPs, the measurement of prGO followed in different pH conditions (Fig. 8.12). The pH value was changed by adding small volumes of diluted H_3PO_4. Since the rGO and GO exhibit a different behavior in pH and especially a different isoelectric point, this analysis serves as a seminal study of the graphene-based material. However, the main reason for the analysis is the study of the graphene material stability and its ability to enable the physisorption of the prepared NPs.
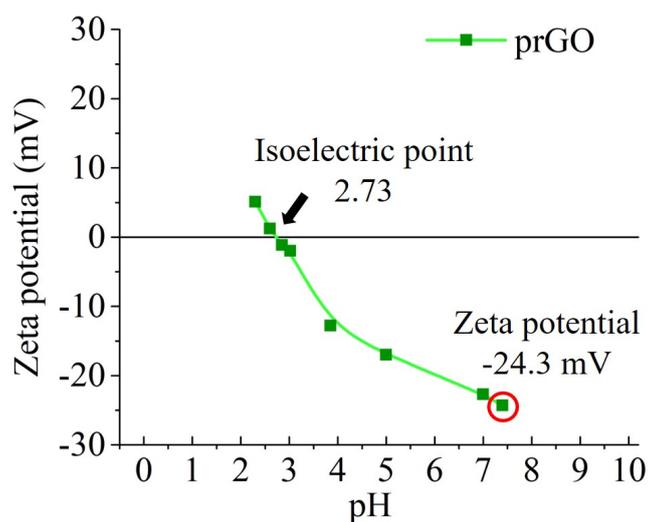
Figure 8.12: Zeta potential of the prepared prGO solution depending on the medium's pH. The red circle highlights the zeta potential at the pH used for the NPs synthesis.

The experiments started at the pH value of NPs, which showed a good condition for the NPs decoration. The Zeta potential was similar in value to the mostly stabilized NPs, but the potential was negative as it was required. Then, the prepared analysis continued to the lower pHs, while the more acidic pH led to overcoming the zero potential value. To find the isoeletric point more precisely, the step in pH was shortened. Finally, the measured values were interpolated by a curve. The calculated isoelectric point corresponds well with the one of rGO [199]. Since the highest negative Zeta potential was determined at the pH, which was detected in the samples with NPs, the physisorption-mediated decoration of the prGO by the NPs was made at the NPs native pH conditions. After the decoration, the nanocatalysts were analyzed by TEM, among the other techniques.

8.2.2 TEM

The TEM analysis includes general pictures of the prepared nanocatalysts in dark field (Fig. 8.13). The dark field permits to see the NPs loading on the graphene-based nanosupports easily. The particles in all the pictures exhibit the same size

distributions as the one before decorating graphene-based sheets. The crucial difference between the sample is in the NPs loading.
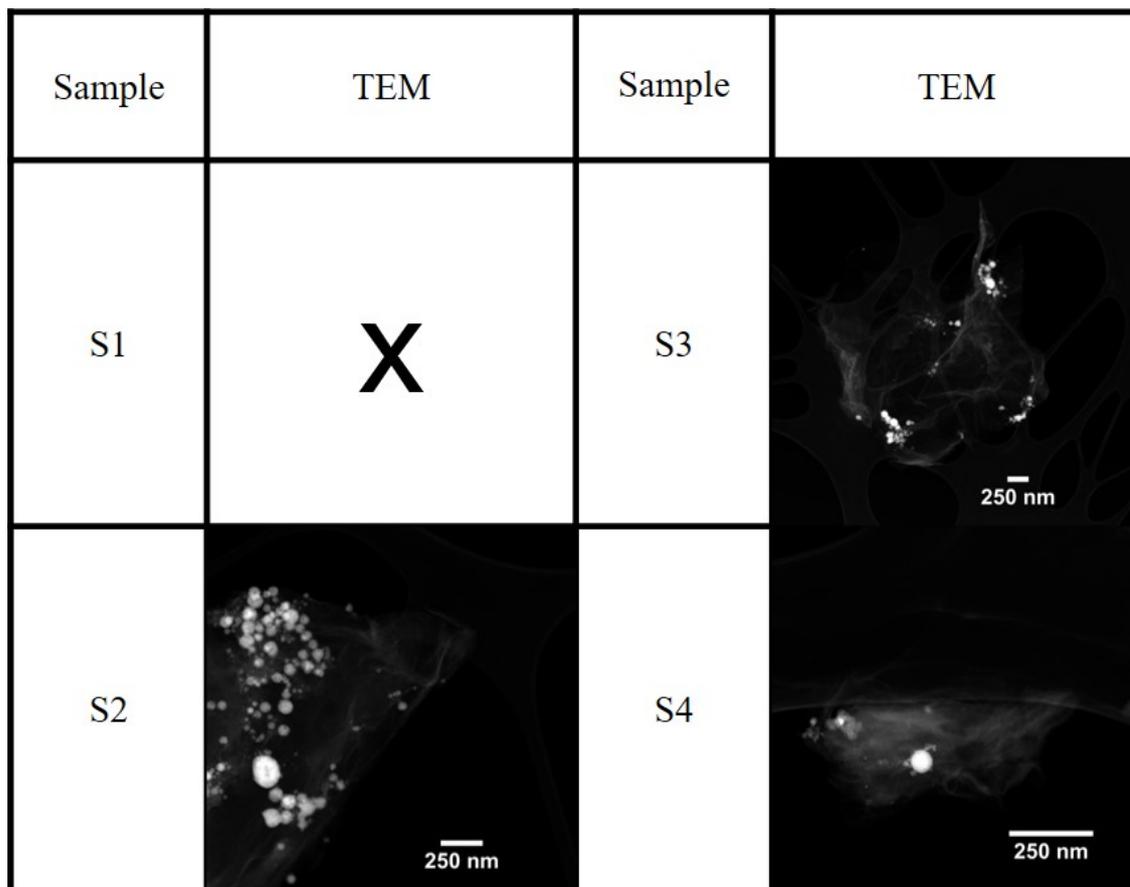
Figure 8.13: Representative TEM pictures of graphene-based nanosupports decorated by Pd-NiO$_z$ NPs

Although, the NPs look to be attached in all samples. The S4 sample represents the nanocatalyst with the lowest loading. In the picture, it is visible two positions with highly agglomerated particles. The lowest stability, together with the highest amount of Pd NPs, led to fast agglomeration and the impossibility to attach the NPs properly on the graphene-based material surface. Especially, it was possible to observe a huge amount of agglomerated NPs in some sample places. Alternatively, the lowest Zeta potential difference can avoid the physisorption, and thus, the agglomeration process could occur later.

In sample S3, the loading of NPs is higher, and the particles seem to be more distributed on the graphene-based material surface. Moreover, there are some places with attached small NPs, which can represent the separated Pd NPs. The number of places with NPs is also low, like in the previous sample. However, there is no remaining NPs material around, which could be connected with the low stability of NPs and their agglomeration. Since the material looks to be mostly attached, the higher leaching of NPs can be a probable reason for the low decoration of big NPs.

Alternatively, the presence of Pd NPs surrounding the NiO_z NPs can disable the physisorption of NiO_z NPs on the graphene-based material. This presumption can explain the extremely high NPs loading in the S2 sample.

The last analyzed sample exhibits a highly uniform loading of NPs. Here, the small and big NPs are located on each graphene-based material sheet without significant agglomeration of NPs near the decoration places. As it was mentioned, the high Pd content around NiO_z NPs probably causes the lower physisorption efficiency in the high Pd containing samples. In contrast, the S2 sample has only 8.35 % mass of Pd NPs included. The physisorption between the NPs and graphene-based material is much more effective in this sample, and then it can seem that only the NiO_z are responsible for the sorption of the material on the sheets. However, in all samples, it is possible to observe small NPs absorbed on the sheets together with some big ones. Therefore, the decoration of the graphene-based material is probably made by Pd-NiO_z and also Pd NPs, while the particle responsible for the successful sorption of Pd-NiO_z is the NiO_z particle. The high amount of Pd NPs around the NiO_z disables the physisorption on the graphene-based material, but a lower amount of Pd NPs gives a change to the Pd-NiO_z to be absorbed reliably.

In summary, the S2 sample represents the material, which can benefit the most from the adsorption to the graphene-based nanosupport. Although the decoration mechanism is based on physisorption, the difference between the samples can also be connected with the different surface chemistry of graphene-based materials. To understand more the chemistry and surface functionalization of the prepared graphene-based materials, the analysis by Raman and FTIR spectroscopies is included.

8.2.3 Raman spectroscopy and FTIR

In our study, the DXR Raman Microscope (Thermo Scientific, USA) and the FTIR Nicolet Antaris IGS (Thermo Scientific, USA) are used to analyzing the graphene-based samples. The spectra are taken from 3500 to 50 cm^{-1} in Raman spectroscopy and from 4000 to 400 cm^{-1} in FTIR.

The peaks in Raman spectra (Fig. 8.14) are located around 2916, 2677, 1590, and 1352 cm^{-1} in all the samples that represent D+D' / 2D, which are not used for the analysis and G / D bands, respectively [200, 201]. The G band corresponds to the first-order scattering of the E2g Raman mode, and the D band represents the reduction in the size of the in-plane sp2 domains and defects in the sp2 structure [201]. The 2D band is the second order of the D band and can be used when the D band is suppressed due to the low number of defects in the structure.

The parameter indicating a reduction of GO is represented by the intensity ratio of D and G bands. In our case, the ratio values are 0.878, 0.853, 0.901, 1.001 for prGO, S2-prGO, S3-prGO, S4-prGO, respectively. The value is too low in the first sample, so it is more probable that the GO is observed rather than rGO. Moreover, there is no blue shift for the G and D bands, which is typical for rGO. This well corresponds to the prGO. However, the post-processing oxidation of the sample due to exposure to the environment is also possible. Conversely, a high D/G ratio and

blue shift are visible in the S4 sample and partly also in the S3 sample.
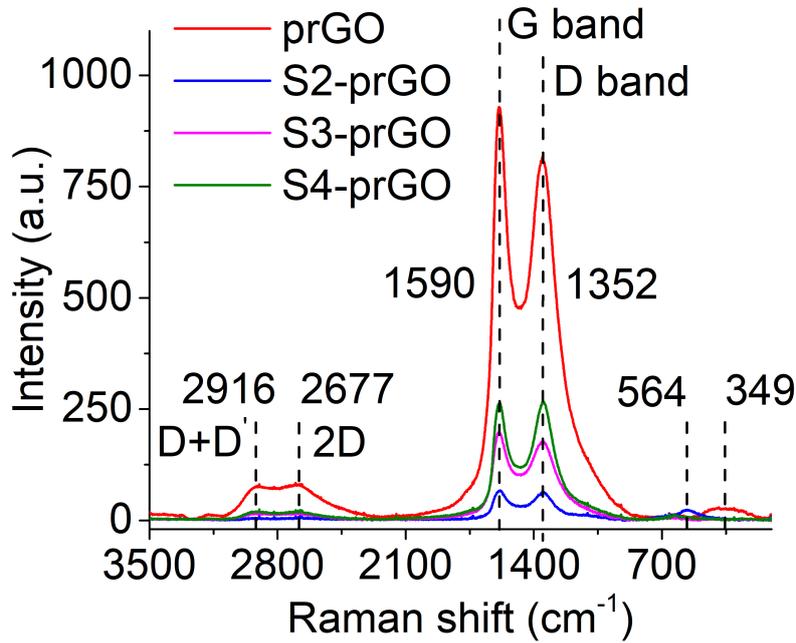
Figure 8.14: Representative Raman spectra for graphene-based materials

Since these samples also exhibit the low loading of NPs, the creation of more reduced GO can be the reason for the lower decoration. Possibly, the contact between species led to the post-reduction of the graphene-based material surface. The later reduced GO not enabled an effective decoration of its surface by the NPs. Since the support material increased the level of reduction, the NPs should become more oxidized in S3 and S4 samples. The opposite situation occurs with S2 NPs, while in this sample, the decoration was probably promoted mainly by NiO_z NPs instead of Pd ones. The NiO_z were oxidized, and thus further oxidation of their surface was not possible. The opposite situation occurs in S3 and S4 samples, which are probably predominantly composed of the Pd NPs. These particles do not exhibit any oxide incorporated in the structure, and thus the NPs could be oxidized.

The connection between the surface chemistry of the graphene-based material and its decoration by the Pd-NiO_z NPs are found. Nevertheless, a better understanding of specific groups on the prGO is given by FTIR analysis (Fig. 8.15).

The most prominent peaks within the FTIR spectra are located at 2357, 1724, 1540, and 1010 cm^{-1}. The last three peaks represent C=O, C=C [202], and C-O [203] functional groups on the prGO planes, respectively. The mentioned groups, which are well visible in all samples aside from the S3, indicate the GO structure. Nevertheless, their relative intensities compared to the background are small, which can be connected with partial reduction of the material. The small absorbance intensity from the low amount of analyzed material causes difficulties with the groups' detection in the sample S3. Nevertheless, small peaks of C=O and C=C are visible in the raw data.
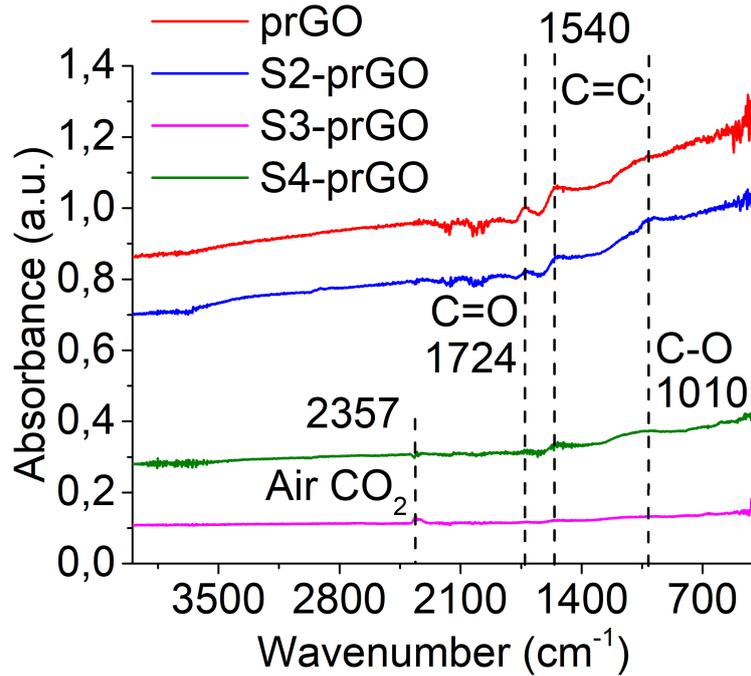
Figure 8.15: Representative FTIR graph for graphene-based materials

In comparison with the usual GO spectrum, the samples do not exhibit peaks corresponding to the C-OH and C-H around 3390 and 3060 cm^{-1}, respectively [204]. The significant decrease in these specific groups means that the decoration of prGO occurred on the specific groups (C=O, C-O) or on the locations of the defects of prGO structure. The highest relative intensity of C-O peak in the S2 sample can indicate the connection between the loading of NPs in the structure and the number of C-O groups.

Finally, the additional peak at 2357 cm^{-1}, which is detected only in S3 sample, can be associated with the adsorption of carbon dioxide on the material from the air environment [204, 205].

9 Conclusion

In the current thesis, we are presenting the laser-mediated synthesis of palladium-nickel NPs in water. The used reactive ablation methodology combines the laser photoreaction of Pd salt and laser ablation of a Ni foil in a single step process, while no use of hazardous precursor is necessary. Thus, this can be considered a green methodology for the preparation of palladium-nickel nanocolloids. The irradiation of the Ni foil immersed in various Pd salt aqueous solutions with low laser intensities provided the conditions required for the material's synthesis. Moreover, the selection of low intensities also enabled avoiding side laser-mediated effects as LFL or LML. As an additional consequence, the low energy plasma led to the low optical breakdown effect. Thus, unlike what occurs with the traditional RLAL practice, the final Pd-NiO$_z$ NPs were produced only due to the reduction of Pd salt ions by hot Ni species coming from the sub-nanosecond timescale region of the ablation reaction.

The optimized parameters used for the nanocolloid generation were determined as a laser fluence < 10 J/m^2, 0.9 MHz repetition rate, and 3 mm water layer above the Ni foil. These conditions led to the preparation of nanomaterials with 33-38 nm NiO$_z$ NPs, which were surrounded by 7 nm Pd NPs, while their content in the sample was proportional to the amount of the used Pd salt in the reaction. The saturation level of connection between NiO$_z$ and Pd NPs is around 1:1 Pd:Ni, which was observed in two samples prepared using different origin Pd salt concentrations. The mechanism responsible for the interaction between the NPs can be MSI, which influences the behavior of NPs by the charge transfer between the support and metal. Moreover, the Pd NPs were probably surrounded by a Ni skin. The amount of oxygen in the samples determined by EDX was relatively low, which indicates a z « 1 for NiO$_z$ NPs. The structural composition of NiO$_z$ is probably a mixture mainly composed of the NiO$_x$ NPs and a small number of core-shell Ni-based particles with the oxidized shell.

Further, the catalytic activity of the prepared nanomaterials was tested on the efficiency to degrade a highly used industrial pollutant of the environment, 4-NP. The measured catalytic activity was competitive with the ones reported in other studies, while as expected, the amount of Pd NPs in the mixtures played a significant role in the materials' catalytic power. Although the reactions' selectivity was around 100% in all the samples, the Pd content didn't significantly influence this value in any sample.

The following magnetic performance was, on the other hand, connected with the content of NiO$_z$ NPs, which cause a ferromagnetic behavior in the whole mixture. In addition, the detected magnetizations were the second-highest from the samples

with Pd-Ni nanoalloys found in the literature.

The magneto-catalytic NPs were subsequently attached to prGO nanosupports by physisorption at the native pH of NPs. The decoration of graphene-based sheets was observed in all the samples. Nevertheless, the best decoration was observed in the samples that included a minor amount of Pd NPs, which can be due to these NPs were acting as protection agents avoiding the NiO_z NPs sorption on prGO. Besides, the effectively attached NPs were immobilized over prGO in formations including Pd-NiO_z NPs or separated individual Pd NPs, while the positions susceptible for decoration on the prGO were probably represented by C=O, C-O chemical groups, and defects in the graphene plane structure.

Overall, this methodology brings the long-awaited promise of environmentally-friendly synthesized magnetically manipulable powerful catalysts for their exploitation in heterogeneous catalysis. The future steps for the current project encompass the fabrication of nanofibrous sponge composites as macrosupports for the Pd-NiO_z/prGO catalysts. The final decorated nanosponge (Fig. 9.1) may be implemented in real applications of Pd-Ni nanoalloys, which includes, e.g., the creation of methanol or ethanol fuel cells [206, 207, 208], organic synthesis (e.g. Suzuki-Miyaura reaction [209, 210], Miyaura–Heck reaction [211], Heck and Sonogashira reactions [209]), hydrogen storage [212, 213], and gas sensing [214, 215].
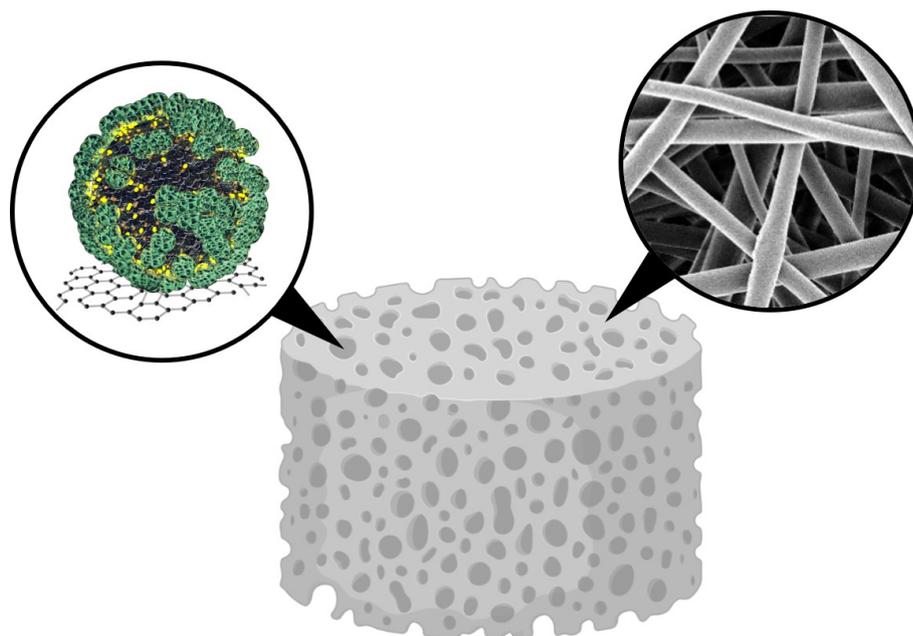
Figure 9.1: Scheme of a nanofibrous nanosponge decorated by Pd-NiO_z/Graphene-based nanosupports. Image was created with the help of BioRender.com

10 Scientific contribution

Published scientific papers

TORRES-MENDIETA, Rafael; YALCINKAYA, Fatma; BOYRAZ, Evren; **HAVELKA, Ondřej**; WACŁAWEK, S; MARYŠKA, Jiří; ČERNÍK, Miroslav ; BRYJAK, Marek. PVDF nanofibrous membranes modified via laser-synthesized Ag nanoparticles for a cleaner oily water separation. *Applied Surface Science.* 2020, vol. 526, pp. 146575. (Top decile, IF 6.182)

CVEK, Martin; TORRES-MENDIETA, Rafael; **HAVELKA, Ondřej**; URBÁNEK, Michal; PLACHÝ, Tomáš; ČERNÍK, Miroslav. Laser-induced fragmentation of carbonyl iron as a clean method to enhance magnetorheological effect. *Journal of Cleaner Production.* 2020, vol. 254, pp. 120182. (Top decile, IF 7.246)

TORRES-MENDIETA, Rafael; **HAVELKA, Ondřej**; URBÁNEK, Michal;CVEK, Martin; WACŁAWEK, Stanisław; PADIL, Vinod Vellora Thekkae; JAŠÍKOVÁ, Darina; KOTEK, Michal; ČERNÍK, Miroslav. Laser-assisted synthesis of Fe-Cu oxide nanocrystals. *Applied Surface Science.* 2019, vol. 469, pp.1007–1015. (Top decile, IF 6.182)

Submitted scientific papers

HAVELKA, Ondřej; CVEK, Martin; URBÁNEK, Michal; JAŠÍKOVÁ, Darina; KOTEK, Michal; ČERNÍK, Miroslav; AMENDOLA, Vincenzo; TORRES-MENDIETA, Rafael. On the laser fragmentation for the synthesis of ligand-free ultra-small iron nanoparticles in various liquid environments. *Nanomaterials.* 2021, submitted.

ETTEL, David; **HAVELKA, Ondřej**; Seling¨ul Isik, SILVESTRI, Daniele; WACŁAWEK, Stanislaw; URBANEK, Michal; PADIL; Vinod V.T.; ČERNÍK, Miroslav; YALCINKAYA, Fatma; TORRES-MENDIETA, Rafael . Laser-synthesized Ag/TiO nanoparticles to integrate catalytic pollutant degradation and antifouling enhancement in nanofibrous membranes for oil-water separation. *Applied Surface Science.* 2021, submitted.

References

[1] GEWIN, Virginia. Nanobiotechnology: small talk. *Nature*. 2006, vol. 444, no. 7118, pp. 514–515. Available from DOI: `10.1038/nj7118-514a`.

[2] HULLA, JE; SAHU, SC; HAYES, AW. Nanotechnology: History and future. *Human & experimental toxicology*. 2015, vol. 34, no. 12, pp. 1318–1321. Available from DOI: `10.1177/0960327115603588`.

[3] ODOM, Teri W; PILENI, Marie-Paule. Nanoscience. *Accounts of chemical research*. 2008, vol. 12, no. 41, pp. 1565–1565. Available from DOI: `10.1021/ar800253n`.

[4] ZHANG, Dongshi; GÖKCE, Bilal; BARCIKOWSKI, Stephan. Laser synthesis and processing of colloids: fundamentals and applications. *Chemical reviews*. 2017, vol. 117, no. 5, pp. 3990–4103. Available from DOI: `10.1021/acs.chemrev.6b00468`.

[5] MULVIHILL, Martin J; BEACH, Evan S; ZIMMERMAN, Julie B; ANASTAS, Paul T. Green chemistry and green engineering: a framework for sustainable technology development. *Annual review of environment and resources*. 2011, vol. 36, pp. 271–293. Available from DOI: `10.1146/annurev-environ-032009-095500`.

[6] LU, Yuan; OZCAN, Soydan. Green nanomaterials: On track for a sustainable future. *Nano Today*. 2015, vol. 10, no. 4, pp. 417–420. Available from DOI: `10.1016/j.nantod.2015.04.010`.

[7] RODUNER, Emil. Size matters: why nanomaterials are different. *Chemical Society Reviews*. 2006, vol. 35, no. 7, pp. 583–592. Available from DOI: `10.1039/B502142C`.

[8] RAY, Paresh Chandra. Size and shape dependent second order nonlinear optical properties of nanomaterials and their application in biological and chemical sensing. *Chemical reviews*. 2010, vol. 110, no. 9, pp. 5332–5365. Available from DOI: `10.1021/cr900335q`.

[9] GOYAL, Monika; GUPTA, BRK. Study of shape, size and temperature-dependent elastic properties of nanomaterials. *Modern Physics Letters B*. 2019, vol. 33, no. 26, pp. 1950310. Available from DOI: `10.1142/S021798491950310X`.

[10] KARIMI-MALEH, Hassan; CELLAT, Kemal; ARIKAN, Kubilay; SAVK, Aysun; KARIMI, Fatemeh; ŞEN, Fatih. Palladium–Nickel nanoparticles decorated on Functionalized-MWCNT for high precision non-enzymatic glucose sensing. *Materials Chemistry and Physics*. 2020, vol. 250, pp. 123042. Available from DOI: `10.1016/j.matchemphys.2020.123042`.

[11] YIN, Xi-Tao et al. A highly sensitivity and selectivity Pt-SnO2 nanoparticles for sensing applications at extremely low level hydrogen gas detection. *Journal of alloys and compounds*. 2019, vol. 805, pp. 229–236. Available from DOI: `10.1016/j.jallcom.2019.07.081`.

[12] SAHA, Krishnendu; AGASTI, Sarit S; KIM, Chaekyu; LI, Xiaoning; ROTELLO, Vincent M. Gold nanoparticles in chemical and biological sensing. *Chemical reviews*. 2012, vol. 112, no. 5, pp. 2739–2779. Available from DOI: `10.1021/cr2001178`.

[13] CVEK, Martin; TORRES-MENDIETA, Rafael; HAVELKA, Ondrej; URBANEK, Michal; PLACHY, Tomas; CERNIK, Miroslav. Laser-induced fragmentation of carbonyl iron as a clean method to enhance magnetorheological effect. *Journal of Cleaner Production*. 2020, vol. 254, pp. 120182. Available from DOI: `10.1016/j.jclepro.2020.120182`.

[14] HAJALILOU, Abdollah; KIANVASH, Abbas; SHAMELI, Kamyar; LAVVAFI, Hossein. Carbonyl iron based magnetorheological effects with silver nanoparticles via green-assisted coating. *Applied Physics Letters*. 2017, vol. 110, no. 26, pp. 261902. Available from DOI: `10.1063/1.4990679`.

[15] KUMAR, James Sathya; PAUL, P Sam; RAGHUNATHAN, Girish; ALEX, Divin George. A review of challenges and solutions in the preparation and use of magnetorheological fluids. *International Journal of Mechanical and Materials Engineering*. 2019, vol. 14, no. 1, pp. 1–18. Available from DOI: `10.1186/s40712-019-0109-2`.

[16] MCNAMARA, Karrina; TOFAIL, Syed AM. Nanoparticles in biomedical applications. *Advances in Physics: X*. 2017, vol. 2, no. 1, pp. 54–88. Available from DOI: `10.1080/23746149.2016.1254570`.

[17] AZHARUDDIN, Mohammad; ZHU, Geyunjian H; DAS, Debapratim; OZGUR, Erdogan; UZUN, Lokman; TURNER, Anthony PF; PATRA, Hirak K. A repertoire of biomedical applications of noble metal nanoparticles. *Chemical Communications*. 2019, vol. 55, no. 49, pp. 6964–6996. Available from DOI: `10.1039/C9CC01741K`.

[18] DREADEN, Erik C; ALKILANY, Alaaldin M; HUANG, Xiaohua; MURPHY, Catherine J; EL-SAYED, Mostafa A. The golden age: gold nanoparticles for biomedicine. *Chemical Society Reviews*. 2012, vol. 41, no. 7, pp. 2740–2779. Available from DOI: `10.1039/C1CS15237H`.

[19] IRAVANI, Siavash; VARMA, Rajender S. Plant-derived edible nanoparticles and miRNAs: emerging frontier for therapeutics and targeted drug-delivery. *ACS Sustainable Chemistry & Engineering.* 2019, vol. 7, no. 9, pp. 8055–8069. Available from DOI: `10.1021/acssuschemeng.9b00954`.

[20] IRAVANI, Siavash; VARMA, Rajender S. Biofactories: engineered nanoparticles via genetically engineered organisms. *Green Chemistry.* 2019, vol. 21, no. 17, pp. 4583–4603. Available from DOI: `10.1039/C9GC01759C`.

[21] DE JONG, Wim H; BORM, Paul JA. Drug delivery and nanoparticles: applications and hazards. *International journal of nanomedicine.* 2008, vol. 3, no. 2, pp. 133. Available from DOI: `10.2147/ijn.s596`.

[22] POLSHETTIWAR, Vivek; VARMA, Rajender S. Green chemistry by nanocatalysis. *Green Chemistry.* 2010, vol. 12, no. 5, pp. 743–754. Available from DOI: `10.1039/B921171C`.

[23] SCHAUERMANN, Swetlana; NILIUS, Niklas; SHAIKHUTDINOV, Shamil; FREUND, Hans-Joachim. Nanoparticles for heterogeneous catalysis: new mechanistic insights. *Accounts of chemical research.* 2013, vol. 46, no. 8, pp. 1673–1681. Available from DOI: `10.1021/ar300225s`.

[24] ASTRUC, Didier; LU, Feng; ARANZAES, Jaime Ruiz. Nanoparticles as recyclable catalysts: the frontier between homogeneous and heterogeneous catalysis. *Angewandte Chemie International Edition.* 2005, vol. 44, no. 48, pp. 7852–7872. Available from DOI: `10.1002/anie.200500766`.

[25] WU, Ming-Chung; HSIAO, Kai-Chi; CHANG, Yin-Hsuan; CHAN, Shun-Hsiang. Photocatalytic hydrogen evolution of palladium nanoparticles decorated black TiO2 calcined in argon atmosphere. *Applied Surface Science.* 2018, vol. 430, pp. 407–414. Available from DOI: `10.1016/j.apsusc.2017.08.071`.

[26] ELSEY, Justin; BUBLEY, Jeffrey A; ZHU, Lei; RAO, Shikha; SASAKI, Maiko; POLLACK, Brian P; YANG, Lily; ARBISER, Jack L. Palladium based nanoparticles for the treatment of advanced melanoma. *Scientific reports.* 2019, vol. 9, no. 1, pp. 1–9. Available from DOI: `10.1038/s41598-019-40258-6`.

[27] MUNIZ, Kilian. High-oxidation-state palladium catalysis: new reactivity for organic synthesis. *Angewandte Chemie International Edition.* 2009, vol. 48, no. 50, pp. 9412–9423. Available from DOI: `10.1002/anie.200903671`.

[28] LIU, Xiao Yan; WANG, Aiqin; ZHANG, Tao; MOU, Chung-Yuan. Catalysis by gold: New insights into the support effect. *Nano Today.* 2013, vol. 8, no. 4, pp. 403–416. Available from DOI: `10.1016/j.nantod.2013.07.005`.

[29] SHARMA, Gaurav; KUMAR, Amit; SHARMA, Shweta; NAUSHAD, Mu; DWIVEDI, Ram Prakash; ALOTHMAN, Zeid A; MOLA, Genene Tessema. Novel development of nanoparticles to bimetallic nanoparticles and their composites: a review. *Journal of King Saud University-Science.* 2019, vol. 31, no. 2, pp. 257–269. Available from DOI: `10.1016/j.jksus.2017.06.012`.

[30] SEO, Min Ho; CHOI, Sung Mook; SEO, Joon Kyo; NOH, Seung Hyo; KIM, Won Bae; HAN, Byungchan. The graphene-supported palladium and palladium–yttrium nanoparticles for the oxygen reduction and ethanol oxidation reactions: Experimental measurement and computational validation. *Applied Catalysis B: Environmental*. 2013, vol. 129, pp. 163–171. Available from DOI: `10.1016/j.apcatb.2012.09.005`.

[31] NASROLLAHZADEH, Mahmoud; AZARIAN, Abbas; MAHAM, Mehdi; EHSANI, Ali. Synthesis of Au/Pd bimetallic nanoparticles and their application in the Suzuki coupling reaction. *Journal of Industrial and Engineering Chemistry*. 2015, vol. 21, pp. 746–748. Available from DOI: `10.1016/j.jiec.2014.04.006`.

[32] ŞEN, Betül; AYGÜN, Ayşenur; ŞAVK, Aysun; AKOCAK, Süleyman; ŞEN, Fatih. Bimetallic palladium–iridium alloy nanoparticles as highly efficient and stable catalyst for the hydrogen evolution reaction. *International Journal of Hydrogen Energy*. 2018, vol. 43, no. 44, pp. 20183–20191. Available from DOI: `10.1016/j.ijhydene.2018.07.081`.

[33] HARIKA, Villa Krishna; SADHANALA, Hari Krishna; PERELSHTEIN, Ilana; GEDANKEN, Aharon. Sonication-assisted synthesis of bimetallic Hg/Pd alloy nanoparticles for catalytic reduction of nitrophenol and its derivatives. *Ultrasonics sonochemistry*. 2020, vol. 60, pp. 104804. Available from DOI: `10.1016/j.ultsonch.2019.104804`.

[34] GAWANDE, Manoj B; FORNASIERO, Paolo; ZBOŘIL, Radek. Carbon-based single-atom catalysts for advanced applications. *ACS Catalysis*. 2020, vol. 10, no. 3, pp. 2231–2259. Available from DOI: `10.1021/acscatal.9b04217`.

[35] RAWOOL, Sushma A; BELGAMWAR, Rajesh; JANA, Rajkumar; MAITY, Ayan; BHUMLA, Ankit; YIGIT, Nevzat; DATTA, Ayan; RUPPRECHTER, Günther; POLSHETTIWAR, Vivek. Direct CO 2 capture and conversion to fuels on magnesium nanoparticles under ambient conditions simply using water. *Chemical Science*. 2021, vol. 12, no. 16, pp. 5774–5786. Available from DOI: `10.1039/D1SC01113H`.

[36] *Automated Production of Colloidal Nanoparticles* [`https://www.autopronano.eu`]. Accessed: 2021-04-02.

[37] *Advanced Nanoparticle Generation Excitation by Lasers in Liquids 2020* [`http://angel-conference.org/info.asp?sid=167`]. Accessed: 2021-04-03.

[38] AMENDOLA, Vincenzo. *Laser-Assisted Synthesis of Non-Equilibrium Nanoalloys*. Wiley Online Library, 2021. No. 7. Available from DOI: `10.1002/cphc.202000987`.

[39] TYMOCZKO, Anna; KAMP, Marius; REHBOCK, Christoph; KIENLE, Lorenz; CATTARUZZA, Elti; BARCIKOWSKI, Stephan; AMENDOLA, Vincenzo. One-step synthesis of Fe–Au core–shell magnetic-plasmonic nanoparticles driven by interface energy minimization. *Nanoscale Horizons*. 2019, vol. 4, no. 6, pp. 1326–1332. Available from DOI: `10.1039/C9NH00332K`.

[40] BRANDIELE, Riccardo; AMENDOLA, Vincenzo; GUADAGNINI, Andrea; RIZZI, Gian Andrea; BADOCCO, Denis; PASTORE, Paolo; ISSE, Abdirisak Ahmed; DURANTE, Christian; GENNARO, Armando. Facile synthesis of Pd3Y alloy nanoparticles for electrocatalysis of the oxygen reduction reaction. *Electrochimica Acta*. 2019, vol. 320, pp. 134563. Available from DOI: `10.1016/j.electacta.2019.134563`.

[41] BRANDIELE, Riccardo; GUADAGNINI, Andrea; GIRARDI, Leonardo; DRAŽIĆ, Goran; DALCONI, Maria Chiara; RIZZI, Gian Andrea; AMENDOLA, Vincenzo; DURANTE, Christian. Climbing the oxygen reduction reaction volcano plot with laser ablation synthesis of Pt x Y nanoalloys. *Catalysis Science & Technology*. 2020, vol. 10, no. 14, pp. 4503–4508. Available from DOI: `10.1039/D0CY00983K`.

[42] ANASTAS, Paul; EGHBALI, Nicolas. Green chemistry: principles and practice. *Chemical Society Reviews*. 2010, vol. 39, no. 1, pp. 301–312. Available from DOI: `10.1039/B918763B`.

[43] YAM, Kah Meng; GUO, Na; JIANG, Zhuoling; LI, Shulong; ZHANG, Chun. Graphene-based heterogeneous catalysis: role of graphene. *Catalysts*. 2020, vol. 10, no. 1, pp. 53. Available from DOI: `10.3390/catal10010053`.

[44] MACHADO, Bruno F; SERP, Philippe. Graphene-based materials for catalysis. *Catalysis Science & Technology*. 2012, vol. 2, no. 1, pp. 54–75. Available from DOI: `10.1039/C1CY00361E`.

[45] LI, Yimin; SOMORJAI, Gabor A. Nanoscale advances in catalysis and energy applications. *Nano letters*. 2010, vol. 10, no. 7, pp. 2289–2295. Available from DOI: `10.1021/nl101807g`.

[46] MIKA, Laszlo T; CSEFALVAY, Edit; NEMETH, Aron. Catalytic conversion of carbohydrates to initial platform chemicals: chemistry and sustainability. *Chemical reviews*. 2018, vol. 118, no. 2, pp. 505–613. Available from DOI: `10.1021/acs.chemrev.7b00395`.

[47] FECHETE, Ioana; WANG, Ye; VÉDRINE, Jacques C. The past, present and future of heterogeneous catalysis. *Catalysis Today*. 2012, vol. 189, no. 1, pp. 2–27. Available from DOI: `10.1016/j.cattod.2012.04.003`.

[48] RODRÍGUEZ-PADRÓN, Daily; PUENTE-SANTIAGO, Alain R; BALU, Alina M; MUÑOZ-BATISTA, Mario J; LUQUE, Rafael. Environmental catalysis: present and future. *ChemCatChem*. 2019, vol. 11, no. 1, pp. 18–38. Available from DOI: `10.1002/cctc.201801248`.

[49] BUSACCA, Carl A; FANDRICK, Daniel R; SONG, Jinhua J; SENANAYAKE, Chris H. The growing impact of catalysis in the pharmaceutical industry. *Advanced Synthesis & Catalysis*. 2011, vol. 353, no. 11-12, pp. 1825–1864. Available from DOI: `10.1002/adsc.201100488`.

[50] CORMA, Avelino; IBORRA, Sara; VELTY, Alexandra. Chemical routes for the transformation of biomass into chemicals. *Chemical reviews*. 2007, vol. 107, no. 6, pp. 2411–2502. Available from DOI: `10.1021/cr050989d`.

[51] HEVELING, Josef. Heterogeneous catalytic chemistry by example of industrial applications. *Journal of Chemical Education*. 2012, vol. 89, no. 12, pp. 1530–1536. Available from DOI: `10.1021/ed200816g`.

[52] VRIES, Johannes G de; JACKSON, S David. Homogeneous and heterogeneous catalysis in industry. *Catalysis Science & Technology*. 2012, vol. 2, no. 10, pp. 2009–2009. Available from DOI: `10.1039/C2CY90039D`.

[53] WANG, Aiqin; LI, Jun; ZHANG, Tao. Heterogeneous single-atom catalysis. *Nature Reviews Chemistry*. 2018, vol. 2, no. 6, pp. 65–81. Available from DOI: `10.1038/s41570-018-0010-1`.

[54] CORMA, Avelino; GARCIA, Hermenegildo. Crossing the borders between homogeneous and heterogeneous catalysis: developing recoverable and reusable catalytic systems. *Topics in Catalysis*. 2008, vol. 48, no. 1, pp. 8–31. Available from DOI: `10.1007/s11244-008-9056-5`.

[55] ARGYLE, Morris D; BARTHOLOMEW, Calvin H. Heterogeneous catalyst deactivation and regeneration: a review. *Catalysts*. 2015, vol. 5, no. 1, pp. 145–269. Available from DOI: `10.3390/catal5010145`.

[56] ARSALANFAR, M; MIRZAEI, AA; BOZORGZADEH, HR; SAMIMI, A; GHOBADI, R. Effect of support and promoter on the catalytic performance and structural properties of the Fe–Co–Mn catalysts for Fischer–Tropsch synthesis. *Journal of Industrial and Engineering Chemistry*. 2014, vol. 20, no. 4, pp. 1313–1323. Available from DOI: `10.1016/j.jiec.2013.07.011`.

[57] ZHAO, Rui-yu; ZENG, Ling-you; LIANG, Juan; LIU, Chen-guang. Interaction between Ni promoter and Al2O3 support and its effect on the performance of NiMo/γ-Al2O3 catalyst in hydrodesulphurization. *Journal of Fuel Chemistry and Technology*. 2016, vol. 44, no. 5, pp. 564–569. Available from DOI: `10.1016/S1872-5813(16)30026-3`.

[58] SUN, Shengnan; LI, Haiyan; XU, Zhichuan J. Impact of surface area in evaluation of catalyst activity. *Joule*. 2018, vol. 2, no. 6, pp. 1024–1027. Available from DOI: `10.1016/j.joule.2018.05.003`.

[59] ZHU, Jun; HOLMEN, Anders; CHEN, De. Carbon nanomaterials in catalysis: proton affinity, chemical and electronic properties, and their catalytic consequences. *ChemCatChem*. 2013, vol. 5, no. 2, pp. 378–401. Available from DOI: `10.1002/cctc.201200471`.

[60] WATERHOUSE, Geoffrey IN; BOWMAKER, Graham A; METSON, James B. Influence of catalyst morphology on the performance of electrolytic silver catalysts for the partial oxidation of methanol to formaldehyde. *Applied Catalysis A: General.* 2004, vol. 266, no. 2, pp. 257–273. Available from DOI: 10.1016/j.apcata.2004.02.015.

[61] LUHUI, WANG; HUI, LIU; YUAN, LIU; YING, CHEN; SHUQING, YANG. Influence of preparation method on performance of Ni-CeO2 catalysts for reverse water-gas shift reaction. *Journal of Rare Earths.* 2013, vol. 31, no. 6, pp. 559–564. Available from DOI: 10.1016/S1002-0721(12)60320-2.

[62] ROSSETTI, Ilenia; PERNICONE, Nicola; FORNI, Lucio. Promoters effect in Ru/C ammonia synthesis catalyst. *Applied Catalysis A: General.* 2001, vol. 208, no. 1-2, pp. 271–278. Available from DOI: 10.1016/S0926-860X(00)00711-0.

[63] JIANG, Feng; ZHANG, Min; LIU, Bing; XU, Yuebing; LIU, Xiaohao. Insights into the influence of support and potassium or sulfur promoter on iron-based Fischer–Tropsch synthesis: understanding the control of catalytic activity, selectivity to lower olefins, and catalyst deactivation. *Catalysis science & technology.* 2017, vol. 7, no. 5, pp. 1245–1265. Available from DOI: 10.1080/01614940.2020.1762367.

[64] GHOLAMI, Zahra; TIŠLER, Zdeněk; RUBÁŠ, Vlastimil. Recent advances in Fischer-Tropsch synthesis using cobalt-based catalysts: a review on supports, promoters, and reactors. *Catalysis Reviews.* 2020, pp. 1–84. Available from DOI: 10.1080/01614940.2020.1762367.

[65] LIN, Bingyu; WEI, Kemei; MA, Xiaofeng; LIN, Jianxin; NI, Jun. Study of potassium promoter effect for Ru/AC catalysts for ammonia synthesis. *Catalysis Science & Technology.* 2013, vol. 3, no. 5, pp. 1367–1374. Available from DOI: 10.1039/C3CY20830C.

[66] STREL'TSOV, IA; VINOKUROVA, OB; TOKAREVA, IV; MISHAKOV, IV; ISUPOV, VP; SHUBIN, Yu V; VEDYAGIN, AA. Effect of the nature of a textural promoter on the catalytic properties of a nickel-copper catalyst for hydrocarbon processing in the production of carbon nanofibers. *Catalysis in industry.* 2014, vol. 6, no. 3, pp. 176–181. Available from DOI: 10.1134/S2070050414030131.

[67] ISHIDA, Tamao; KINOSHITA, Naoto; OKATSU, Hiroko; AKITA, Tomoki; TAKEI, Takashi; HARUTA, Masatake. Influence of the support and the size of gold clusters on catalytic activity for glucose oxidation. *Angewandte Chemie.* 2008, vol. 120, no. 48, pp. 9405–9408. Available from DOI: 10.1002/ange.200802845.

[68] LEDOUX, Marc J; PHAM-HUU, Cuong. Silicon carbide: a novel catalyst support for heterogeneous catalysis. *Cattech.* 2001, vol. 5, no. 4, pp. 226–246. Available from DOI: 10.1023/A:1014092930183.

[69] AL-FATESH, Ahmed S; NAEEM, Muhammad A; FAKEEHA, Anis H; ABASAEED, Ahmed E. Role of La2O3 as promoter and support in Ni/γ-Al2O3 catalysts for dry reforming of methane. *Chinese Journal of Chemical Engineering*. 2014, vol. 22, no. 1, pp. 28–37. Available from DOI: `10.1016/S1004-9541(14)60029-X`.

[70] VENKATESHAIAH, Abhilash; SILVESTRI, Daniele; RAMAKRISHNAN, Rohith K; WACŁAWEK, Stanislaw; PADIL, Vinod VT; ČERNÍK, Miroslav; VARMA, Rajender S. Gum kondagoagu/reduced graphene oxide framed platinum nanoparticles and their catalytic role. *Molecules*. 2019, vol. 24, no. 20, pp. 3643. Available from DOI: `10.3390/molecules24203643`.

[71] GUL, Saima; REHAN, Zulfiqar Ahmad; KHAN, Shahid Ali; AKHTAR, Kalsoom; KHAN, Murad Ali; KHAN, MI; RASHID, Muhammad Imtiaz; ASIRI, Abdullah M; KHAN, Sher Bahadar. Antibacterial PES-CA-Ag2O nanocomposite supported Cu nanoparticles membrane toward ultrafiltration, BSA rejection and reduction of nitrophenol. *Journal of Molecular Liquids*. 2017, vol. 230, pp. 616–624. Available from DOI: `10.1016/j.molliq.2016.12.093`.

[72] SPAIN, Jim C. Biodegradation of nitroaromatic compounds. *Annual review of microbiology*. 1995, vol. 49, no. 1, pp. 523–555. Available from DOI: `10.1146/annurev.mi.49.100195.002515`.

[73] ISMAIL, Muhammad; KHAN, MI; KHAN, Sher Bahadar; AKHTAR, Kalsoom; KHAN, Murad Ali; ASIRI, Abdullah M. Catalytic reduction of picric acid, nitrophenols and organic azo dyes via green synthesized plant supported Ag nanoparticles. *Journal of Molecular Liquids*. 2018, vol. 268, pp. 87–101. Available from DOI: `10.1016/j.molliq.2018.07.030`.

[74] XIONG, Zhaokun; ZHANG, Heng; ZHANG, Wenchao; LAI, Bo; YAO, Gang. Removal of nitrophenols and their derivatives by chemical redox: A review. *Chemical Engineering Journal*. 2019, vol. 359, pp. 13–31. Available from DOI: `10.1016/j.cej.2018.11.111`.

[75] KOIZUMI, Mutsuko; YAMAMOTO, Yuzuru; ITO, Yoshihiko; TAKANO, Masao; ENAMI, Tomonori; KAMATA, Eiichi; HASEGAWA, Ryuichi. Comparative study of toxicity of 4-nitrophenol and 2, 4-dinitrophenol in newborn and young rats. *The Journal of toxicological sciences*. 2001, vol. 26, no. 5, pp. 299–311. Available from DOI: `10.2131/jts.26.299`.

[76] KHAN, Farman Ullah; KHAN, Sher Bahadar; KAMAL, Tahseen; ASIRI, Abdullah M; KHAN, Ihsan Ullah; AKHTAR, Kalsoom, et al. Novel combination of zero-valent Cu and Ag nanoparticles@ cellulose acetate nanocomposite for the reduction of 4-nitro phenol. *International journal of biological macromolecules*. 2017, vol. 102, pp. 868–877. Available from DOI: `10.1016/j.ijbiomac.2017.04.062`.

[77] GUPTA, Vinod Kumar; YOLA, Mehmet Lütfi; EREN, Tanju; KARTAL, Fatma; ÇAĞLAYAN, Mustafa Oğuzhan; ATAR, Necip. Catalytic activity of Fe@ Ag nanoparticle involved calcium alginate beads for the reduction of nitrophenols. *Journal of Molecular Liquids*. 2014, vol. 190, pp. 133–138. Available from DOI: `10.1016/j.molliq.2013.10.022`.

[78] LI, Ning; ZHANG, Fuhua; WANG, Hua; HOU, Shifeng. Catalytic degradation of 4-nitrophenol in polluted water by three-dimensional gold nanoparticles/reduced graphene oxide microspheres. *Engineered Science*. 2019, vol. 7, no. 2, pp. 72–79. Available from DOI: `10.30919/es8d509`.

[79] FERRANDO, Riccardo; JELLINEK, Julius; JOHNSTON, Roy L. Nanoalloys: from theory to applications of alloy clusters and nanoparticles. *Chemical reviews*. 2008, vol. 108, no. 3, pp. 845–910. Available from DOI: `10.1021/cr040090g`.

[80] GUISBIERS, G; MENDOZA-PÉREZ, R; BAZÁN-DÍAZ, L; MENDOZA-CRUZ, R; VELÁZQUEZ-SALAZAR, J Jesús; JOSÉ-YACAMÁN, M. Size and shape effects on the phase diagrams of nickel-based bimetallic nanoalloys. *The Journal of Physical Chemistry C*. 2017, vol. 121, no. 12, pp. 6930–6939. Available from DOI: `10.1021/acs.jpcc.6b09115`.

[81] SHAN, Shiyao; LUO, Jin; YANG, Lefu; ZHONG, Chuan-Jian. Nanoalloy catalysts: structural and catalytic properties. *Catalysis Science & Technology*. 2014, vol. 4, no. 10, pp. 3570–3588. Available from DOI: `10.1039/C4CY00469H`.

[82] ALLOYEAU, Damien; MOTTET, Christine; RICOLLEAU, Christian. *Nanoalloys: Synthesis, Structure and Properties*. Springer Science & Business Media, 2012. ISBN 978-1-4471-4014-6.

[83] ABDELSAYED, Victor; GLASPELL, Garry; NGUYEN, Minh; HOWE, James M; EL-SHALL, M Samy. Laser synthesis of bimetallic nanoalloys in the vapor and liquid phases and the magnetic properties of PdM and PtM nanoparticles (M= Fe, Co and Ni). *Faraday Discussions*. 2008, vol. 138, pp. 163–180. Available from DOI: `10.1039/B706067J`.

[84] ALEXANDER, Duncan TL; FORRER, Daniel; ROSSI, Enrico; LIDORIKIS, Elefterios; AGNOLI, Stefano; BERNASCONI, Gabriel D; BUTET, Jeremy; MARTIN, Olivier JF; AMENDOLA, Vincenzo. Electronic Structure-Dependent Surface Plasmon Resonance in Single Au–Fe Nanoalloys. *Nano letters*. 2019, vol. 19, no. 8, pp. 5754–5761. Available from DOI: `10.1021/acs.nanolett.9b02396`.

[85] TORRES-MENDIETA, Rafael; HAVELKA, Ondřej; URBÁNEK, Michal; CVEK, Martin; WACŁAWEK, Stanisław; PADIL, Vinod Vellora Thekkae; JAŠÍKOVÁ, Darina; KOTEK, Michal; ČERNÍK, Miroslav. Laser-assisted synthesis of Fe-Cu oxide nanocrystals. *Applied Surface Science*. 2019, vol. 469, pp. 1007–1015. Available from DOI: `10.1016/j.apsusc.2018.11.058`.

[86]   ANDREWS, Mark P; O'BRIEN, Sean C. Gas-phase" molecular alloys" of bulk immiscible elements: iron-silver (FexAgy). *The Journal of Physical Chemistry*. 1992, vol. 96, no. 21, pp. 8233–8241. Available from DOI: `10.1021/j100200a007`.

[87]   CHEN, Guozhu; DESINAN, Stefano; NECHACHE, Riad; ROSEI, Renzo; ROSEI, Federico; MA, Dongling. Bifunctional catalytic/magnetic Ni@ Ru core–shell nanoparticles. *Chemical Communications*. 2011, vol. 47, no. 22, pp. 6308–6310. Available from DOI: `10.1039/C1CC10619H`.

[88]   DEMARTIN, Francesco; BIANI, Fabrizia Fabrizi de; FEMONI, Cristina; IAPALUCCI, Maria Carmela; LONGONI, Giuliano; MACCHI, Piero; ZANELLO, Piero. Synthesis, Electrochemistry and Crystal Structure of the [Ni36Pt4 (CO) 45] 6- and [Ni37Pt4 (CO) 46] 6- Hexaanions. *Journal of Cluster Science*. 2001, vol. 12, no. 1, pp. 61–74. Available from DOI: `10.1023/A:1016614810894`.

[89]   AGUILERA-GRANJA, F; LONGO, RC; GALLEGO, LJ; VEGA, A. Structural and magnetic properties of X 12 Y (X, Y= Fe, Co, Ni, Ru, Rh, Pd, and Pt) nanoalloys. *The Journal of Chemical Physics*. 2010, vol. 132, no. 18, pp. 184507. Available from DOI: `10.1063/1.3427292`.

[90]   JOHNSTON, Roy L. Metal nanoparticles and nanoalloys. In: *Frontiers of Nanoscience*. Elsevier, 2012, vol. 3, pp. 1–42. Available from DOI: `10.1016/B978-0-08-096357-0.00006-6`.

[91]   JOHNY, Jacob et al. Multidimensional thermally-induced transformation of nest-structured complex Au-Fe nanoalloys towards equilibrium. *arXiv preprint arXiv:2104.13491*. 2021.

[92]   LEPPERT, Linn; KEMPE, Rhett; KÜMMEL, Stephan. Hydrogen binding energies and electronic structure of Ni–Pd particles: a clue to their special catalytic properties. *Physical Chemistry Chemical Physics*. 2015, vol. 17, no. 39, pp. 26140–26148. Available from DOI: `10.1039/C5CP04174K`.

[93]   WALLACE, Philip Richard. The band theory of graphite. *Physical review*. 1947, vol. 71, no. 9, pp. 622. Available from DOI: `10.1103/PhysRev.71.622`.

[94]   BOEHM, HP; SETTON, R; STUMPP, E. Nomenclature and terminology of graphite intercalation compounds. *Pure and Applied Chemistry*. 1986, vol. 66, no. 9. Available from DOI: `10.1016/0008-6223(86)90126-0`.

[95]   GEIM, Andre K; NOVOSELOV, Konstantin S. The rise of graphene. In: *Nanoscience and technology: a collection of reviews from nature journals*. World Scientific, 2010, pp. 11–19. Available from DOI: `10.1038/nmat1849`.

[96]   MERMIN, N David; WAGNER, Herbert. Absence of ferromagnetism or anti-ferromagnetism in one-or two-dimensional isotropic Heisenberg models. *Physical Review Letters*. 1966, vol. 17, no. 22, pp. 1133. Available from DOI: `10.1103/PhysRevLett.17.1133`.

[97] MEYER, Jannik C; GEIM, Andre K; KATSNELSON, Mikhail I; NOVOSELOV, Konstantin S; BOOTH, Tim J; ROTH, Siegmar. The structure of suspended graphene sheets. *Nature*. 2007, vol. 446, no. 7131, pp. 60–63. Available from DOI: `10.1038/nature05545`.

[98] NOVOSELOV, Kostya S; JIANG, D; SCHEDIN, F; BOOTH, TJ; KHOTKEVICH, VV; MOROZOV, SV; GEIM, Andre K. Two-dimensional atomic crystals. *Proceedings of the National Academy of Sciences*. 2005, vol. 102, no. 30, pp. 10451–10453. Available from DOI: `10.1073/pnas.0502848102`.

[99] BROWNSON, Dale AC; KAMPOURIS, Dimitrios K; BANKS, Craig E. Graphene electrochemistry: fundamental concepts through to prominent applications. *Chemical Society Reviews*. 2012, vol. 41, no. 21, pp. 6944–6976. Available from DOI: `10.1039/C2CS35105F`.

[100] BALANDIN, Alexander A; GHOSH, Suchismita; BAO, Wenzhong; CALIZO, Irene; TEWELDEBRHAN, Desalegne; MIAO, Feng; LAU, Chun Ning. Superior thermal conductivity of single-layer graphene. *Nano letters*. 2008, vol. 8, no. 3, pp. 902–907. Available from DOI: `10.1021/nl0731872`.

[101] LEE, Changgu; WEI, Xiaoding; KYSAR, Jeffrey W; HONE, James. Measurement of the elastic properties and intrinsic strength of monolayer graphene. *science*. 2008, vol. 321, no. 5887, pp. 385–388. Available from DOI: `10.1126/science.1157996`.

[102] ZHU, Yanwu; MURALI, Shanthi; CAI, Weiwei; LI, Xuesong; SUK, Ji Won; POTTS, Jeffrey R; RUOFF, Rodney S. Graphene and graphene oxide: synthesis, properties, and applications. *Advanced materials*. 2010, vol. 22, no. 35, pp. 3906–3924. Available from DOI: `10.1002/adma.201001068`.

[103] NOVOSELOV, Kostya S; GEIM, Andre K; MOROZOV, Sergei V; JIANG, D; ZHANG, Y_; DUBONOS, Sergey V; GRIGORIEVA, Irina V; FIRSOV, Alexandr A. Electric field effect in atomically thin carbon films. *science*. 2004, vol. 306, no. 5696, pp. 666–669. Available from DOI: `10.1126/science.1102896`.

[104] DE SILVA, KKH; HUANG, H-H; JOSHI, RK; YOSHIMURA, M. Chemical reduction of graphene oxide using green reductants. *Carbon*. 2017, vol. 119, pp. 190–199. Available from DOI: `10.1016/j.carbon.2017.04.025`.

[105] LEE, Xin Jiat; HIEW, Billie Yan Zhang; LAI, Kar Chiew; LEE, Lai Yee; GAN, Suyin; THANGALAZHY-GOPAKUMAR, Suchithra; RIGBY, Sean. Review on graphene and its derivatives: Synthesis methods and potential industrial implementation. *Journal of the Taiwan Institute of Chemical Engineers*. 2019, vol. 98, pp. 163–180. Available from DOI: `10.1016/j.jtice.2018.10.028`.

[106] PRIMO, Ana; NEATU, Florentina; FLOREA, Mihaela; PARVULESCU, Vasile; GARCIA, Hermenegildo. Graphenes in the absence of metals as carbocatalysts for selective acetylene hydrogenation and alkene hydrogenation. *Nature communications.* 2014, vol. 5, no. 1, pp. 1–9. Available from DOI: 10.1038/ncomms6291.

[107] AMBROSI, Adriano; BONANNI, Alessandra; SOFER, Zdeněk; CROSS, Jeffrey S; PUMERA, Martin. Electrochemistry at chemically modified graphenes. *Chemistry–A European Journal.* 2011, vol. 17, no. 38, pp. 10763–10770. Available from DOI: 10.1002/chem.201101117.

[108] LIN, Wei-Jhih; LIAO, Chien-Shiun; JHANG, Jia-Hao; TSAI, Yu-Chen. Graphene modified basal and edge plane pyrolytic graphite electrodes for electrocatalytic oxidation of hydrogen peroxide and β-nicotinamide adenine dinucleotide. *Electrochemistry Communications.* 2009, vol. 11, no. 11, pp. 2153–2156. Available from DOI: 10.1016/j.elecom.2009.09.018.

[109] YUAN, Wenjing; ZHOU, Yu; LI, Yingru; LI, Chun; PENG, Hailin; ZHANG, Jin; LIU, Zhongfan; DAI, Liming; SHI, Gaoquan. The edge-and basal-plane-specific electrochemistry of a single-layer graphene sheet. *Scientific reports.* 2013, vol. 3, no. 1, pp. 1–7. Available from DOI: 10.1038/srep02248.

[110] RANDVIIR, Edward P; BROWNSON, Dale AC; BANKS, Craig E. A decade of graphene research: production, applications and outlook. *Materials Today.* 2014, vol. 17, no. 9, pp. 426–432. Available from DOI: 10.1016/j.mattod.2014.06.001.

[111] HU, Maocong; YAO, Zhenhua; WANG, Xianqin. Graphene-based nanomaterials for catalysis. *Industrial & Engineering Chemistry Research.* 2017, vol. 56, no. 13, pp. 3477–3502. Available from DOI: 10.1021/acs.iecr.6b05048.

[112] HU, Leibo; HU, Xianru; WU, Xuebin; DU, Chenlei; DAI, Yunchuan; DENG, Jianbo. Density functional calculation of transition metal adatom adsorption on graphene. *Physica B: Condensed Matter.* 2010, vol. 405, no. 16, pp. 3337–3341. Available from DOI: 10.1016/j.physb.2010.05.001.

[113] HUMMERS JR, William S; OFFEMAN, Richard E. Preparation of graphitic oxide. *Journal of the american chemical society.* 1958, vol. 80, no. 6, pp. 1339–1339. Available from DOI: 10.1021/ja01539a017.

[114] ACIK, M; LEE, Geunsik; MATTEVI, C; CHHOWALLA, Manishkumar; CHO, K; CHABAL, YJ. Unusual infrared-absorption mechanism in thermally reduced graphene oxide. *Nature materials.* 2010, vol. 9, no. 10, pp. 840–845. Available from DOI: 10.1038/nmat2858.

[115] GÓMEZ-NAVARRO, Cristina; WEITZ, R Thomas; BITTNER, Alexander M; SCOLARI, Matteo; MEWS, Alf; BURGHARD, Marko; KERN, Klaus. Electronic transport properties of individual chemically reduced graphene oxide sheets. *Nano letters.* 2007, vol. 7, no. 11, pp. 3499–3503. Available from DOI: 10.1021/nl072090c.

[116] TUNG, Vincent C; ALLEN, Matthew J; YANG, Yang; KANER, Richard B. High-throughput solution processing of large-scale graphene. *Nature nanotechnology*. 2009, vol. 4, no. 1, pp. 25. Available from DOI: 10.1038/nnano.2008.329.

[117] CHUA, Chun Kiang; PUMERA, Martin. Chemical reduction of graphene oxide: a synthetic chemistry viewpoint. *Chemical Society Reviews*. 2014, vol. 43, no. 1, pp. 291–312. Available from DOI: 10.1039/C3CS60303B.

[118] HUANG, Lei; LIU, Yang; JI, Le-Chun; XIE, Yi-Qun; WANG, Tao; SHI, Wang-Zhou. Pulsed laser assisted reduction of graphene oxide. *Carbon*. 2011, vol. 49, no. 7, pp. 2431–2436. Available from DOI: 10.1016/j.carbon.2011.01.067.

[119] LOTYA, Mustafa; KING, Paul J; KHAN, Umar; DE, Sukanta; COLEMAN, Jonathan N. High-concentration, surfactant-stabilized graphene dispersions. *ACS nano*. 2010, vol. 4, no. 6, pp. 3155–3162. Available from DOI: 10.1021/nn1005304.

[120] GARAJ, Slaven; HUBBARD, William; GOLOVCHENKO, Jene Andrew. Graphene synthesis by ion implantation. *Applied physics letters*. 2010, vol. 97, no. 18, pp. 183103. Available from DOI: 10.1063/1.3507287.

[121] ARISTOV, Victor Yu et al. Graphene synthesis on cubic SiC/Si wafers. Perspectives for mass production of graphene-based electronic devices. *Nano letters*. 2010, vol. 10, no. 3, pp. 992–995. Available from DOI: 10.1021/nl904115h.

[122] BAE, Sukang et al. Roll-to-roll production of 30-inch graphene films for transparent electrodes. *Nature nanotechnology*. 2010, vol. 5, no. 8, pp. 574. Available from DOI: 10.1038/nnano.2010.132.

[123] LEE, Gwan-Hyoung et al. High-strength chemical-vapor–deposited graphene and grain boundaries. *science*. 2013, vol. 340, no. 6136, pp. 1073–1076. Available from DOI: 10.1126/science.1235126.

[124] LI, Xuesong et al. Large-area synthesis of high-quality and uniform graphene films on copper foils. *science*. 2009, vol. 324, no. 5932, pp. 1312–1314. Available from DOI: 10.1126/science.1171245.

[125] HYUN, Woo Jin; PARK, O Ok; CHIN, Byung Doo. Foldable graphene electronic circuits based on paper substrates. *Advanced Materials*. 2013, vol. 25, no. 34, pp. 4729–4734. Available from DOI: 10.1002/adma.201302063.

[126] HERNANDEZ, Yenny et al. High-yield production of graphene by liquid-phase exfoliation of graphite. *Nature nanotechnology*. 2008, vol. 3, no. 9, pp. 563–568. Available from DOI: 10.1038/nnano.2008.215.

[127] PATON, Keith R et al. Scalable production of large quantities of defect-free few-layer graphene by shear exfoliation in liquids. *Nature materials*. 2014, vol. 13, no. 6, pp. 624–630. Available from DOI: 10.1038/nmat3944.

[128] CHANDRASHEKAR, Bananakere Nanjegowda; DENG, Bing; SMITHA, Ankanahalli Shankaregowda; CHEN, Yubin; TAN, Congwei; ZHANG, Haixia; PENG, Hailin; LIU, Zhongfan. Roll-to-roll green transfer of CVD graphene onto plastic for a transparent and flexible triboelectric nanogenerator. *Advanced materials*. 2015, vol. 27, no. 35, pp. 5210–5216. Available from DOI: 10.1002/adma.201502560.

[129] AUFFAN, Mélanie; ROSE, Jerome; BOTTERO, Jean-Yves; LOWRY, Gregory V; JOLIVET, Jean-Pierre; WIESNER, Mark R. Towards a definition of inorganic nanoparticles from an environmental, health and safety perspective. *Nature Nanotechnology*. 2009, vol. 4, no. 10, pp. 634. Available from DOI: 10.1038/nnano.2009.242.

[130] KREYLING, Wolfgang G; SEMMLER-BEHNKE, Manuela; CHAUDHRY, Qasim. A complementary definition of nanomaterial. *Nano today*. 2010, vol. 5, no. 3, pp. 165–168. Available from DOI: 10.1016/j.nantod.2010.03.004.

[131] PARVEEN, Khadeeja; BANSE, Viktoria; LEDWANI, Lalita. Green synthesis of nanoparticles: their advantages and disadvantages. In: *AIP conference proceedings*. 2016, vol. 1724, p. 020048. No. 1. Available from DOI: 10.1063/1.4945168.

[132] HRISTOZOV, Danail; MALSCH, Ineke. Hazards and risks of engineered nanoparticles for the environment and human health. *Sustainability*. 2009, vol. 1, no. 4, pp. 1161–1194. Available from DOI: 10.3390/su1041161.

[133] THIRUVENGADATHAN, Rajagopalan; KORAMPALLY, Venumadhav; GHOSH, Arkasubhra; CHANDA, Nripen; GANGOPADHYAY, Keshab; GANGOPADHYAY, Shubhra. Nanomaterial processing using self-assembly-bottom-up chemical and biological approaches. *Reports on Progress in Physics*. 2013, vol. 76, no. 6, pp. 066501. Available from DOI: 10.1088/0034-4885/76/6/066501.

[134] NIKAM, AV; PRASAD, BLV; KULKARNI, AA. Wet chemical synthesis of metal oxide nanoparticles: a review. *CrystEngComm*. 2018, vol. 20, no. 35, pp. 5091–5107. Available from DOI: 10.1039/C8CE00487K.

[135] ZIEFUß, Anna R; REICHENBERGER, Sven; REHBOCK, Christoph; CHAKRABORTY, Indranath; GHARIB, Mustafa; PARAK, Wolfgang J; BARCIKOWSKI, Stephan. Laser fragmentation of colloidal gold nanoparticles with high-intensity nanosecond pulses is driven by a single-step fragmentation mechanism with a defined educt particle-size threshold. *The Journal of Physical Chemistry C*. 2018, vol. 122, no. 38, pp. 22125–22136. Available from DOI: 10.1021/acs.jpcc.8b04374.

[136] PATIL, PP; PHASE, DM; KULKARNI, SA; GHAISAS, SV; KULKARNI, SK; KANETKAR, SM; OGALE, SB; BHIDE, VG. Pulsed-laser–induced reactive quenching at liquid-solid interface: Aqueous oxidation of iron. *Physical review letters*. 1987, vol. 58, no. 3, pp. 238. Available from DOI: 10.1103/PhysRevLett.58.238.

[137] FOJTIK, Anton; HENGLEIN, Arnim. Laser ablation of films and suspended particles in a solvent: formation of cluster and colloid solutions. *Berichte der Bunsen-Gesellschaft.* 1993, vol. 97, no. 2, pp. 252–254.

[138] AMANS, David; CAI, Weiping; BARCIKOWSKI, Stephan. *Status and demand of research to bring laser generation of nanoparticles in liquids to maturity.* Elsevier, 2019. Available from DOI: `10.1016/j.apsusc.2019.05.117`.

[139] LETZEL, Alexander et al. Time and Mechanism of Nanoparticle Functionalization by Macromolecular Ligands during Pulsed Laser Ablation in Liquids. *Langmuir.* 2019, vol. 35, no. 8, pp. 3038–3047. Available from DOI: `10.1021/acs.langmuir.8b01585`.

[140] JENDRZEJ, Sandra; GÖKCE, Bilal; EPPLE, Matthias; BARCIKOWSKI, Stephan. How Size Determines the Value of Gold: Economic Aspects of Wet Chemical and Laser-Based Metal Colloid Synthesis. *ChemPhysChem.* 2017, vol. 18, no. 9, pp. 1012–1019. Available from DOI: `10.1002/cphc.201601139`.

[141] CRIVELLARO, Simone; GUADAGNINI, Andrea; ARBOLEDA, David Muñetón; SCHINCA, Daniel; AMENDOLA, Vincenzo. A system for the synthesis of nanoparticles by laser ablation in liquid that is remotely controlled with PC or smartphone. *Review of Scientific Instruments.* 2019, vol. 90, no. 3, pp. 033902. Available from DOI: `10.1063/1.5083811`.

[142] SHELDON, Roger A. Fundamentals of green chemistry: efficiency in reaction design. *Chemical Society Reviews.* 2012, vol. 41, no. 4, pp. 1437–1451. Available from DOI: `10.1039/C1CS15219J`.

[143] STREUBEL, René; BARCIKOWSKI, Stephan; GÖKCE, Bilal. Continuous multigram nanoparticle synthesis by high-power, high-repetition-rate ultrafast laser ablation in liquids. *Optics letters.* 2016, vol. 41, no. 7, pp. 1486–1489. Available from DOI: `10.1364/OL.41.001486`.

[144] IONIN, Andrey et al. Milligram-per-second femtosecond laser production of Se nanoparticle inks and ink-jet printing of nanophotonic 2D-patterns. *Applied Surface Science.* 2018, vol. 436, pp. 662–669. Available from DOI: `10.1016/j.apsusc.2017.12.057`.

[145] NADARAJAH, Ruksan; BARCIKOWSKI, Stephan; GÖKCE, Bilal. Picosecond laser-induced surface structures on alloys in liquids and their influence on nanoparticle productivity during laser ablation. *Optics express.* 2020, vol. 28, no. 3, pp. 2909–2924. Available from DOI: `10.1364/OE.28.002909`.

[146] KALUS, Mark-Robert; BÄRSCH, Niko; STREUBEL, René; GÖKCE, Emine; BARCIKOWSKI, Stephan; GÖKCE, Bilal. How persistent microbubbles shield nanoparticle productivity in laser synthesis of colloids–quantification of their volume, dwell dynamics, and gas composition. *Physical Chemistry Chemical Physics.* 2017, vol. 19, no. 10, pp. 7112–7123. Available from DOI: `10.1039/C6CP07011F`.

[147] BARCIKOWSKI, Stephan; AMENDOLA, Vincenzo; MARZUN, Galina; REHBOCK, Christoph; REICHENBERGER, Sven; ZHANG, Dongshi; GÖKCE, Bilal. Handbook of laser synthesis of colloids - second edition. 2019. Available from DOI: `10.17185/duepublico/70584`.

[148] KALUS, Mark-Robert; BARCIKOWSKI, Stephan; GÖKCE, Bilal. How the Physicochemical Properties of the Bulk Material Affect the Ablation Crater Profile, Mass Balance, and Bubble Dynamics During Single-Pulse, Nanosecond Laser Ablation in Water. *Chemistry (Weinheim an der Bergstrasse, Germany)*. 2021, vol. 27, no. 19, pp. 5978. Available from DOI: `10.1002/chem.202005087`.

[149] SHIH, Cheng-Yu et al. Two mechanisms of nanoparticle generation in picosecond laser ablation in liquids: The origin of the bimodal size distribution. *Nanoscale*. 2018, vol. 10, no. 15, pp. 6900–6910. Available from DOI: `10.1039/C7NR08614H`.

[150] AMENDOLA, Vincenzo; AMANS, Ing David; ISHIKAWA, Yoshie; KOSHIZAKI, Naoto; SCIRÈ, Salvatore; COMPAGNINI, Giuseppe; REICHENBERGER, Sven; BARCIKOWSKI, Ing Stephan. Room-Temperature Laser Synthesis in Liquid of Oxide, Metal-Oxide Core-Shells, and Doped Oxide Nanoparticles. *Chemistry (Weinheim an der Bergstrasse, Germany)*. 2020, vol. 26, no. 42, pp. 9206. Available from DOI: `10.1002/chem.202000686`.

[151] MAURER, Michael J. Relaxation Model for Heat Conduction in Metals. *Journal of Applied Physics*. 1969, vol. 40, no. 13, pp. 5123–5130. Available from DOI: `10.1063/1.1657362`.

[152] TORRES-MENDIETA, R; YALCINKAYA, Fatma; BOYRAZ, Evren; HAVELKA, Ondřej; WACŁAWEK, S; MARYŠKA, Jiří; ČERNÍK, Miroslav; BRYJAK, Marek. PVDF nanofibrous membranes modified via laser-synthesized Ag nanoparticles for a cleaner oily water separation. *Applied Surface Science*. 2020, vol. 526, pp. 146575. Available from DOI: `10.1016/j.apsusc.2020.146575`.

[153] TORRESAN, Veronica et al. 4D Multimodal Nanomedicines Made of Nonequilibrium Au–Fe Alloy Nanoparticles. *ACS nano*. 2020, vol. 14, no. 10, pp. 12840–12853. Available from DOI: `10.1021/acsnano.0c03614`.

[154] TORRESAN, Veronica et al. Biocompatible Iron–Boron Nanoparticles Designed for Neutron Capture Therapy Guided by Magnetic Resonance Imaging. *Advanced Healthcare Materials*. 2021, vol. 10, no. 6, pp. 1–11. Available from DOI: `10.1002/adhm.202001632`.

[155] JOHNY, Jacob et al. Formation of Co–Au Core–Shell Nanoparticles with Thin Gold Shells and Soft Magnetic ε-Cobalt Cores Ruled by Thermodynamics and Kinetics. *The Journal of Physical Chemistry C*. 2021, vol. 125, no. 17, pp. 9534–9549. Available from DOI: `10.1021/acs.jpcc.1c02138`.

[156] WAAG, Friedrich; STREUBEL, René; GÖKCE, Bilal; BARCIKOWSKI, Stephan. Synthesis of gold, platinum, and gold-platinum alloy nanoparticle colloids with high-power megahertz-repetition-rate lasers: the importance of the beam guidance method. *Applied Nanoscience*. 2021, vol. 11, no. 4, pp. 1303–1312. Available from DOI: `10.1007/s13204-021-01693-y`.

[157] JOHN, Mallory G; TIBBETTS, Katharine Moore. One-step femtosecond laser ablation synthesis of sub-3 nm gold nanoparticles stabilized by silica. *Applied Surface Science*. 2019, vol. 475, pp. 1048–1057. Available from DOI: `10.1016/j.apsusc.2019.01.042`.

[158] ETTEL, David; HAVELKA, Ondřej; ISIK, Selingül; YALCINKAYA, Fatma; TORRES, Mendieta Rafael Omar. EXPANSION OF OPTICAL PROPERTIES IN TIOX NANOPARTICLES BY THEIR LASER-MEDIATED ALLOYING WITH AG. In: *Proceedings 12th International Conference on Nanomaterials-Research & Application NANOCON 2020*. 2020, pp. 109–115. Available from DOI: `10.37904/nanocon.2020.3700`.

[159] JIMENEZ, Ernesto; ABDERRAFI, Kamal; ABARGUES, Rafael; VALDES, Jose L; MARTINEZ-PASTOR, Juan P. Laser-ablation-induced synthesis of SiO2-capped noble metal nanoparticles in a single step. *Langmuir*. 2010, vol. 26, no. 10, pp. 7458–7463. Available from DOI: `10.1021/la904179x`.

[160] LIU, Pu; CHEN, Huanjun; WANG, Hao; YAN, Jiahao; LIN, Zhaoyong; YANG, Guowei. Fabrication of Si/Au core/shell nanoplasmonic structures with ultrasensitive surface-enhanced Raman scattering for monolayer molecule detection. *The Journal of Physical Chemistry C*. 2015, vol. 119, no. 2, pp. 1234–1246. Available from DOI: `10.1021/jp5111482`.

[161] ERMAKOV, Victor A; JIMENEZ-VILLAR, Ernesto; SILVA FILHO, José Maria Clemente da; YASSITEPE, Emre; MOGILI, Naga Vishnu Vardhan; IIKAWA, Fernando; SÁ, Gilberto Fernandes de; CESAR, Carlos Lenz; MARQUES, Francisco Chagas. Size control of silver-core/silica-shell nanoparticles fabricated by laser-ablation-assisted chemical reduction. *Langmuir*. 2017, vol. 33, no. 9, pp. 2257–2262. Available from DOI: `10.1021/acs.langmuir.6b04308`.

[162] SARAEVA, Irina Nikolaevna et al. Laser synthesis of colloidal Si@ Au and Si@ Ag nanoparticles in water via plasma-assisted reduction. *Journal of Photochemistry and Photobiology A: Chemistry*. 2018, vol. 360, pp. 125–131. Available from DOI: `10.1016/j.jphotochem.2018.04.004`.

[163] HU, Sheng; MELTON, Chad; MUKHERJEE, Dibyendu. A facile route for the synthesis of nanostructured oxides and hydroxides of cobalt using laser ablation synthesis in solution (LASIS). *Physical Chemistry Chemical Physics*. 2014, vol. 16, no. 43, pp. 24034–24044. Available from DOI: `10.1039/C4CP03018D`.

[164] HAVELKA, Ondrej. Laser-mediated synthesis of iron nanoclusters. *Liberec: Technical University of Liberec, Institute for Nanomaterials, Advanced Technologies and Innovation*. Bachelor thesis, 2019.

[165]   *Javascript Mie scattering calculator* [https://saviot.cnrs.fr/miecoat/index.en.html]. Accessed: 2021-05-06.

[166]   DEGUELDRE, C; FAVARGER, P-Y; BITEA, C. Zirconia colloid analysis by single particle inductively coupled plasma–mass spectrometry. *Analytica Chimica Acta.* 2004, vol. 518, no. 1-2, pp. 137–142. Available from DOI: 10.1016/j.aca.2004.04.015.

[167]   SHIRSATH, Sagar E; JADHAV, Santosh S; TOKSHA, BG; PATANGE, SM; JADHAV, KM. Influence of Ce4+ ions on the structural and magnetic properties of NiFe2O4. *Journal of Applied Physics.* 2011, vol. 110, no. 1, pp. 013914. Available from DOI: 10.1063/1.3603004.

[168]   BOCCACCINI, Aldo R; BIEST, Omer van der; TALBOT, Jan B. Electrophoretic Deposition, Fundamentals and Applications: Proceedings of the International Symposium. In: 2002. ISBN 1-56677-345-8.

[169]   DERRICK, Michele R; STULIK, Dusan; LANDRY, James M. *Infrared spectroscopy in conservation science.* Getty Publications, 2000. ISBN 978-0-89236-469-5.

[170]   METWALLY, Khaled; MENSAH, Serge; BAFFOU, Guillaume. Fluence threshold for photothermal bubble generation using plasmonic nanoparticles. *The Journal of Physical Chemistry C.* 2015, vol. 119, no. 51, pp. 28586–28596. Available from DOI: 10.1021/acs.jpcc.5b09903.

[171]   SILVESTRI, Daniele; WACŁAWEK, Stanisław; VENKATESHAIAH, Abhilash; KRAWCZYK, Kamil; SOBEL, Bartłomiej; PADIL, Vinod VT; ČERNÍK, Miroslav; VARMA, Rajender S. Synthesis of Ag nanoparticles by a chitosan-poly (3-hydroxybutyrate) polymer conjugate and their superb catalytic activity. *Carbohydrate polymers.* 2020, vol. 232, pp. 115806. Available from DOI: 10.1016/j.carbpol.2019.115806.

[172]   WANG, Xue et al. Pd@ Pt core–shell concave decahedra: a class of catalysts for the oxygen reduction reaction with enhanced activity and durability. *Journal of the American Chemical Society.* 2015, vol. 137, no. 47, pp. 15036–15042. Available from DOI: 10.1021/jacs.5b10059.

[173]   NARAYANAN, Kannan Badri; SAKTHIVEL, Natarajan. Synthesis and characterization of nano-gold composite using Cylindrocladium floridanum and its heterogeneous catalysis in the degradation of 4-nitrophenol. *Journal of hazardous materials.* 2011, vol. 189, no. 1-2, pp. 519–525. Available from DOI: 10.1016/j.jhazmat.2011.02.069.

[174]   LARA, Luciano RS; ZOTTIS, Alexandre D; ELIAS, Welman C; FAGGION, Deonildo; CAMPOS, Carlos Eduardo Maduro de; ACUÑA, Jose Javier S; DOMINGOS, Josiel B. The catalytic evaluation of in situ grown Pd nanoparticles on the surface of Fe 3 O 4@ dextran particles in the p-nitrophenol reduction reaction. *RSC Advances.* 2015, vol. 5, no. 11, pp. 8289–8296. Available from DOI: 10.1039/C4RA16440G.

[175] KÄSTNER, Claudia; THÜNEMANN, Andreas F. Catalytic reduction of 4-nitrophenol using silver nanoparticles with adjustable activity. *Langmuir.* 2016, vol. 32, no. 29, pp. 7383–7391. Available from DOI: `10.1021/acs.langmuir.6b01477`.

[176] PARK, Sungjin; AN, Jinho; POTTS, Jeffrey R; VELAMAKANNI, Aruna; MURALI, Shanthi; RUOFF, Rodney S. Hydrazine-reduction of graphite-and graphene oxide. *Carbon.* 2011, vol. 49, no. 9, pp. 3019–3023. Available from DOI: `10.1016/j.carbon.2011.02.071`.

[177] ZHANG, Xiaorui; OOKI, Wataru; KOSAKA, Yoshinori R; OKONOGI, Akinori; MARZUN, Galina; WAGENER, Philipp; BARCIKOWSKI, Stephan; KONDO, Takahiro; NAKAMURA, Junji. Effect of pH on the spontaneous synthesis of palladium nanoparticles on reduced graphene oxide. *Applied Surface Science.* 2016, vol. 389, pp. 911–915. Available from DOI: `10.1016/j.apsusc.2016.08.014`.

[178] KANITZ, A; KALUS, MR; GUREVICH, EL; OSTENDORF, A; BARCIKOWSKI, S; AMANS, David. Review on experimental and theoretical investigations of the early stage, femtoseconds to microseconds processes during laser ablation in liquid-phase for the synthesis of colloidal nanoparticles. *Plasma Sources Science and Technology.* 2019, vol. 28, no. 10, pp. 103001. Available from DOI: `10.1088/1361-6595/ab3dbe`.

[179] D'ADDATO, Sergio; GRILLO, V; ALTIERI, Salvatore; TONDI, R; VALERI, Sergio; FRABBONI, Stefano. Structure and stability of nickel/nickel oxide core–shell nanoparticles. *Journal of Physics: Condensed Matter.* 2011, vol. 23, no. 17, pp. 175003. Available from DOI: `10.1088/0953-8984/23/17/175003`.

[180] NAYAK, Bibhuti B; VITTA, Satish; NIGAM, AK; BAHADUR, DHIRENDRA. Ni and Ni–nickel oxide nanoparticles with different shapes and a core–shell structure. *Thin Solid Films.* 2006, vol. 505, no. 1-2, pp. 109–112. Available from DOI: `10.1016/j.tsf.2005.10.018`.

[181] IMRAN, M; YOUSAF, Ammar B; ZHOU, Xiao; JIANG, Yi-Fan; YUAN, Cheng-Zong; ZEB, Akif; JIANG, Nan; XU, An-Wu. Pd/TiO nanocatalyst with strong metal–support interaction for highly efficient durable heterogeneous hydrogenation. *The Journal of Physical Chemistry C.* 2017, vol. 121, no. 2, pp. 1162–1170. Available from DOI: `10.1021/acs.jpcc.6b102741`.

[182] COMOTTI, Massimiliano; LI, Wen-Cui; SPLIETHOFF, Bernd; SCHÜTH, Ferdi. Support effect in high activity gold catalysts for CO oxidation. *Journal of the American Chemical Society.* 2006, vol. 128, no. 3, pp. 917–924. Available from DOI: `10.1021/ja0561441`.

[183] FIGUEIREDO, Wallace T; DELLA MEA, Guilherme B; SEGALA, Maximiliano; BAPTISTA, Daniel L; ESCUDERO, Carlos; PÉREZ-DIESTE, Virginia; BERNARDI, Fabiano. Understanding the Strong Metal–Support Interaction (SMSI) Effect in Cu x Ni1–x/CeO2 (0< x< 1) Nanoparticles for Enhanced Catalysis. *ACS Applied Nano Materials.* 2019, vol. 2, no. 4, pp. 2559–2573. Available from DOI: `10.1021/acsanm.9b00569`.

[184] CHEN, Xiaodong; MENG, Chao; WANG, Yong; ZHAO, Qianqian; LI, Yue-jiao; CHEN, Xue-Min; YANG, Dewang; LI, Yuxia; ZHOU, Yue. Laser-synthesized rutile TiO2 with abundant oxygen vacancies for enhanced solar water evaporation. *ACS Sustainable Chemistry & Engineering*. 2020, vol. 8, no. 2, pp. 1095–1101. Available from DOI: `10.1021/acssuschemeng.9b05952`.

[185] MITRANO, DM; RANVILLE, James F; BEDNAR, Anthony; KAZOR, Karen; HERING, Amanda S; HIGGINS, Christopher P. Tracking dissolution of silver nanoparticles at environmentally relevant concentrations in laboratory, natural, and processed waters using single particle ICP-MS (spICP-MS). *Environmental Science: Nano*. 2014, vol. 1, no. 3, pp. 248–259. Available from DOI: `10.1039/C3EN00108C`.

[186] REVATHY, TA; DHANAVEL, S; SIVARANJANI, T; NARAYANAN, V; MAIYALAGAN, T; STEPHEN, A. Highly active graphene-supported palladium-nickel alloy nanoparticles for catalytic reduction of 4-nitrophenol. *Applied Surface Science*. 2018, vol. 449, pp. 764–771. Available from DOI: `10.1016/j.apsusc.2018.01.280`.

[187] REVATHY, TA; DHANAPAL, K; DHANAVEL, S; NARAYANAN, V; STEPHEN, A. Pulsed electrodeposited dendritic Pd-Ni alloy as a magnetically recoverable nanocatalyst for the hydrogenation of 4-nitrophenol. *Journal of Alloys and Compounds*. 2018, vol. 735, pp. 1703–1711. Available from DOI: `10.1016/j.jallcom.2017.11.264`.

[188] KAUR, Navneet; SOOD, Akanksha; BHASIN, KK; KAUR, Gurpreet; BHALLA, Aman; DHAU, Jaspreet S; CHAUDHARY, Ganga Ram. Metallosurfactants derived Pd-NiO nanocomposite for remediation of nitrophenol in water. *Journal of Molecular Liquids*. 2019, vol. 288, pp. 111018. Available from DOI: `10.1016/j.molliq.2019.111018`.

[189] LEBASCHI, Sadaf; HEKMATI, Malak; VEISI, Hojat. Green synthesis of palladium nanoparticles mediated by black tea leaves (Camellia sinensis) extract: catalytic activity in the reduction of 4-nitrophenol and Suzuki-Miyaura coupling reaction under ligand-free conditions. *Journal of colloid and interface science*. 2017, vol. 485, pp. 223–231. Available from DOI: `10.1016/j.jcis.2016.09.027`.

[190] WANG, Chunxia; YANG, Fan; YANG, Wang; REN, Liang; ZHANG, Yunhan; JIA, Xilai; ZHANG, Liqiang; LI, Yongfeng. PdO nanoparticles enhancing the catalytic activity of Pd/carbon nanotubes for 4-nitrophenol reduction. *Rsc Advances*. 2015, vol. 5, no. 35, pp. 27526–27532. Available from DOI: `10.1039/C4RA16792A`.

[191] LIU, Teng; CUI, Zelin; LIU, Yang; BAI, Xuefeng. In-situ fabrication of ultrafine Pd supported on nitrogen-doped reduced graphene oxide via nitrogen glow discharge plasma for catalytic reduction of 4-Nitrophenol. *Applied Catalysis A: General*. 2019, vol. 588, pp. 117278. Available from DOI: `10.1016/j.apcata.2019.117278`.

[192] DONG, Wenhuan; CHENG, Saisai; FENG, Cheng; SHANG, Ningzhao; GAO, Shutao; WANG, Chun. Fabrication of highly dispersed Pd nanoparticles supported on reduced graphene oxide for catalytic reduction of 4-nitrophenol. *Catalysis Communications*. 2017, vol. 90, pp. 70–74. Available from DOI: 10.1016/j.catcom.2016.11.021.

[193] CAMPESI, R; PAUL-BONCOUR, V; CUEVAS, F; LEROY, E; GADIOU, R; VIX-GUTERL, C; LATROCHE, M. Structural and Magnetic Properties of Pd x Ni1- x (x= 0 and 0.54) Metallic Nanoparticles in an Ordered Mesoporous Carbon Template. *The Journal of Physical Chemistry C*. 2009, vol. 113, no. 39, pp. 16921–16926. Available from DOI: 10.1021/jp904453k.

[194] LIU, Lijun; CHEN, Ruifen; LIU, Weikai; WU, Jiamin; GAO, Di. Catalytic reduction of 4-nitrophenol over Ni-Pd nanodimers supported on nitrogen-doped reduced graphene oxide. *Journal of hazardous materials*. 2016, vol. 320, pp. 96–104. Available from DOI: 10.1016/j.jhazmat.2016.08.019.

[195] YADAV, Raghvendra Singh; KUŘITKA, Ivo; VILCAKOVA, Jarmila; HAVLICA, Jaromir; KALINA, Lukas; URBÁNEK, Pavel; MACHOVSKY, Michal; MASAŘ, Milan; HOLEK, Martin. Influence of La 3+ on structural, magnetic, dielectric, electrical and modulus spectroscopic characteristics of single phase CoFe 2- x La x O 4 nanoparticles. *Journal of Materials Science: Materials in Electronics*. 2017, vol. 28, no. 12, pp. 9139–9154. Available from DOI: 10.1007/s10854-017-6648-5.

[196] JALILI, Hajar; ASLIBEIKI, Bagher; VARZANEH, Ali Ghotbi; CHERNENKO, Volodymyr A. The effect of magneto-crystalline anisotropy on the properties of hard and soft magnetic ferrite nanoparticles. *Beilstein journal of nanotechnology*. 2019, vol. 10, no. 1, pp. 1348–1359. Available from DOI: 10.3762/bjnano.10.133.

[197] MOUSSA, Sherif; SIAMAKI, Ali R; GUPTON, B Frank; EL-SHALL, M Samy. Pd-partially reduced graphene oxide catalysts (Pd/PRGO): laser synthesis of Pd nanoparticles supported on PRGO nanosheets for carbon–carbon cross coupling reactions. *Acs Catalysis*. 2012, vol. 2, no. 1, pp. 145–154. Available from DOI: 10.1021/cs200497e.

[198] MARZUN, Galina; STREICH, Carmen; JENDRZEJ, Sandra; BARCIKOWSKI, Stephan; WAGENER, Philipp. Adsorption of colloidal platinum nanoparticles to supports: charge transfer and effects of electrostatic and steric interactions. *Langmuir*. 2014, vol. 30, no. 40, pp. 11928–11936. Available from DOI: 10.1021/la502588g.

[199] MAHARANA, HS; RAI, PK; BASU, A. Surface-mechanical and electrical properties of pulse electrodeposited Cu–graphene oxide composite coating for electrical contacts. *Journal of Materials Science*. 2017, vol. 52, no. 2, pp. 1089–1105. Available from DOI: 10.1007/s10853-016-0405-7.

[200] HAFIZ, Syed Muhammad et al. A practical carbon dioxide gas sensor using room-temperature hydrogen plasma reduced graphene oxide. *Sensors and Actuators B: Chemical*. 2014, vol. 193, pp. 692–700. Available from DOI: 10.1016/j.snb.2013.12.017.

[201] TUINSTRA, F; KOENIG, J Lo. Raman spectrum of graphite. *The Journal of chemical physics*. 1970, vol. 53, no. 3, pp. 1126–1130. Available from DOI: 10.1063/1.1674108.

[202] OSSONON, Benjamin Diby; BÉLANGER, Daniel. Synthesis and characterization of sulfophenyl-functionalized reduced graphene oxide sheets. *RSC advances*. 2017, vol. 7, no. 44, pp. 27224–27234. Available from DOI: 10.1039/C6RA28311J.

[203] TIAN, Hongwei; SHEN, Kai; HU, Xiaoying; QIAO, Liang; ZHENG, Weitao. N, S co-doped graphene quantum dots-graphene-TiO2 nanotubes composite with enhanced photocatalytic activity. *Journal of Alloys and Compounds*. 2017, vol. 691, pp. 369–377. Available from DOI: 10.1016/j.jallcom.2016.08.261.

[204] FANIYI, IO; FASAKIN, O; OLOFINJANA, B; ADEKUNLE, AS; OLUWA-SUSI, TV; ELERUJA, MA; AJAYI, EOB. The comparative analyses of reduced graphene oxide (RGO) prepared via green, mild and chemical approaches. *SN Applied Sciences*. 2019, vol. 1, no. 10, pp. 1–7. Available from DOI: 10.1007/s42452-019-1188-7.

[205] SPEARRIN, RM; REN, W; JEFFRIES, JB; HANSON, RK. Multi-band infrared CO 2 absorption sensor for sensitive temperature and species measurements in high-temperature gases. *Applied Physics B*. 2014, vol. 116, no. 4, pp. 855–865. Available from DOI: 10.1007/s00340-014-5772-7.

[206] LEE, Kyungwon; KANG, Shin Wook; LEE, Su-Un; PARK, Kyu-Hwan; LEE, Young Wook; HAN, Sang Woo. One-pot synthesis of monodisperse 5 nm Pd–Ni nanoalloys for electrocatalytic ethanol oxidation. *ACS applied materials & interfaces*. 2012, vol. 4, no. 8, pp. 4208–4214. Available from DOI: 10.1021/am300923s.

[207] ZHAO, Juan; SARKAR, Arindam; MANTHIRAM, Arumugam. Synthesis and characterization of Pd-Ni nanoalloy electrocatalysts for oxygen reduction reaction in fuel cells. *Electrochimica Acta*. 2010, vol. 55, no. 5, pp. 1756–1765. Available from DOI: 10.1016/j.electacta.2009.10.061.

[208] WANG, Ye; SHI, Fei-Fei; YANG, Yao-Yue; CAI, Wen-Bin. Carbon supported Pd–Ni–P nanoalloy as an efficient catalyst for ethanol electro-oxidation in alkaline media. *Journal of power sources*. 2013, vol. 243, pp. 369–373. Available from DOI: 10.1016/j.jpowsour.2013.06.021.

[209] RAI, Rohit K; GUPTA, Kavita; TYAGI, Deepika; MAHATA, Arup; BEHRENS, Silke; YANG, Xinchun; XU, Qiang; PATHAK, Biswarup; SINGH, Sanjay K. Access to highly active Ni–Pd bimetallic nanoparticle catalysts for C–C coupling reactions. *Catalysis Science & Technology*. 2016, vol. 6, no. 14, pp. 5567–5579. Available from DOI: `10.1039/C6CY00037A`.

[210] GHANBARI, Najmeh; HOSEINI, S Jafar; BAHRAMI, Mehrangiz. Ultrasonic assisted synthesis of palladium-nickel/iron oxide core–shell nanoalloys as effective catalyst for Suzuki-Miyaura and p-nitrophenol reduction reactions. *Ultrasonics sonochemistry*. 2017, vol. 39, pp. 467–477. Available from DOI: `10.1016/j.ultsonch.2017.05.015`.

[211] FENG, Li; CHONG, Hanbao; LI, Peng; XIANG, Ji; FU, Fangyu; YANG, Sha; YU, Hui; SHENG, Hongting; ZHU, Manzhou. Pd–Ni alloy nanoparticles as effective catalysts for Miyaura–Heck coupling reactions. *The Journal of Physical Chemistry C*. 2015, vol. 119, no. 21, pp. 11511–11515. Available from DOI: `10.1021/jp510988m`.

[212] ISMAIL, N; MADIAN, M; EL-SHALL, M Samy. Reduced graphene oxide doped with Ni/Pd nanoparticles for hydrogen storage application. *Journal of Industrial and Engineering Chemistry*. 2015, vol. 30, pp. 328–335. Available from DOI: `10.1016/j.jiec.2015.06.002`.

[213] WAN, Xiaoyang; WEI, Xuefeng; MIAO, Juan; ZHANG, Ruichang; ZHANG, Jun; NIU, Qingshan Jason. Pd-Ni/Cd loaded PPy/Ti composite electrode: synthesis, characterization, and application for hydrogen storage. *International Journal of Energy Research*. 2019, vol. 43, no. 8, pp. 3284–3294. Available from DOI: `10.1002/er.4458`.

[214] LEE, Eunsongyi; LEE, Jun Min; LEE, Eunyoung; NOH, Jin-Seo; JOE, Jin Hyoun; JUNG, Bumsuk; LEE, Wooyoung. Hydrogen gas sensing performance of Pd–Ni alloy thin films. *Thin Solid Films*. 2010, vol. 519, no. 2, pp. 880–884. Available from DOI: `10.1016/j.tsf.2010.07.122`.

[215] WANG, Wen; LIU, Xueli; MEI, Shengchao; LIU, Mengwei; LU, Chao; LU, Minghui. Development of a High Stability Pd-Ni Alloy Thin-Film Coated SAW Device for Sensing Hydrogen. *Sensors*. 2019, vol. 19, no. 16, pp. 3560. Available from DOI: `10.3390/s19163560`.